A DRAW-BEND FRICTION TEST APPLIED TO MEASUREMENT AND MODELING OF ANISOTROPIC FRICTION ON SHEET METAL

A DRAW-BEND FRICTION TEST APPLIED TO MEASUREMENT AND MODELING OF ANISOTROPIC FRICTION ON SHEET METAL

By

YOUNG SUK KIM, B.Eng., M.A.Sc.,

A Thesis

Submitted to the School of Graduate Studies

In Partial Fulfillment of the Requirements

for the Degree

Doctor of Philosophy

McMaster University

DOCTOR OF PHILOSOPHY (2008)
(Mechanical Engineering)

McMaster University
Hamilton, Ontario

TITLE: A Draw-Bend Friction Test Applied to Measurement and Modeling of Anisotropic Friction on Sheet Metal

AUTHOR: Young Suk Kim, B. Eng. (Korea Univ. - Korea),
M.A.Sc. (McMaster Univ.)

SUPERVISOR: Professor Mukesh K. Jain
Professor Don. R. Metzger

NUMBER OF PAGES: xviii, 170

ABSTRACT

In sheet metal forming processes, friction has decisive effects on the strain distribution in the deformed sheets and the quality of the final product due to the large surface/thickness ratio of the blank sheets. It is well known that friction in sheet forming operations is dependent on local contact conditions such as surface roughness, contact pressure and sliding velocity. Adding complexity to this frictional behavior, some rolled sheets have oriented surface roughness and show considerable frictional anisotropy. A constant friction model without consideration of these relevant phenomena is regarded as the reason why sheet metal forming simulations often fail to produce satisfying results despite the well developed material models.

To develop a friction model which considers both of the varying conditions of local contact and the frictional anisotropy was the aim of this thesis. For this purpose, the analysis method of the friction test (draw-bend test) had to be examined for the capability to evaluate these parameters independently. Through careful study using finite element simulations, it was found that the conventional method has shortcomings in addressing pressure dependent friction due to the pressure non-uniformity existing in the test. Therefore, a new analysis method, which can evaluate pressure dependency of a friction coefficient, was developed. In the new method, contact pressure maps obtained from simulations were included in the analysis of test data.

The new analysis method was applied to friction measurement of aluminum sheets with known anisotropic mill finish, and friction coefficients were obtained as functions of contact pressure, sliding velocity and sliding direction. In the obtained friction model, a friction coefficient is a continuous surface over the domain of contact pressure and sliding velocity. Lastly, the new friction model was implemented into a finite element code and the model was validated through circular cup drawing experiments and simulations. The comparisons showed good agreements in the aspects of punch force, cup size and failure location. Thus, the newly developed model can accurately predict the effects of anisotropic friction in sheet metal forming processes.

ACKNOWLEDGEMENT

I would like to express my sincere gratitude to my supervisors, Dr. Mukesh Jain and Dr. Don Metzger for their knowledgeable supervisions and patient encouragements throughout this research. I am privileged to have both of them as my mentors, still having a dream of becoming like them in my field.

I would like to thank Doug Kenny in Novelis Global Technology Centre for his help for friction tests, which had been prolonged over two years. I enjoyed the conversations with him about our lives more than the long series of tests.

I would like to thank Yen Jin Kim, my sister-in-law and a wonder-mother of three super-boys, for her insightful advice on the composition of this thesis.

I would like to thank brothers and sisters in Hamilton Korean Presbyterian Church for their continual prayers that make me see the way to run beyond this thesis. Quite a while, their greetings to me at Sunday morning had been "How many chapters did you finish?". I would also like to thank spiritual brothers and sisters in New York and in Arkalyk and Karaganda regions of Kazakhstan.

I would like to express my gratitude to my dear wife, Yensen, my son, Samuel, and my daughter, Dahee, for all the supports they gave as they always trusted me.

Finally, I would like to express my deep gratitude towards my parents for their prayers, encouragement and love.

TABLE OF CONTENTS

LIST OF FIGURES

LIST OF TABLES

CHAPTER 1

INTRODUCTION

1.1. Background and Motivation

Finite element simulation technologies are useful tools for the process and tool development of sheet metal forming operations and a friction model plays an important role in the sheet metal forming simulations. In sheet metal forming processes, the frictional force is a significant portion of the total force, due to the large surface/thickness ratio of the blank sheets. Hence, friction affects the stress and strain distribution in the deformed sheets, and the quality of the final product.

Applying a constant friction coefficient to the simulations has been common practice (Zhou and Wagoner, 1995; Nakamachi and Huo, 1996; Mamalis et al., 1997), but it is well known that the friction coefficient is a function of local contact conditions such as roughness, pressure and sliding velocity (Schey and Nautiya, 1991; Emmens, 1988; Schipper, 1988). Adding complexity to frictional behavior, some rolled sheets such as mill-finished aluminum sheets have oriented surface textures and show considerable frictional anisotropy. Constant friction models without consideration of these relevant phenomena could be the reason why sheet forming simulations often fail to produce satisfactory results despite the well developed material models. Therefore, investigation is

required to determine how a friction model might consider the varying conditions of local contact and the frictional anisotropy.

1.2. Literature Review

1.2.1. Friction in Sheet Metal Forming

The classical Coulomb's friction law is represented by a constant friction coefficient, which is independent of sliding velocity and contact pressure. This is approximately true for friction between unlubricated metals at low surface pressures. The mechanisms for these phenomena were explained by Amontons (Bowden and Tabor, 1971) as the formation and shearing of metallic junctions between surface asperities. But for lubricated surfaces as in the sheet metal forming processes, the friction coefficient is observed to depend on several parameters including sliding velocity and contact pressure (Schey and Nautiya, 1991; Emmens, 1988; Schipper, 1988). Figure 1.1 illustrates the friction mechanism in lubricated contacts, where lubricant is dragged from the surface's micro-valleys (Vermeulen et al., 2001). This model explains the dependency of friction coefficient on sliding velocity and pressure.

Frictional behavior of richly lubricated surfaces is often described using Stribeck curve (Dowson, 1998), where friction coefficient is plotted in relation to lubricant viscosity, sliding velocity and contact pressure. The details of this curve will be given in

Chapter 3, where the Stribeck friction model is used to study the effect of the pressure non-uniformity on friction measurements.

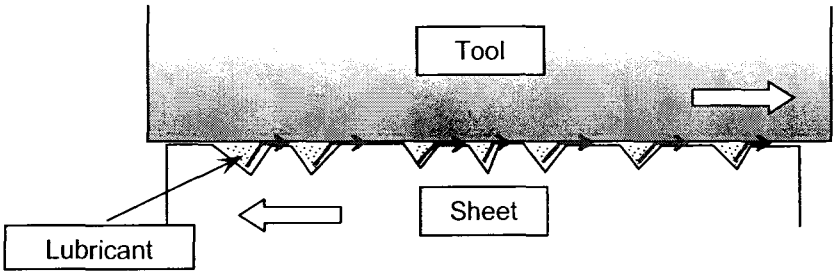

Figure 1.1 Friction mechanism in lubricated contacts.

Two approaches to model the friction in sheet metal forming include the theoretical and empirical approaches. In the theoretical approach, friction is modeled according to the physical laws at micro-mechanical level of contacts (Hsu and Liu, 1998; Ter Haar, 1996; Westeneng, 2001). In the empirical approach, the friction coefficient is measured through experiments and the correlations between measured friction coefficient and the parameters in the test condition are modeled (Emmens, 1988; Ghosh, 1977; Keum et al., 2004). The relation between two approaches is analogous to the relation between the modeling of dislocations at the atomistic level and the mechanical response in tensile tests. In this research, an empirical approach using a particular friction test is used for the friction model development.

1.2.2. Friction Test Methods for Sheet Metals

There are wide variety of friction test methods for sheet metal forming applications. Each test has its own strengths and limitations, and the test has to be performed and evaluated with a proper understanding of its characteristics. The basic guidelines to select a friction test method are simplicity and similitude (Wagoner and Chenot, 1996). Simplicity is judged in terms of the separation of frictional effects from other effects, and similitude concerns how much the friction test is similar to the actual operation.

There are three common friction test methods for sheet metals as illustrated in Figure 1.2. In a **strip draw friction test**, a metal strip is pulled while a friction die applies a normal force on the strip (Matuszak, 2000; Han, 1997; Lee et al., 2002; Roizard, 1999) or the friction die is slid on the strip while the tensile strain is applied on the strip (Ter Haar, 1996). The friction die can have flat or cylindrical contact geometries. The interpretation of the strip draw test is simple; the tangential force divided by normal force is the friction coefficient. However, this method has less similitude to sheet metal forming, and the range of applicable pressure load is lower than the other two types due to the strip failure by the combined effect of pressure and pulling stresses.

In the **twist-compression friction test**, a rotating annular die is compressed on a flat specimen while the normal load and torque are measured (Schey and Nautiya, 1991; Reid, 2005; Wiklund et al., 2004). The test can be performed at higher pressure load than the strip draw test, but it cannot be used to measure the friction anisotropy due to the

rotating motion of the die and it also has less similitude to sheet metal forming, but is best suited for a comparative assessment of lubricant against depletion.

The **draw-bend friction test** is most widely used for sheet metals due to its similitude to sheet forming operations. The test method has the capability to change process variables such as pressure, sliding velocity and strain rate independently (Chvedov et al., 2003; Wilson et al., 1991; Vallance and Matlock, 1992; Han, 1997; Wihlborg and Crafoord, 2001; Fratini et al., 2006). By using different sized pins and controlling the motions of actuators, the test can be performed at wide ranges of pressure, velocity and strain rate conditions.

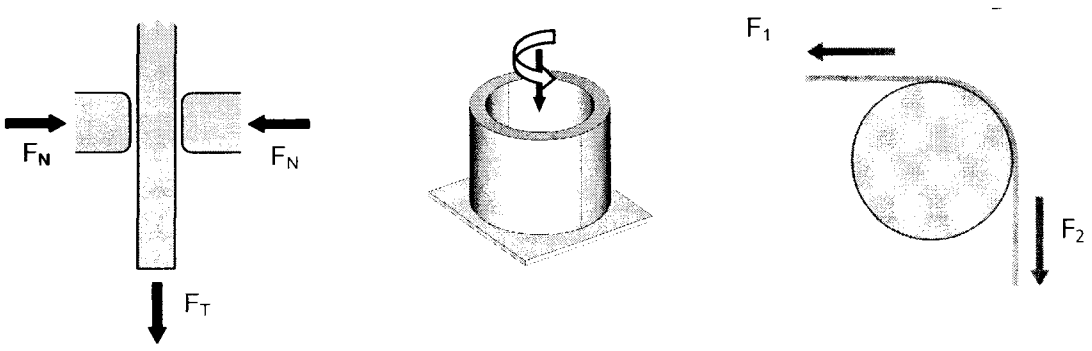

(1) Strip Draw Test (2) Twist-Compression Test (3) Draw-Bend Test

Figure 1.2 Friction measurement methods for sheet metals.

1.2.3. Draw-Bend Friction Test

For the new friction model development, the dependency of the friction coefficient on the parameters (pressure, velocity and sliding direction) has to be measured through a proper friction test method. The draw-bend friction test is regarded as the best candidate for this purpose because of its known capability to change contact pressure and sliding velocity (Saha et al., 1994). Friction anisotropy can be measured by performing tests with specimens cut in different textural directions.

In a draw bending test a metal strip is slid over a cylindrical pin while the pulling forces are measured and the friction coefficient is estimated from the pulling forces and pin radius (Fox et al., 1989). The estimation of friction coefficient from the test data is based two important underlying assumptions (Swift, 1948):

1) The cylindrical die/strip contact angle is equal to the geometric wrap angle.
2) The pressure distribution at the contact is uniform.

However, due to the bending stiffness of a metal strip, pressure non-uniformity at the contact interface of the draw-bend tests has been postulated (Hanaki and Kato, 1984; Patula, 1979; Sniekers, 1996). Alinger et al. (1999) measured the strains on the outer surfaces of metal strips through the test and noticed that the real contact angle is less than a geometric wrap angle. Coubrough et al. (2002) obtained qualitative data, which show the existence of pressure peaks at the pin die/strip contact, by using a contact sensor on the die. They also observed the real contact angle is less than the geometric wrap angle.

Kim et al. (2004) showed these phenomena clearly using 3D finite element simulations of the tests.

From various draw-bend friction experiments, where the friction coefficients were estimated using the methodology based on these assumptions, it has been uniformly reported that the friction coefficient increases as the die radius used in the tests decreases (Zheng and Overby, 1988; Kotchman et al., 1992; Saha et al., 1996; Han, 1997; Keum et al., 2004; Deng and Lovell, 2000). These experimental and numerical observations raise the need for re-examination of the current methodology before the test is applied to the current research.

1.2.4. Anisotropic Friction in Aluminum Sheets

The surface texture of a metal sheet has a strong influence on the friction property of the sheet. The surface texture is imparted by a transfer of surface texture of work roll to the strip. When sheet material is rolled with tangentially ground work rolls, mill-finished (MF) surface texture arises. Electro-Discharge (EDT) texture arises with work rolls whose surfaces are treated by the electric sparks to have isotropic texture. Figure 1.3 shows roughness oriented in Rolling Direction (RD) of a MF aluminum sheet, and isotropic texture of an EDT aluminum sheet.

Aluminum sheets with oriented roughness show considerable directionality in friction behavior. Figures 1.4, 1.5 and 1.6 are test results from three different groups (Murtha et al., 1995; Saha et al., 1996; Kenny et al., 2000). From all the experiments,

friction was higher in the longitudinal direction by an order of 1.4-2.1. Therefore, the friction anisotropy has been measured through the draw-bend tests and considered in the new friction model in this research.

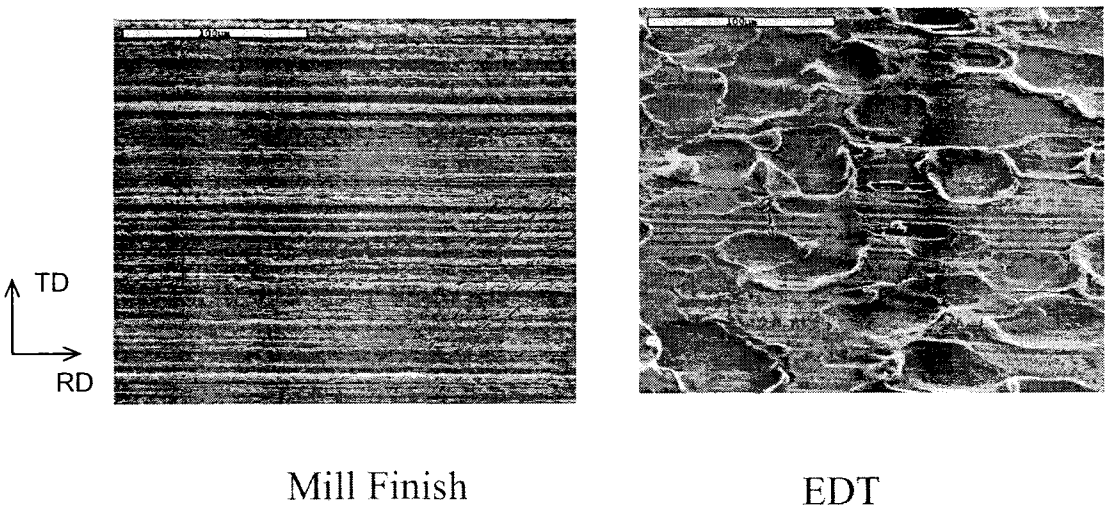

Figure 1.3 Surface textures of Mill-Finished and EDT aluminum sheets (Kenny et al., 2000).

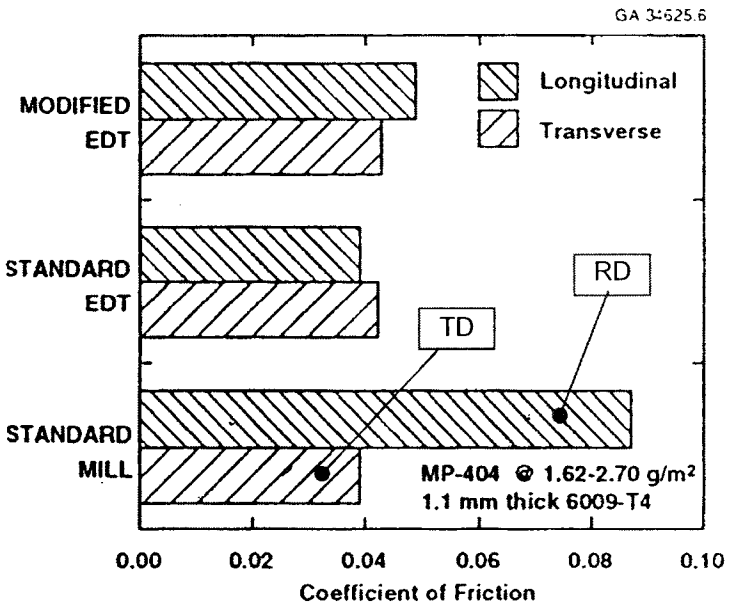

Figure 1.4 Friction coefficients of aluminum sheets (drawbead test) (Murtha et al., 1995).

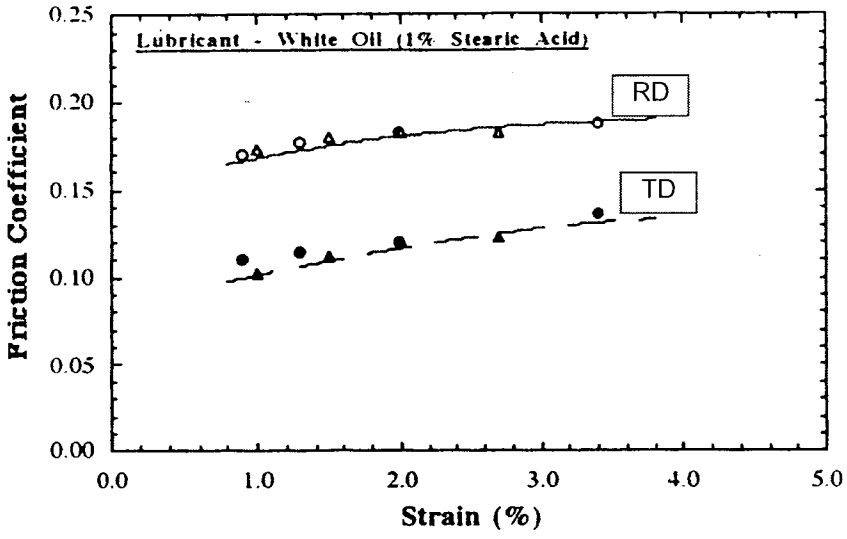

Figure 1.5 Friction coefficients of MF aluminum sheets (draw-bend test) (Saha et al., 1996).

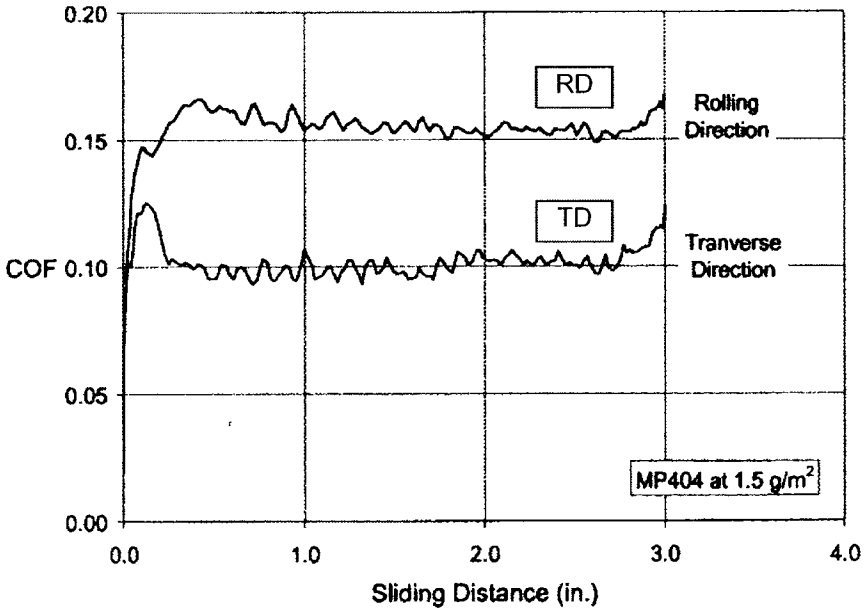

Figure 1.6 Friction coefficients of MF aluminum sheets (draw-bend test) (Kenny et al., 2000).

1.2.5. Anisotropic Friction Modeling for Sheet Metal Forming Simulation

From the review of current literatures on anisotropic friction models for sheet metal forming simulations, it was found that no such specific research on the subject is available yet. There appeared publications on anisotropic friction models for dry friction (Buczkowsk and Kleiber, 1997; Hjiaj et al., 2004; Zhang et al., 2004; Jones and Papadopoulos, 2006), which were implemented in finite element codes. Buczkowsk and Kleiber (1997) used elliptical stick/slip criterion with two different non-linear friction coefficient functions accounting for the transition from static to dynamic friction. In the model of Hjiaj et al. (2004), the stick/slip criterion was represented by superellipse with

two different friction coefficients in principal directions. In the work of Zhang et al. (2004), a piecewise approximation of the elliptic criterion was used for their specially designed smoothing algorithm. However, all the models in the publications consider Coulomb anisotropic friction with constant friction coefficients, which is more suited to unlubricated dry surfaces.

The reason for the lack of research on anisotropic friction modeling for lubricated contacts in sheet metal forming is largely related to the fact that the friction modeling even for isotropic surface conditions has not been successful so far. Therefore, for the development of new friction model for sheet metal forming simulations, both of the following are required to be considered:

- Frictional dependence on the varying local contact conditions during sheet forming operation

- Frictional dependence on sliding directions

1.3. Objectives

The initial aim of this research was to develop an anisotropic friction model for rolled sheets, which can be readily implemented into a finite element code. In the process of research, a need for re-examination of the analysis method of draw-bend friction test method itself has been raised. Therefore, the objectives of this research are:

- To develop a new method to analyse the draw-bend test data considering the non-uniform pressure distribution at the pin/strip interface,

- To apply the new method to draw-bend friction tests with MF aluminum sheets to measure friction coefficients as a function of local contact conditions (pressure, velocity, and sliding direction),

- To develop a new friction model and implement the model into a finite element code,

- To validate the new friction model through circular cup drawing experiments and simulations.

1.4. Methodology

To develop a friction model which considers both the varying conditions of local contact and the frictional anisotropy, this research will be composed of two parts. In the first part (Chapters 2, 3 and 4), the conventional analysis method of draw-bend friction test will be examined thoroughly for the capability to evaluate those parameters independently. A new analysis method will be developed if it is required by the study. The second part (Chapters 5 and 6) will consider friction tests with MF aluminum sheets and analysis of test data using the method proved in the first part. New friction model will be obtained as functions of contact pressure, sliding velocity and sliding direction. Lastly, the new friction model will be validated through circular cup drawing experiments and simulations, which are representative of sheet forming processes.

In Chapter 2 the general aspects of draw-bend friction test are studied through the finite element simulations. Using 3D finite element models and local axis systems, the pressure and strain distributions on the frictional contact surface are investigated.

In Chapter 3 the influence of the observed pressure non-uniformity on the friction measurement is evaluated in more detail using a variable friction (Stribeck) coefficient model.

In Chapter 4 a new method to extract variable friction coefficient from the draw-bend tests is developed. The prediction capability of the new method is tested by applying the method to back-predict the input friction data for the simulations with the variable friction coefficient model.

In Chapter 5, the new method is applied to real friction experimental data. For this purpose, draw-bend friction tests are performed on MF aluminum sheets and the test data are analyzed using the new method. The new friction model as functions of contact pressure, sliding velocity and sliding direction is obtained.

In Chapter 6 the new friction model is implemented into a finite element code. The new model is validated through circular cup drawing experiments and simulations to prove that relevant features of real applications are adequately captured.

CHAPTER 2

FINITE ELEMENT STUDY ON DRAW-BEND FRICTION TEST

2.1. Introduction

The draw-bend friction test is commonly used for sheet metal forming applications due to its similitude to sheet forming operations. In draw-bend friction tests, friction is measured between a metal strip and a cylindrical pin while the strip slides and bends around the pin as illustrated in Figure 2.1. General steps for conducting a draw-bend friction test are:

1) Both ends of a strip are clamped to the inlet and outlet grips.
2) While fixing the inlet end, the outlet end moves until the strip reaches the desired tension.
3) Outlet end moves with prescribed velocity and the inlet end follows keeping a constant tension force so that the strip slides over the pin. The inlet and outlet strip tension forces are recorded to measure the friction coefficient.

From the measured inlet and outlet tension forces, the friction coefficient is calculated. The difference between these two forces comes from two sources, friction and elastic/plastic bending. The bending force F_B is obtained by repeating the same test with a freely rotating pin, or it is estimated using Equation (2.1) according to Swift (1948).

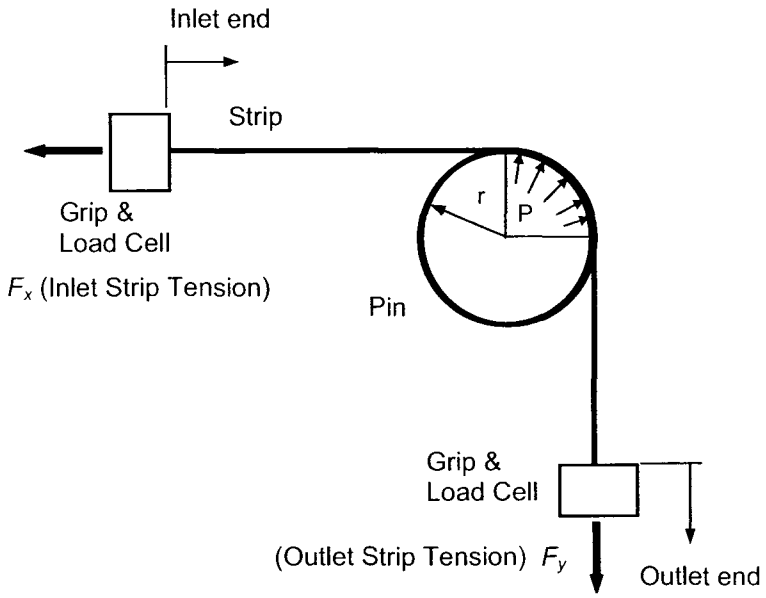

Figure 2.1 Schematic of draw-bend friction test.

$$F_B = \frac{\sigma_y \cdot t^2 \cdot w}{2 \cdot r} \cdot \tan\frac{\Theta}{2} \tag{2.1}$$

where σ_y is the yield stress of the strip, t is the strip thickness, w is the width of the strip, r is the pin radius, and Θ is the angle of wrap. Then the average contact pressure P and friction coefficient μ are calculated using Equations (2.2) and (2.3) (Vallance and Matlock, 1992).

$$P = \frac{\left(F_x + F_y\right)}{2 \cdot r \cdot w} \tag{2.2}$$

$$\mu = \frac{1}{\Theta} \ln \frac{(F_y - F_B)}{F_x} \tag{2.3}$$

The above equations originate from the rope formula, which is the characteristic of a flexible rope sliding over a cylindrical pin. These equations have the underlying assumptions of uniform pressure and angle of contact that extends over the entire geometric angle of wrap. Therefore, it is meaningful to investigate the local contact pressure and strain distributions in the test by finite element simulations and to evaluate the equations. It will help understand the behavior of the materials at the contact zone and the experimental characteristics of draw-bend friction tests.

2.2. Modeling and Simulation

A top half of the geometry of the strip and pin was modeled to exploit the symmetry condition. The strip consisted of 3,968 3D (brick) 8 node elements and the pin was modeled as rigid surface with 336 2D elements. In the strip model, 4 elements through thickness and 8 elements in width were used (Figure 2.2). Local axis systems were defined for each element in the strip model. These axes rotate with each element throughout the deformation. This allows the stress component in the through-thickness direction at the contact zone to represent contact pressure. The stress-strain data was selected from the experimental results provided by Novelis Global Technology Centre for aluminum sheets (Figure 2.3) and isotropic elastic-plastic material model was used.

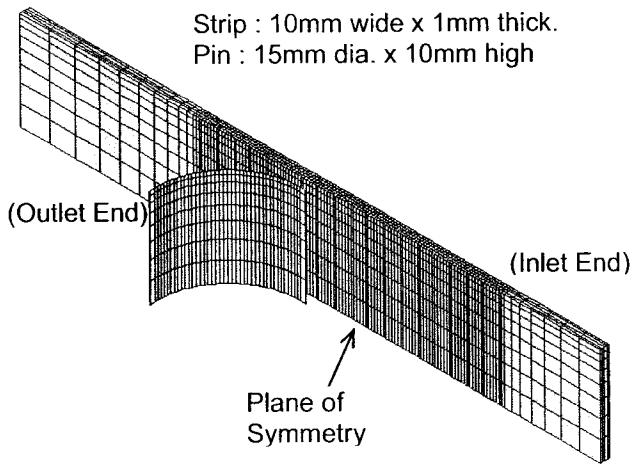

Figure 2.2 Finite element models of a strip and a pin.

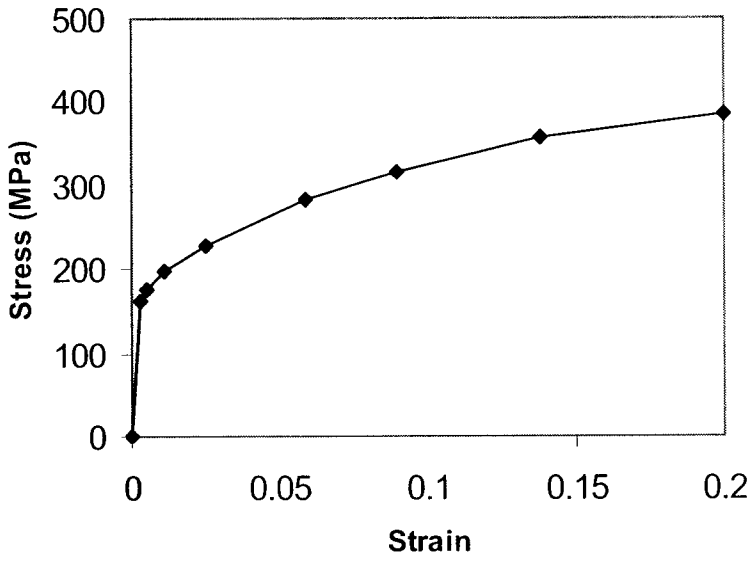

Figure 2.3 Stress-strain curve for aluminum sheet.

To achieve more realistic results, the pre-bending steps explained in the previous section were included in the simulation (Figure 2.4). Beginning with the unbent strip model, the simulation was performed with the following procedures.

Step 1) While fixing the inlet end, the outlet end was loosely bent around the pin by applying a circular motion to outlet end nodes.

Step 2) Nodes at the outlet end moved with specified velocity until the strip reached a certain tension.

Step 3) Both inlet and outlet ends move together with defined velocities (outlet and inlet ends traveled 21.4 mm and 19.7 mm respectively during step 3).

Time spans were 0.25 s for step 1, 0.2 s for step 2, and 0.77 s for step 3. In step 3 the strip slid 21 mm (average of the inlet and outlet ends movements) over the pin.

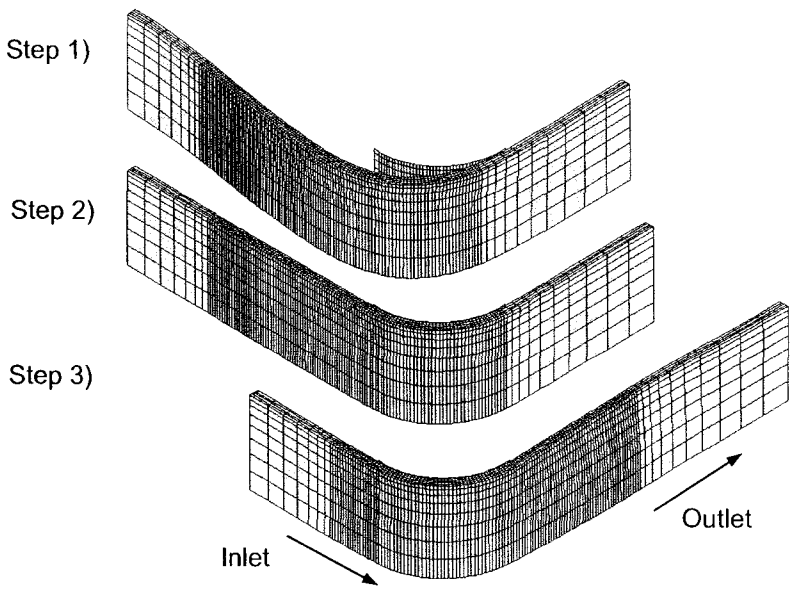

Figure 2.4 Procedures for draw-bend friction test simulation.

All simulations were performed with the finite element software called H3DMAP (Sauvé, 1999), which uses an explicit solution method that is well suited to large deformation problems. The routinely used technique of mass scaling was applied to reduce computation time of the simulations. Two simulations were run for a frictionless case with 100 and 2000 times mass scaling for comparison. Figure 2.5 shows the von Mises stresses of one element during step 3 run for 2000 times and 100 times mass scaling cases. The results assure that any error due to the dynamic effect of mass scaling is minor, even for the higher mass scaling factor of 2000. This improves computational time by a factor of 44 ($=\sqrt{2000}$) since the stable time step is proportional to the square root of mass (Belytschko, 2000).

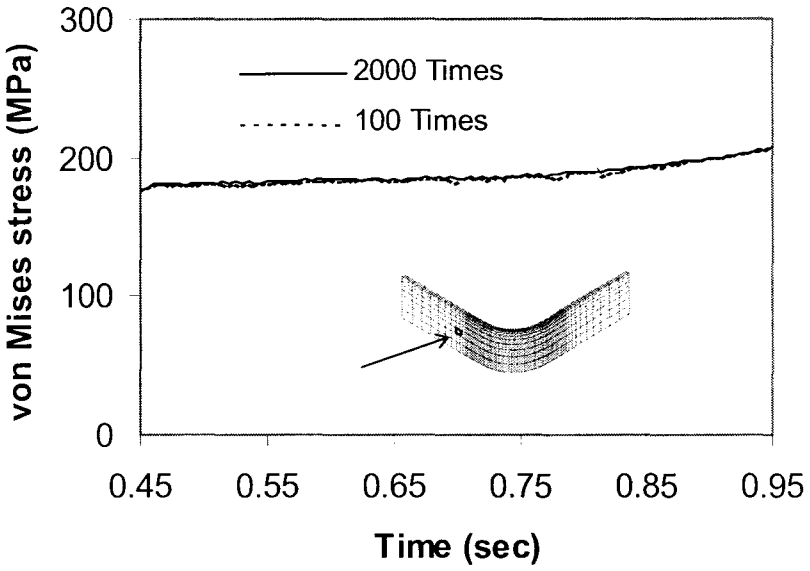

Figure 2.5 von Mises stress comparison between 2000 times and 100 times mass scaling cases (μ =0).

2.3. Simulation Results

2.3.1. Contact Pressure Distribution

As mentioned in the previous section, by using local axis systems in the simulations, stress in the through-thickness direction (σ_{zz}) at the contact zone represent the contact pressure. Figures 2.6 and 2.7 show the contact pressure (σ_{zz}) distribution at the instance shown on the small picture of Figure 2.6 during the step 3 simulation. In this case the friction coefficient of μ=0.1 was applied. Pressure distribution is quite non-uniform both in the longitudinal and transverse directions. Pressure peaks appear near the inlet and outlet regions, and the outlet side pressure peak is somewhat higher than the inlet side peak (Figure 2.7). Also, there are pressure peaks in the transverse direction near the strip edges. A simulation was repeated with friction coefficient μ = 0 and it showed almost the same pressure distribution (maximum pressure was 1.2% lower than the friction case). Therefore, the pressure peak difference between inlet and outlet is not coming from the friction force, but it is rather related to bending and unbending forces in the pin contact region.

Figure 2.8 shows a section of the strip, and the noticeable feature is that the strip edge deforms outward to become free of contact at the edge. This agrees with the experimental observation of non-contacted surface topography shown on the specimen after the tests as shown in Figure 2.9. From Figure 2.6 it can be seen that the contact angle in the longitudinal direction is less than 90°. To check the contact condition in

longitudinal direction, the penetrations of the nodes defining the pin through the strip surface were measured because the contact algorithm allows for small penetration at the contact interfaces. Figure 2.10 shows the penetration distances of the nodes defining the pin through the contact surface around row 6 of Figure 2.6. The real contact angle was 74° (from 11.5° to 85.5°), which is 18% less than the wrap angle.

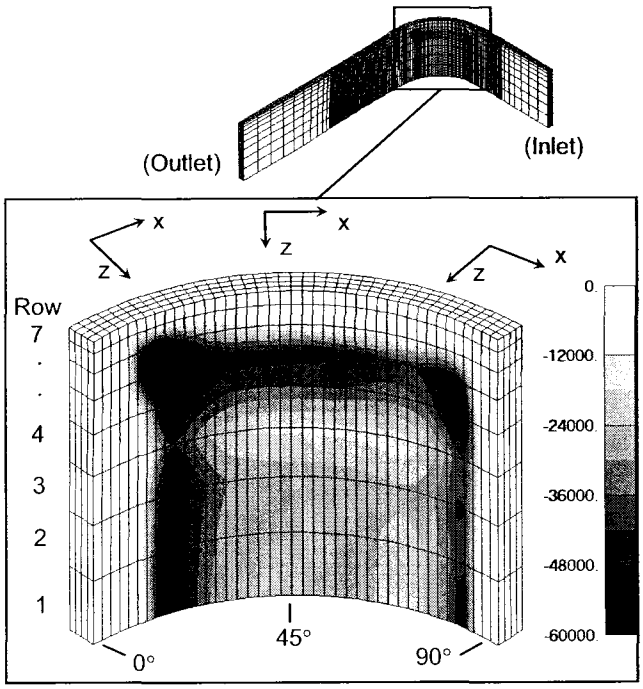

Figure 2.6 Contact pressure (KPa) distribution at t = 1.024 s.

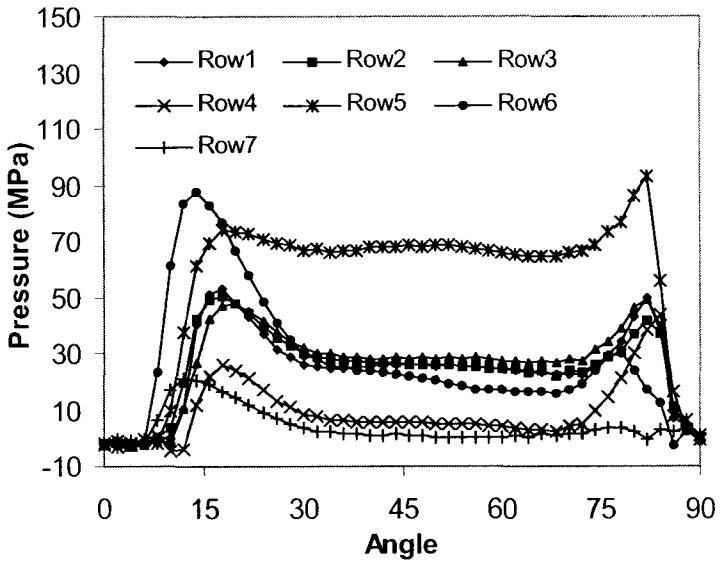

Figure 2.7 Contact pressure (MPa) distribution at each row (t = 1.024 s).

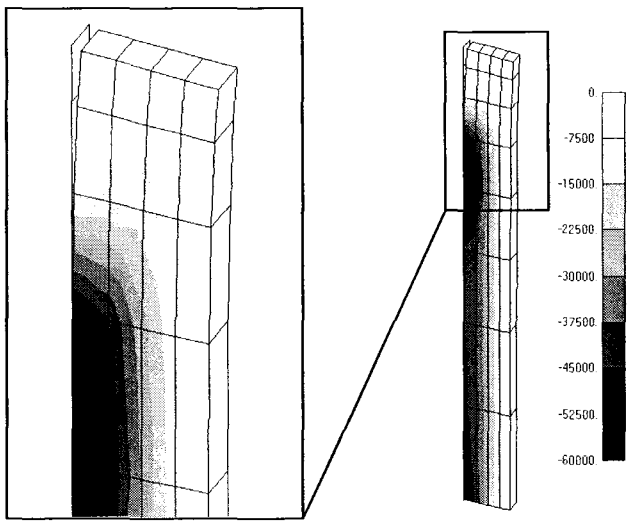

Figure 2.8 Section view of a strip model, there is no contact at the strip edge.

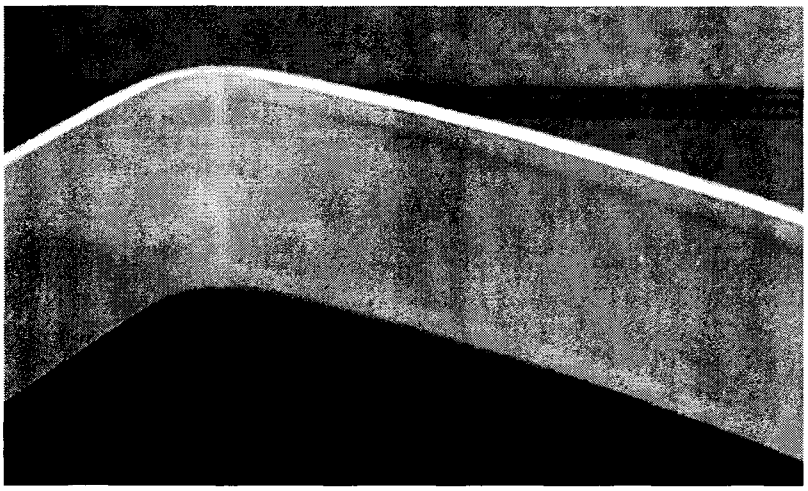

Figure 2.9 A strip specimen after a draw-bend friction test (Novelis Global Technology Centre). Non-contacted regions are seen along the edges.

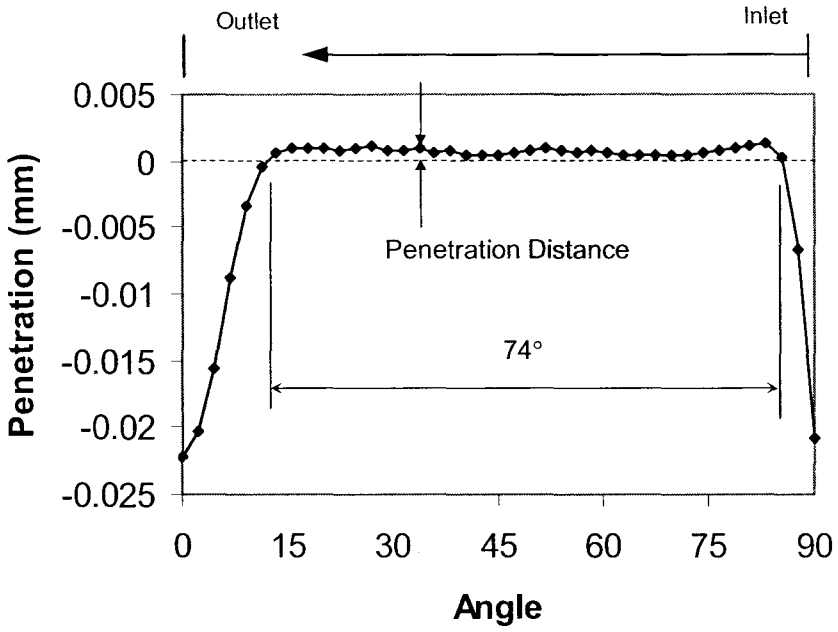

Figure 2.10 Penetrations of nodes defining the pin through the strip contact surface around row 6.

2.3.2. Strain Distribution

Often, the draw-bend test rig is used to control strain while measuring friction coefficient to study the strain effect on friction. The strain is controlled by adjusting the inlet and outlet grip motions (see Figure 2.1) and the strain is measured by attaching the strain gages (Alinger et al., 1999) or by mounting the displacement sensors on the outside surfaces of strips (Wilson et al., 1991). The strain in the inside surface of a strip is impractical to measure, so the inside and outside strain distributions were investigated from the simulations.

Longitudinal strain data were collected from the deformed distances between neighboring nodes divided by the original distances in the longitudinal direction of the strip model. The strain differences among rows were found to be minor. Figures 2.11 and 2.12 show how the outside and inside strains at row 1 evolved and reached the uniform distribution toward the end of the test. A simulation was repeated with frictionless contacts and it showed the same trend with a 1.6% higher maximum strain than the friction case (μ = 0.1) at t=0.895 s. These results suggest that the strain evolution is not coming from the friction, but it is related to the bending and unbending processes of the strip. The test is performed with a strip loaded by the steps 1 and 2 of Figure 2.4, where the strip is loosely bent and tightened over the pin. Because of this pre-bending process, the strip shows the initial uniform strain distribution. As the strip slides over the pin, the strip shows the non-uniform and transient strain distribution and finally reaches the uniform and steady distribution. It can be seen from the results that steady condition was

reached at t=1.01 s after the strip slid 17 mm which is 1.5 times to the length (11.8 mm) of wrap around the pin.

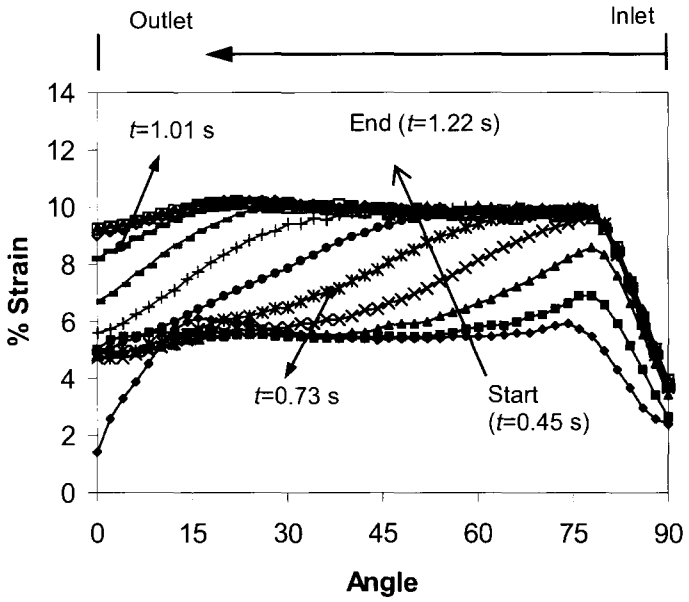

Figure 2.11 Longitudinal strain (outside) evolution during step 3 simulation from elements in row 1 (refer to Figure 2.6 for nomenclature). Outside refers to free surface of a strip.

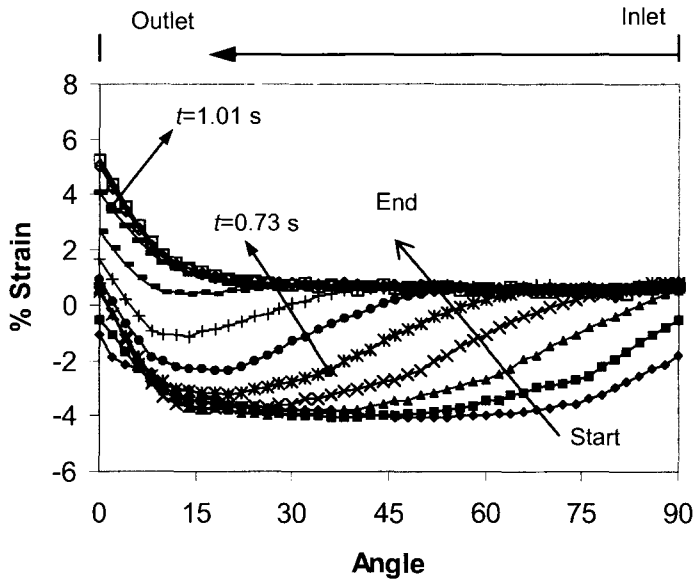

Figure 2.12 Longitudinal strain (inside) evolution during step 3 simulation from elements in row 1 (refer to Figure 2.6 for nomenclature). Inside refers to contact side of a strip.

Figure 2.13 compares the strain distributions of outside and inside surfaces of the strip after the steady state conditions were reached. It shows that the strain increase was concentrated at the inlet region of outside surface and at the outlet region of inside surface. The strains are rather constant at the contact regions of the strip as marked in Figure 2.13. The mechanism for this phenomenon can be explained from the longitudinal stress distribution and plastic strain distribution in the strip as shown in Figures 2.15 and 2.16 respectively. This observation is different from the assumption of Wilson et al. (1991) that the strain increases linearly from the inlet to outlet of a strip. They measured the displacements of a strip at the inlet and outlet regions and calculated the strain distribution at contact region of the strip as shown in Figure 2.14.

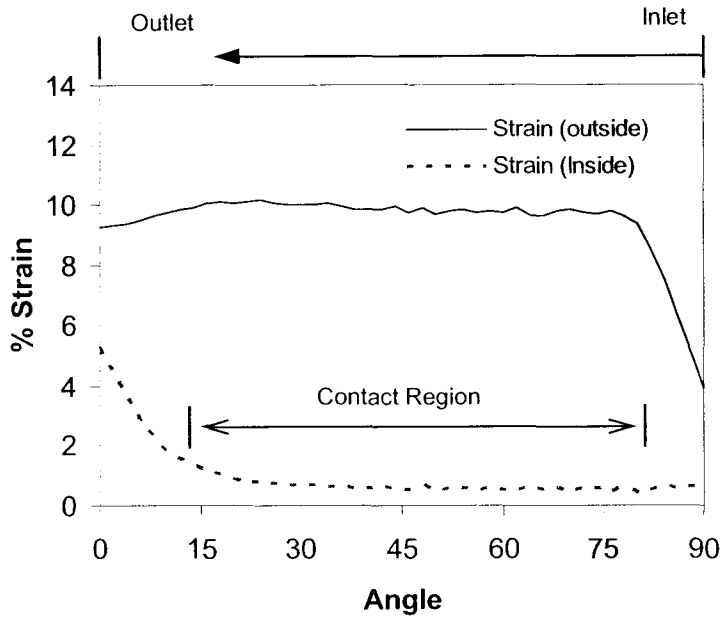

Figure 2.13 Longitudinal strain distributions of outside and inside surfaces of a strip after the steady conditions are reached.

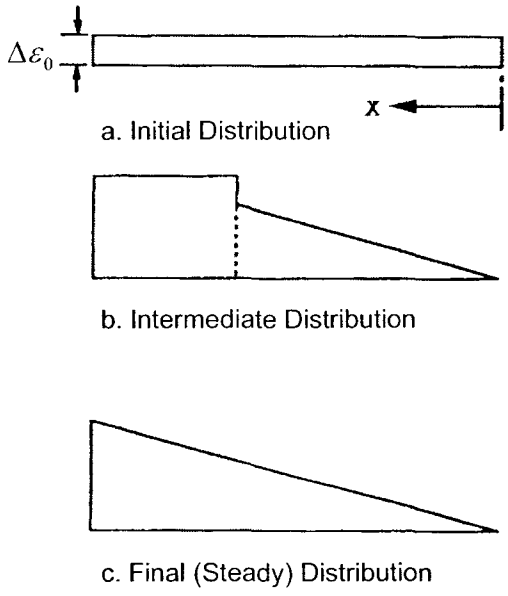

Figure 2.14 Assumptions by Wilson et al. (1991) for strain distribution in contact surface of draw-bend test.

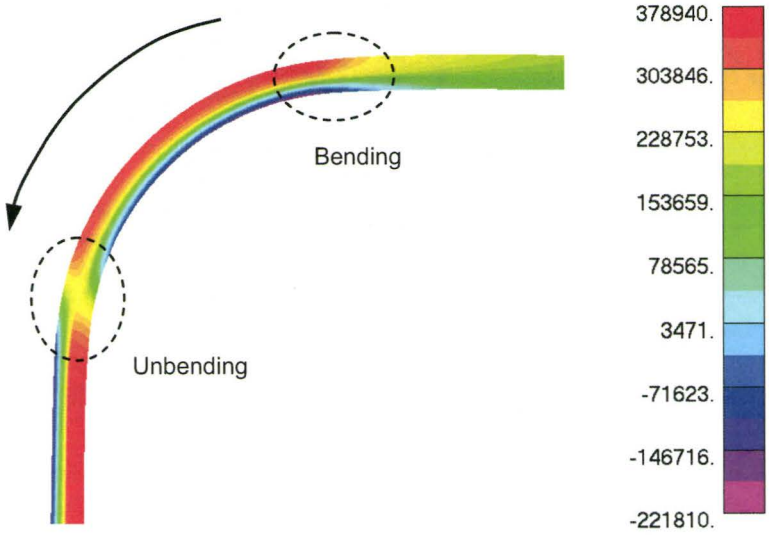

Figure 2.15 Longitudinal stress (Pa) distribution from simulation.

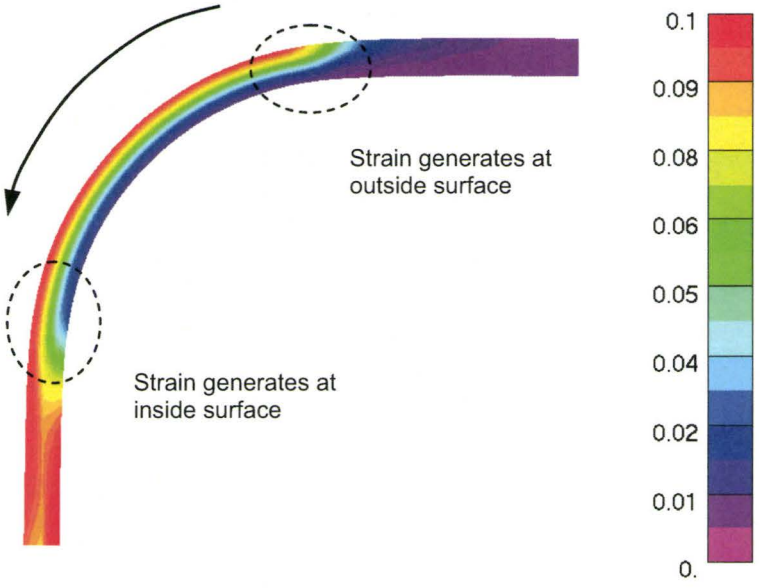

Figure 2.16 Longitudinal plastic strain (natural strain) distribution from simulation.

Alinger et al. (1999) measured the longitudinal strain of a steel strip during the draw-bend test. In their experiment, a strain gage was mounted on the outside surface of a strip in a location that allowed the gage to completely traverse the pin in the test. Therefore, their measurement does not show the strain distribution around the strip at the fixed times, but rather it shows the strain changes of one spot on the strip surface during the test. For the qualitative comparison with their result, strain data of one location were collected from the simulation. The strain collection spot was selected so that the point is located close to the middle of pin contact length at t=0.73 s, when the strain distribution was most non-uniform (see Figures 2.11 and 2.12). The results are plotted in Figure 2.17 for frictionless and frictional cases. While the strip was in contact with the pin, the strains of the spot were uniform for the frictionless case and increasing slightly for the frictional case. This general trend of Figure 2.17 is in good agreement with their experimental results shown in Figure 2.18.

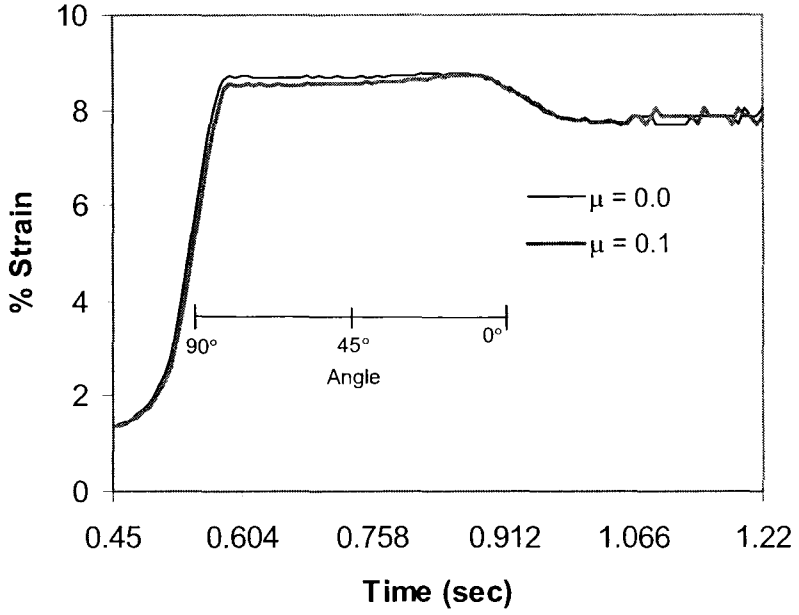

Figure 2.17 Longitudinal strain changes of one spot during the step 3 simulations.

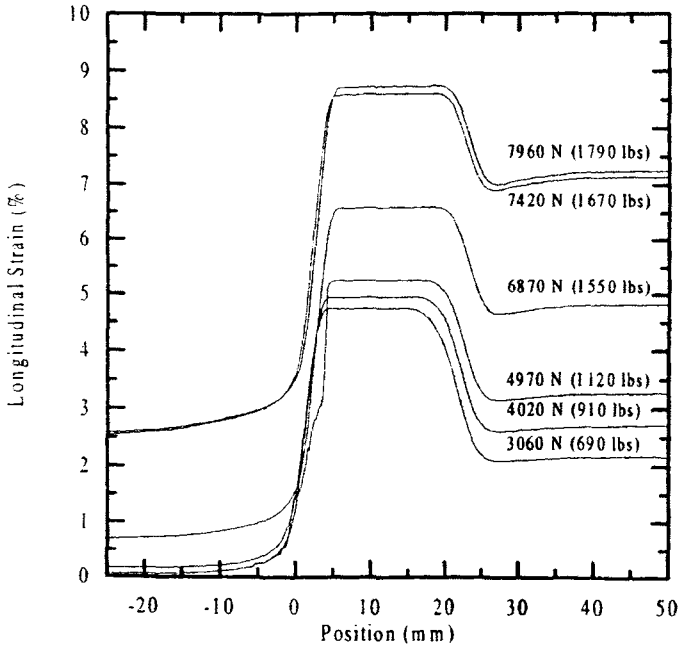

Figure 2.18 Measured longitudinal strain changes as a function of position from tests with free roller (Alinger et al., 1999).

2.3.3. Tension Forces and Friction Coefficient

Since the simulation loads the strip by displacement control, the applied tension forces were obtained from the group of elements at the inlet and outlet ends by integrating of longitudinal stresses over the element areas. Figure 2.19 shows the tension forces from simulations for frictionless and frictional cases. The difference between the outlet and inlet tension forces from the frictionless case represents the bending force, and the difference from the frictional case represents the combination of bending and frictional forces. To calculate the friction coefficient from the force data, the last 25% portion of the data, which is regarded as being in a steady state, was curve-fitted by linear regression as shown in Figure 2.20. The bending forces were obtained from the fitted forces of frictionless case by subtracting the inlet forces from the outlet forces. Then, the resulting bending forces with the fitted inlet and outlet forces of the frictional case were applied to Equation (2.3) and the friction coefficients were calculated.

The bending forces were found to lie in a range of 99 N to 105 N, which can also be estimated by Swift's methodology using Equation (2.1) from the yield stress and the geometry of the strip. The estimated value (107 N) is close to the bending forces obtained from simulations. The friction coefficients acquired from simulations were $\mu = 0.096$ which were 4% lower than the friction coefficient ($\mu = 0.1$) applied in the simulations. It appears that the Equation (2.3) works well in predicting the friction coefficient in spite of the non-uniform contact pressure distributions observed in the previous section.

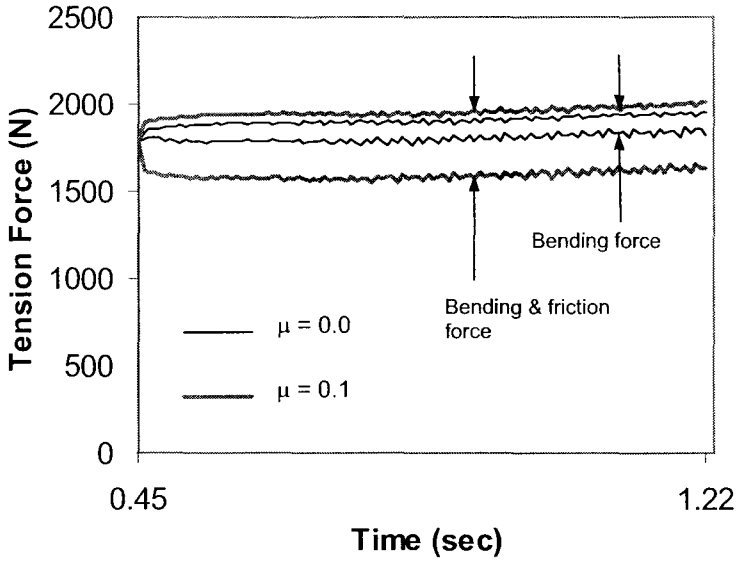

Figure 2.19 Tension forces during step 3 simulations.

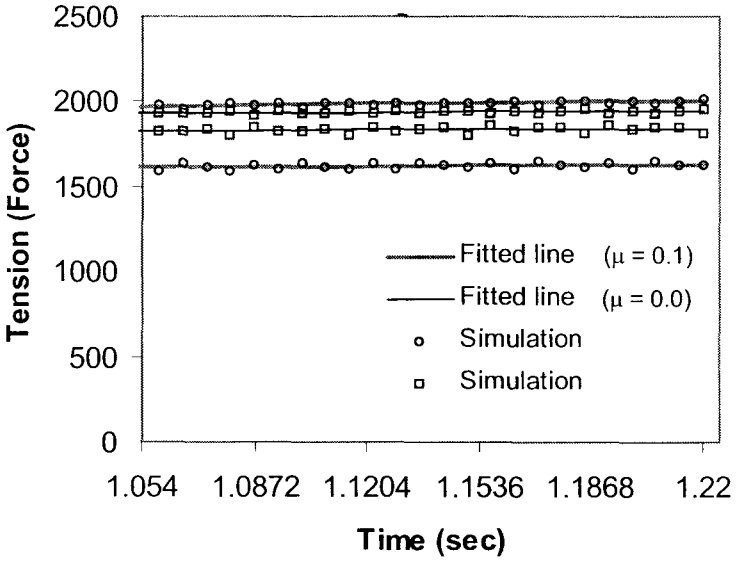

Figure 2.20 Linear regression of the tension forces.

2.4. Summary

2.4.1. Contact Pressure Distribution

Quite non-uniform pressure distributions on the pin/strip contact area (Figures 2.6 and 2.7) were observed. There were pressure peaks near the inlet and outlet regions, and near the strip edges. The observed phenomena differ from the simple rope analogy expectation, that is uniform pressure distribution over the contact.

2.4.2. Strain Distribution

Beginning with a rather uniform strain distribution as a result of the pre-bending operations (steps 1 and 2 in Figure 2.4), a non-uniform and transient strain distribution is shown to develop as the strip slides, and finally the uniform and steady condition is reached (Figures 2.11 and 2.12). In the present simulations, the steady condition was reached after the strip slid the distance that is about 1.5 times to the length of wrap around the pin.

Strain is generated mostly at the inlet and outlet regions of the strip and remains rather constant in the middle. This is different from the important assumptions of Wilson et al. (1991) that the strain is generated in a linearly increasing manner at the contact for their application of the draw-bend test to measure the strain-rate dependence of friction.

2.4.3. Friction Coefficient Estimation

The Equation (2.3) that originating from the rope analogy performed well in estimating the friction coefficient in spite of the observed non-uniform contact pressure distributions over the contact area and the contact angle (74°) that was less than 90°. The estimated friction coefficient (μ = 0.096) was 96 % of the simulation input friction coefficient (μ = 0.1).

CHAPTER 3

PRESSURE NON-UNIFORMITY AND ITS INFLUENCE ON FRICTION MEASUREMENT

3.1. Introduction

In the last chapter, various aspects of draw-bend friction test have been investigated using finite element simulations. Especially, pressure non-uniformity, which deviates from the underlying assumption for the conventional friction calculation method, has been observed. In this chapter, the influence of the observed pressure non-uniformity on the friction measurement will be investigated in more detail.

To study the effect of the pressure non-uniformity on friction measurements, a variable friction coefficient model, which is more realistic for the lubricated sheet metal contacts, is implemented into the finite element code and applied to the simulations. Then, draw-bend friction test cases for three different pin diameters are simulated with the implemented variable friction model.

3.2. Stribeck Friction Model

It is well known that the friction coefficient is a function of process variables such as contact pressure, sliding velocity, and lubricant viscosity. For lubricated surfaces, the friction coefficient can be described with a Stribeck curve (Stribeck, 1902) as shown in Figure 3.1. In Stribeck curves, the friction coefficient μ is plotted against a dimensionless lubricant number L, which is given by

$$L = \frac{v\eta}{PR_a} \tag{3.1}$$

where v is sliding velocity, P is contact pressure, η is lubricant kinematic viscosity, and R_a is surface roughness of the sheet material. The Stribeck curve can be fitted by the following function (Ter Haar, 1996).

$$\mu(L) = 0.5 \cdot \left[\left(\mu_{BL} + \mu_{EHL}\right) + \left(\mu_{BL} - \mu_{EHL}\right) \cdot \tanh \left(\frac{\log_{10}\left(\frac{L^2}{L_{BL} \cdot L_{EHL}}\right)}{\log\left(\frac{L_{BL}}{L_{EHL}}\right)} \right) \right] \tag{3.2}$$

where μ_{BL} and μ_{EHL} are the friction coefficients at the boundary and hydrodynamic lubrication regimes. L_{BL} and L_{EHL} are the lubricant numbers at the transition between the two lubrication regimes. These parameters are experimentally determined by selecting the

parameters that best fit the friction test data. Emmens (1988) and Ter Haar (1996) obtained Stribeck friction curves for various steel strips with their strip-draw type friction experiments.

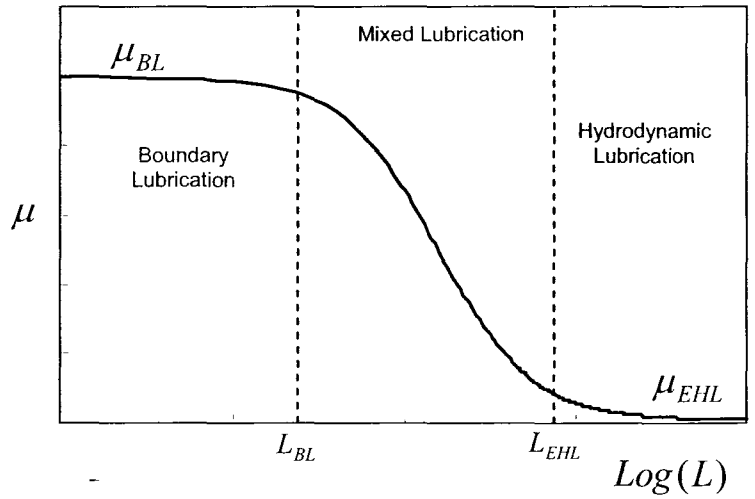

Figure 3.1 Stribeck friction curve (Tanh-fit).

3.3. Implementation and Verification of the Stribeck Friction Model

In the present work, the Stribeck friction model was implemented into the finite element code H3DMAP by modifying the existing Coulomb friction model. Instead of constant μ, Equation (3.2) was used to determine the variable μ, which is dependent on the local contact pressure and sliding velocity.

To test the applicability and accuracy of the implemented model, a strip-draw type friction test was simulated as shown in Figure 3.2. For the strip-draw study, the parameters shown in Table 3.1 were selected based on the experimental data by Ter Haar (1996) as inputs for Stribeck friction model. For the strip, the same sizes of section geometry and elements as the strip model for the draw-bend simulations were used and a flat die was modeled to simplify the analysis instead of the circular pin.

Table 3.1 Input parameters for Stribeck friction model

Parameters	Values
μ_{BL}	0.1
μ_{EHL}	0.001
L_{BL}	4.5×10^{-4}
L_{EHL}	5.4×10^{-3}
R_a	1.85 μm
η	1.2 Pa·s

The following steps were used in the simulation procedures (refer to Figure 3.2), which are close to the draw-bend simulation,

Step 1) While fixing the outlet end, the inlet end moves backward applying the tension to the strip.

Step 2) A force F_N is applied to the flat die to generate the pressure on the strip.

Step 3) Both ends move with the same velocity and the tension forces, F_1 and F_2, are obtained.

Then the friction coefficients are calculated from the obtained forces by $\mu = (F_1 - F_2)/F_N$. The values of μ obtained from simulations with various pressure F_N and velocity v values should conform to the input Stribeck curve to demonstrate the applicability and accuracy of the implemented friction model.

Two numerical problems were encountered in the verification simulations, both of which involve details of local data with the contact algorithm. Left unattended, these problems cause serious excursions in pressure and velocity that prevent successfully using Stribeck model. These problems were solved as described in the following sections.

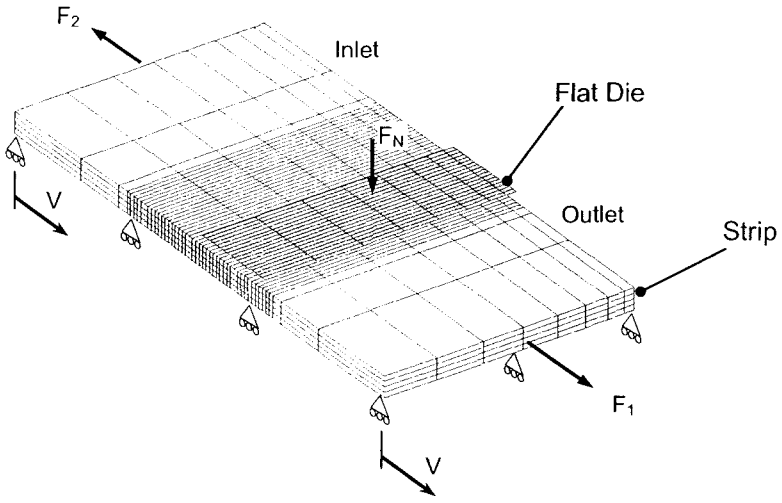

Figure 3.2 Strip-draw friction test model.

3.3.1. Problem in Pressure Distribution and its Solution

The first problem was the non-uniform pressure distribution as shown in Figure 3.3 (a). Pressures are higher at the edges. Because the friction coefficient in the Stribeck friction model depends on contact pressure, the incorrect contact pressure distribution can give an erroneous result.

As an explicit finite element code, H3DMAP uses the penalty method to impose the constraints on the contact boundaries, which is widely used for the large deformation problems (Sauvé et al., 2002). The basic concept of the penalty method can be explained in terms of linear compression-only springs at contact boundaries. Therefore, the stiffness of the spring (penalty stiffness) has decisive effects on the contact stress distribution. To obtain the correct contact pressure distribution a proper penalty stiffness option has to be used.

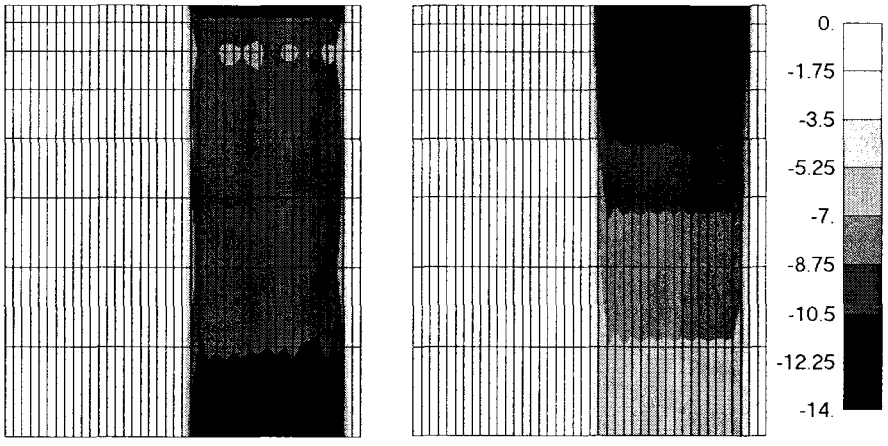

(a) master area option **(b)** slave area option

Figure 3.3 Pressure distribution in the strip (target pressure : 10 MPa).

The following summarizes how the uniform pressure was obtained using the proper penalty stiffness option.

1) Among interface stiffness options, an option that selects the penalty stiffness based on the slave segment area instead of master segment area was used. The details on this option are explained in (Shi and Metzger, 2001).
2) Equal-sized elements were used for the flat die, which was defined as a slave surface. Even with slave node area option in 1), the pressure distribution was non-uniform as shown in Figure 3.3b, and it was found that one of the slave and master surfaces has to have equal-sized elements for the uniform pressure distribution.
3) The number of elements for the die was increased to 25 from 8 in height direction, so that the element size in slave surface is finer than the element size in master surface (strip) at every contact interface. If not, the master nodes penetrate into the slave surfaces and pressure becomes non-uniform. The resulting uniform pressure distribution from the mesh refinement of the die is shown in Figure 3.4.

By defining the strip as a slave surface and the die as a master surface, a uniform pressure distribution was also achieved with coarse equal-sized elements in the die. In this way, the step 3) could have been skipped and a lot of elements could have been saved in die model. However, the current code calculates the penalty stiffness once at the start of the simulation based on the initial slave segment area because calculating the stiffness at every time step is expensive. In the draw-bend simulations, element size in the strip changes when the strip slides and bends around the pin. Therefore the die and pin were

defined as slave surfaces for both the verification simulations and the draw-bend simulations aimed at avoiding the possible errors from using the initial geometries to calculate the contact stiffness of the deformed states of a strip.

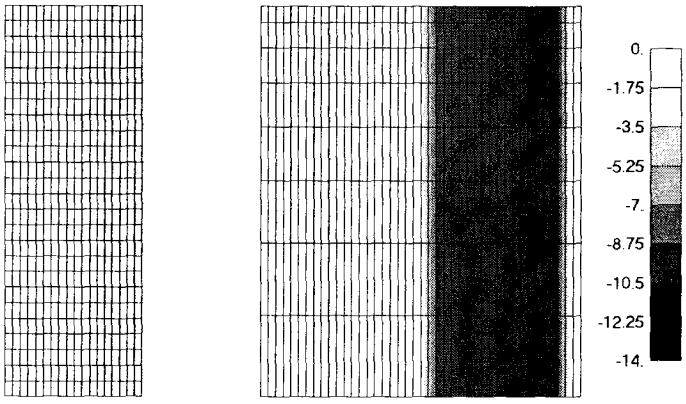

(a) meshes for flat die **(b)** pressure in the strip

Figure 3.4 Pressure distribution in the strip (target pressure : 10 MPa).

3.3.2. Problem in Velocity Calculation and its Solution

The second problem with the Stribeck friction model was the fluctuation in the nodal velocity as the strip slides over the die. Figure 3.5 shows the velocity data collected from a node of the strip during the strip-draw simulation with the Stribeck model. In the first half of the graph, the strip was stretched and normal force was applied (steps 1 and 2). Then the strip moved with the velocity (v = 8 mm/sec). The velocity fluctuation was not observed with the Coulomb friction model (μ=0.1) as shown in Figure 3.6. Due to the severe velocity fluctuation (-10 to 30 mm/sec), the friction coefficients obtained from the

strip-draw simulations with Stribeck friction model didn't match well with the original input.

In the Stribeck friction curve, the friction coefficient increases with a decreasing velocity (see Equation 3.1 and Figure 3.1) and this characteristic of the implemented friction model causes the velocity fluctuation. Because of the dynamic procedure of the explicit method, the velocity fluctuations always exist, although they should be negligible for the quasi-static applications like the simulations in this study. When the boxed part of Figure 3.6 is enlarged, the minor fluctuation is noticed. The Stribeck friction model amplifies this fluctuation by applying an increased friction force to the contact nodes with lower velocity and by applying a reduced friction force to the nodes with higher velocity.

In the current contact algorithm with the Stribeck model, the relative velocity is calculated for contacting slave nodes in each time step and the friction coefficient is updated based on the velocity at each time step.

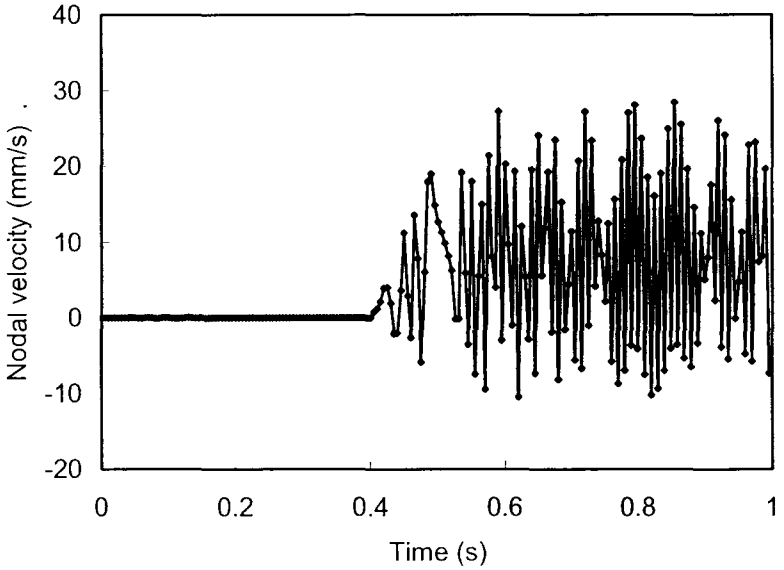

Figure 3.5 Nodal velocity fluctuation with Stribeck friction.

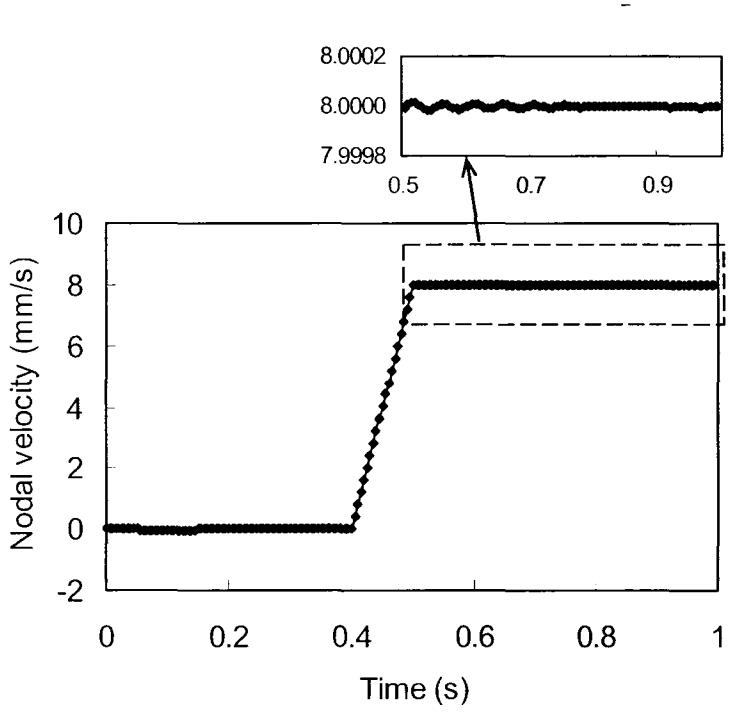

Figure 3.6 Nodal velocity with Coulomb friction.

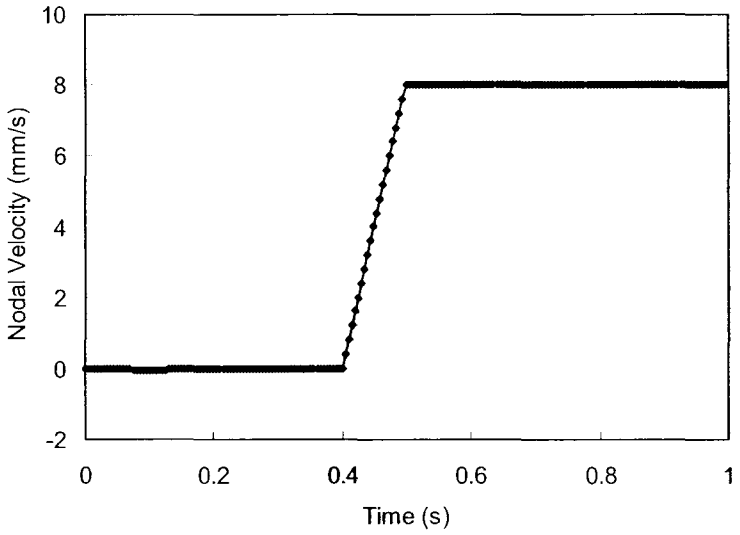

Figure 3.7 Nodal velocity with Stribeck friction after solving velocity fluctuation problem.

The problem has been solved by updating the friction coefficient at some interval, and not at each time step, using the same friction coefficient within the interval. The average velocity over the time interval was calculated and the friction coefficient was updated based on the average velocity. For the current simulations, the interval of 100 time-steps gave the successful results. This is about 0.01% of the total time-step numbers (738,108 steps) so that velocity is still updated with relatively high frequency. Figure 3.7 shows the velocity from the simulation with the Stribeck friction determined by this method.

3.3.3. Friction Model Verification Result

The strip-draw simulations were performed with the velocity and pressure values shown in Table 3.2. The values were selected so that a wide range of the Stribeck curve can be tested. For case 5, the mass scaling was reduced to a value of 10 from an earlier value of 1000 to avoid possible dynamic effects.

Figure 3.8 shows the plots of the original input Stribeck curve and obtained friction coefficients. The original input curve was well reproduced from the simulations, thus demonstrating the applicability and accuracy of the Stribeck friction model as implemented in the finite element code.

Table 3.2 Simulation cases for model verification

Case	Pressure (MPa)	Velocity (mm/sec)
1	10	8
2	5	8
3	10	0.8
4	1	8
5	5	80

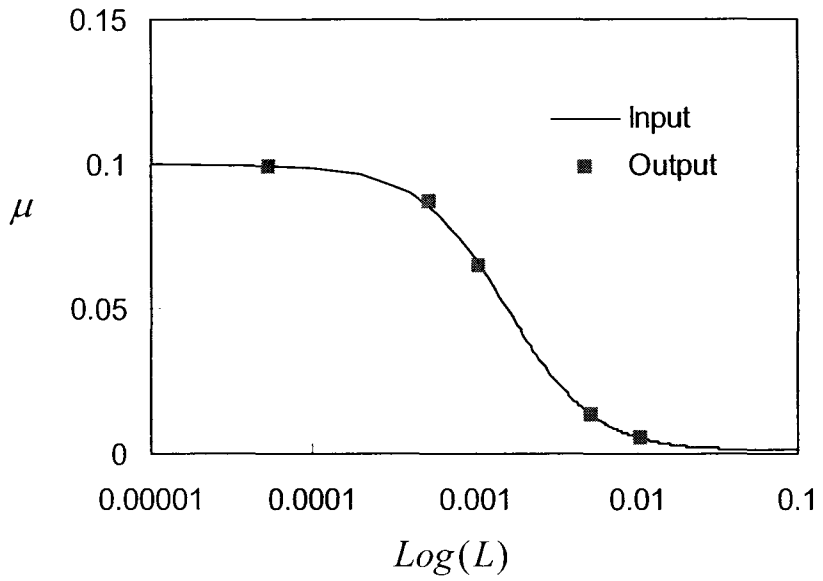

Figure 3.8 Input Stribeck curve and friction coefficients reproduced from simulations.

3.4. Draw-Bend Friction Test Simulations

FE models were prepared for three different pin diameters (12.7 mm, 25.4 mm, 38.1 mm) as shown in Figure 3.9. Top halves of the geometries were modeled to exploit the symmetry condition. In the 12.7 mm diameter pin case, the strip consisted of 3,744 3D (brick) elements (four elements through the thickness). In the longitudinal direction of the strip, mesh was refined (100 elements in 25 mm distance) at the region where the strip would experience the bending and unbending deformation as shown in Figure 3.9. A smaller number of elements (eight) were used over the width because the deformation in this direction is minor compared to the longitudinal direction. The pin was modeled as a

rigid surface with 2D elements. In the other two cases (25.4 mm, 38.1 mm diameter pins), the length of the finely meshed part was increased to 50 mm and 75 mm while keeping mesh sizes equal to the 12.7 mm diameter pin case. The same stress-strain data used for simulations in Chapter 2 and an isotropic elastic-plastic material model were used.

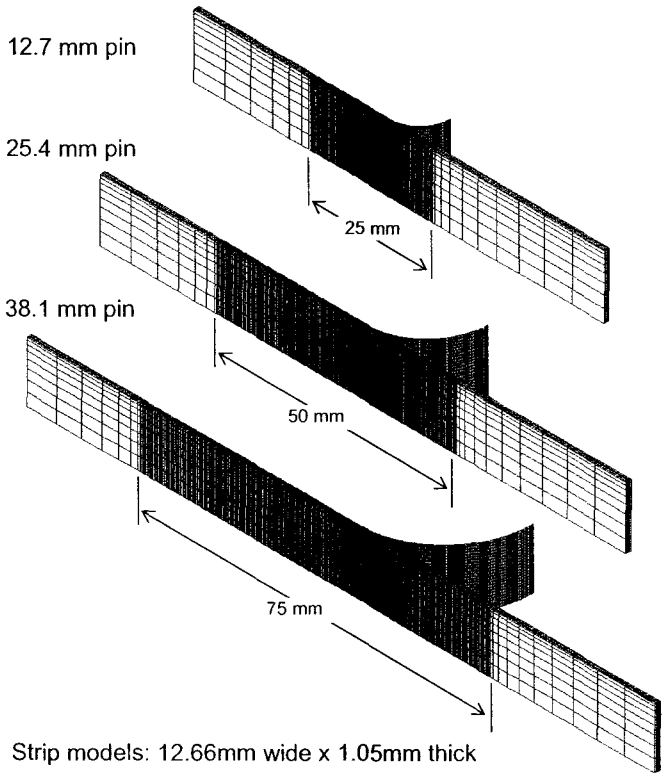

Figure 3.9 Finite element models for draw-bend friction test simulations.

All simulations were performed with the implementation in H3DMAP, and the simulation procedures were the same as the simulation presented earlier in Chapter 2 except that a constant back tension force was applied in the simulations here. Beginning with the unbent strip model, the simulation was performed with the following procedures.

Step 1) While fixing the inlet end, the outlet end is loosely bent around the pin by applying a circular motion to outlet end nodes.

Step 2) In step 2, nodes at the outlet end move until the inlet tension force (back tension) reaches a certain value (to achieve an average contact pressure of 10 MPa).

Step 3) In step 3, the outlet end moves with a defined velocity (50 mm/sec) while the inlet end follows with a constant tension force.

3.5. Simulation Results

The draw-bend test simulations were performed with the implemented Stribeck friction model for different pin diameters shown in Figure 3.9. Simulations were also performed with a Coulomb friction model and for a frictionless condition.

3.5.1. Simulation Inputs and Conditions

For the input Stribeck curve, the friction experiment data with steel strip by Ter Haar (1996) were used (Table 3.3). The experimental data from steel strip would work for the purpose of the study in this chapter for the evaluation of the test analysis method even though they are not from aluminum strips. Simulations were performed with different back tension forces to achieve the average contact pressure of 10 MPa for each pin size, applying the Equation (3.1). Because of the increased area of contact, greater tension forces were required for larger pins to obtain the same average contact pressure. In simulations with a Coulomb friction model, a constant of 0.1 was applied for the friction coefficient. For Coulomb friction and frictionless cases, the simulations were run with the same back tension forces as in the Stribeck friction cases.

Table 3.3 Input parameters for Stribeck friction model (Ter Haar, 1996)

Parameters	Values
μ_{BL}	0.131
μ_{EHL}	0.001
L_{BL}	4.5×10^{-4}
L_{EHL}	5.4×10^{-3}
R_a	1.85 μm
η	1.2 Pa s

3.5.2. Tension Forces and Friction Coefficient Calculation

Figures 3.10, 3.11, and 3.12 show the outlet tension forces at step 3 for Stribeck friction, frictionless, and Coulomb friction cases compared to the applied back tension force for each of the pins. The first unsteady portions of them have less physical meaning because friction conditions were applied only in step 3 after the steps 1 and 2 had been run under frictionless conditions.

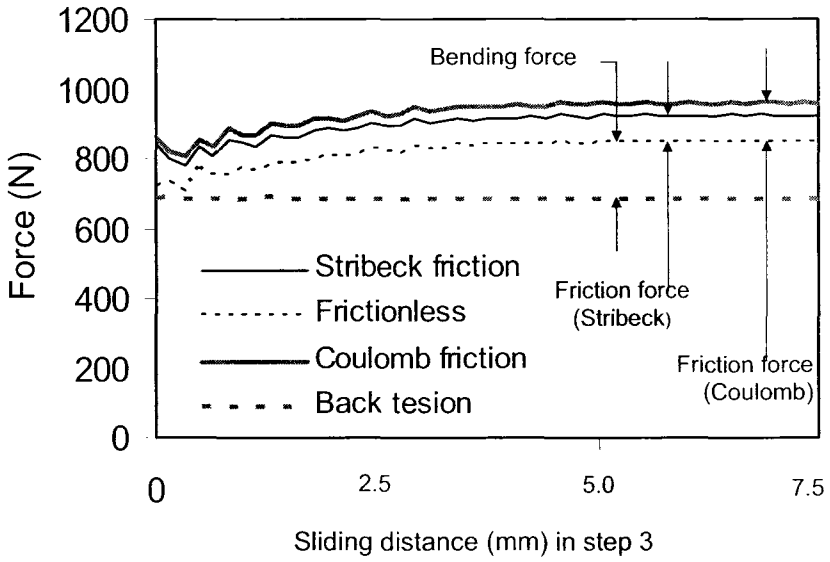

Figure 3.10 Tension forces at step 3 for 12.7 mm diameter pin.

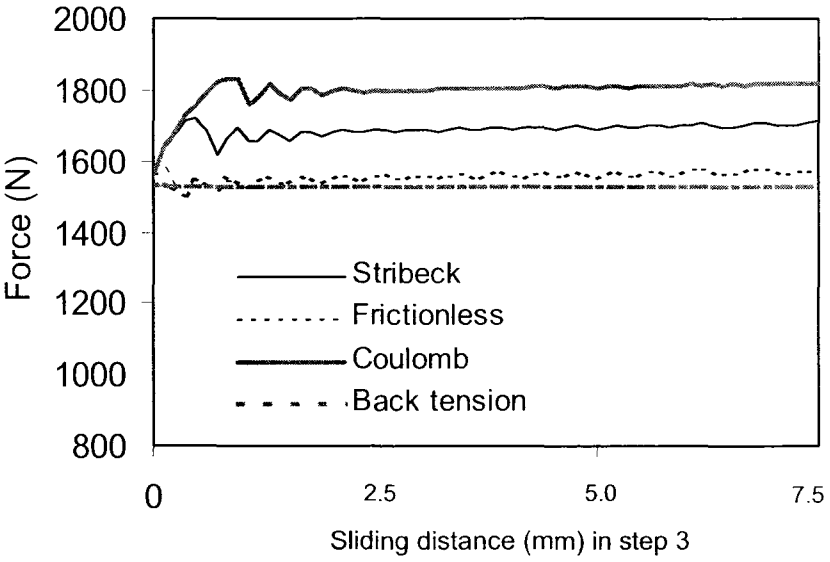

Figure 3.11 Tension forces at step 3 for 25.4 mm diameter pin.

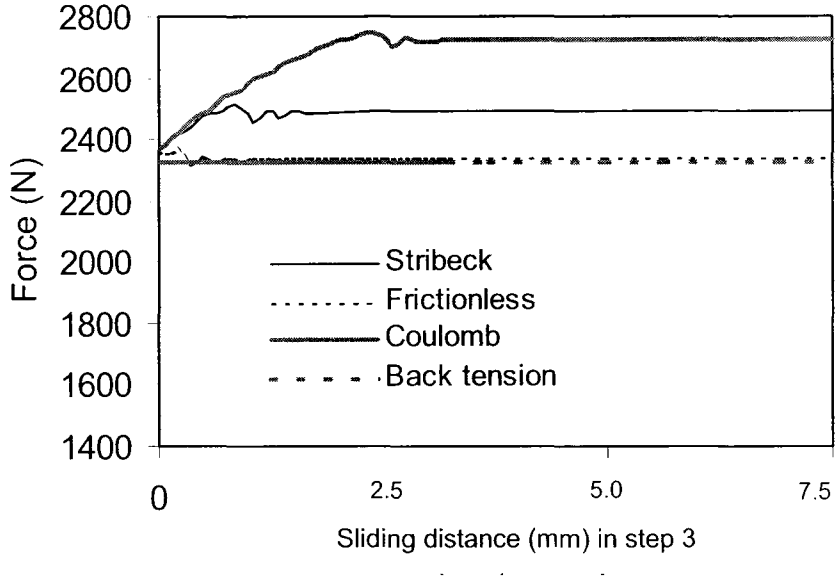

Figure 3.12 Tension forces at step 3 for 38.1 mm diameter pin.

Tension forces were decided by averaging the last one-third portion of the data, which is regarded as being in a steady state, and the friction coefficients were calculated from the tension forces using Equation (2.3). Figure 3.13 shows the calculated friction coefficients for three pin diameters with Coulomb and Stribeck friction models.

In the Coulomb friction cases, the input friction coefficient of 0.1 was well retrieved (95 to 97%). But in the Stribeck friction cases, the obtained coefficients decreased monotonically for the increasing pin diameters even though the simulations were performed with the same average contact pressure (10 MPa) and Stribeck friction input data. The results are in agreement with experimental observations (Kotchman et al., 1992; Saha and Wilson, 1993; Han, 1997; Keum et al., 2004). In Figure 3.14, the

calculated friction coefficients are compared with the input Stribeck curve. The dotted line shows the simulation conditions and the friction coefficient decided by the Stribeck curve with the conditions. This graph shows that the obtained friction coefficient comes close to the coefficient based on the Stribeck curve.

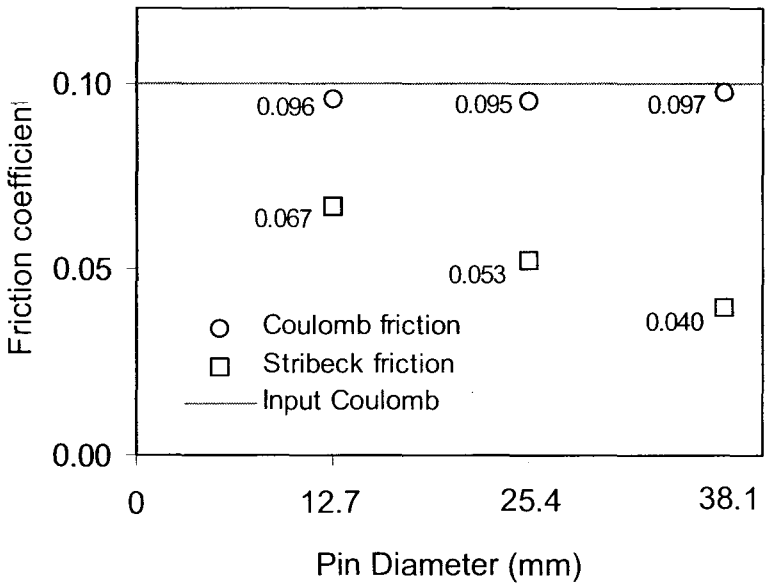

Figure 3.13 Friction coefficients calculated from tension forces.

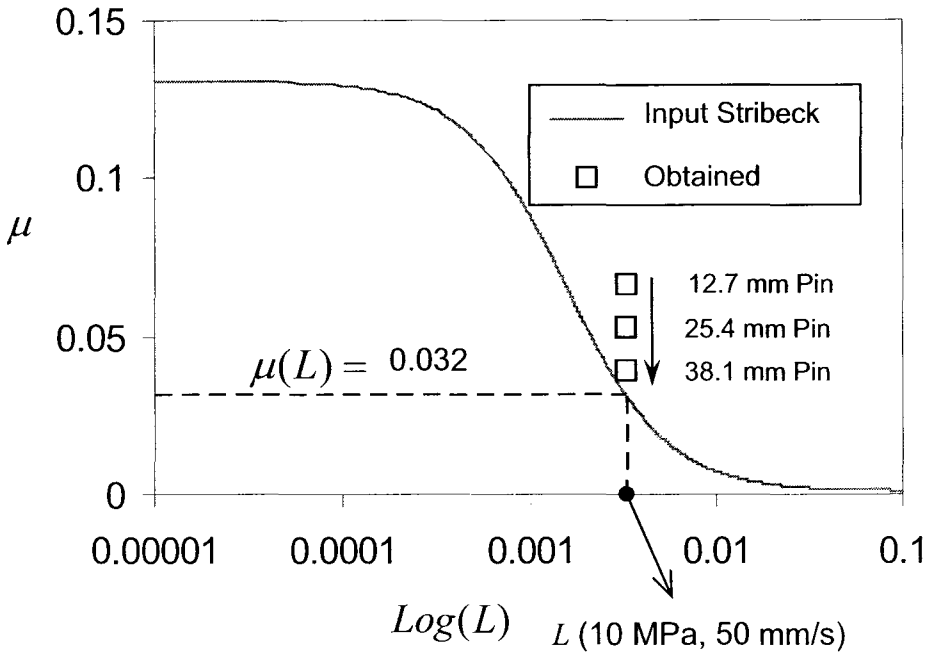

Figure 3.14 Input Stribeck curve and obtained friction coefficients.

3.5.3. Contact Pressure Profiles

Local axis systems were defined for elements in the strip model. These axes rotate with elements through deformation and the stress component in through-thickness direction at the contact interface were taken as the contact pressures. Figure 3.15 shows the contact pressure distribution of the 12.7 mm diameter pin case with Stribeck friction at an instant shown on the small picture. The difference in pressure distribution between Stribeck and Coulomb friction cases were minor. The pressure profiles are quite non-uniform both in longitudinal and transverse directions. The real contact angle is much less than the geometric wrap angle of 90°. Also, there is no contact along the strip edge because of the outward deformation of the strip edge, which is known as the anticlastic curvature of a bent strip.

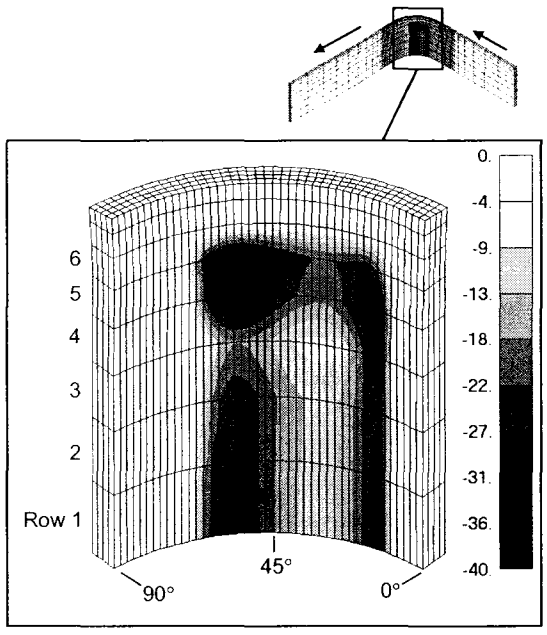

Figure 3.15 Contact pressure distribution (in MPa) for 12.7 mm diameter pin with Stribeck friction.

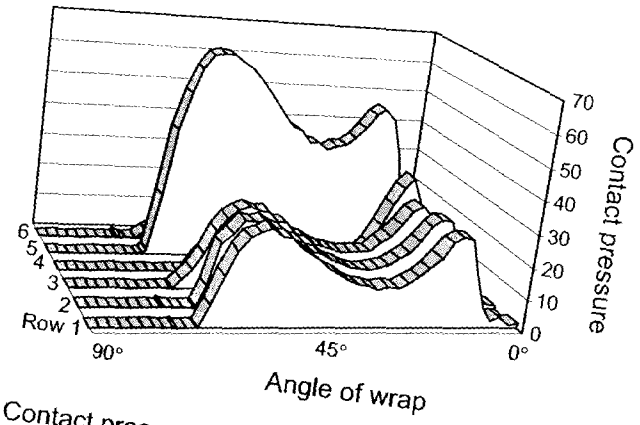

Figure 3.16 Contact pressure (MPa) profiles for 12.7 mm diameter pin.

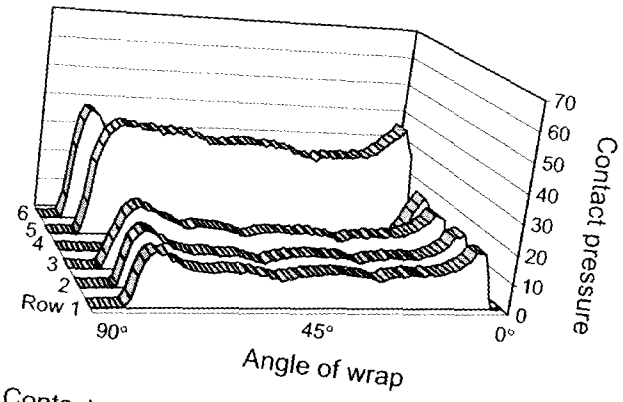

Figure 3.17 Contact pressure (MPa) profiles for 25.4 mm diameter pin.

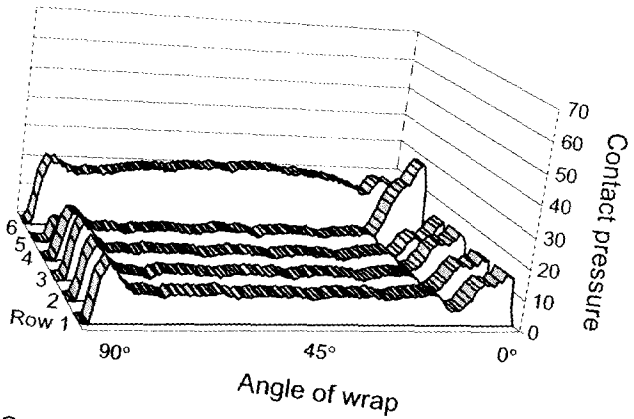

Figure 3.18 Contact pressure (MPa) profiles for 38.1 mm diameter pin.

In Figures 3.16, 3.17, and 3.18 contact pressure profiles of element rows are plotted for each pin diameter case. It is seen that in the 90° wrap angle area, the contact pressure profiles are quite different even though the average contact pressure was set equal to 10 MPa for all the cases. As the pin diameter increases, the real contact area spread closer to the geometric wrap area of 90° and contact pressure profiles become more evenly distributed at around 10 MPa.

The pressure profile changes depending on pin diameters explain the phenomena shown in Figure 3.14. Pressure peaks that appear in smaller diameters raised the friction coefficients in Stribeck model cases, where the friction coefficient increases as the contact pressure increases.

3.6. Discussion

A variable friction coefficient model (Stribeck friction), which is more realistic than constant friction coefficient model (Coulomb friction), was successfully implemented into the finite element code and applied to the draw-bend friction test simulations.

The simulation study showed that contact pressure profiles in the draw-bend test are non-uniform with less real contact angle than the geometric wrap angle. The non-uniformity becomes more severe with decreasing pin diameter, increasing the estimated friction coefficient. These phenomena observed from detailed simulations with Stribeck friction model account for the experimental observation of increase in the measured friction coefficient as the pin diameter is decreased (Kotchman et al., 1992; Saha and Wilson, 1993; Han, 1997; Keum et al., 2004).

The study in this chapter implies that the analysis method based on rope/pulley analogy has shortcomings for measuring a friction coefficient as a function of pressure and the error will increase as the diameter of applied pin is decreases. In next chapter, a new methodology to interpret the draw-bend test data will be introduced. The pressure non-uniformity, which persists in draw-bend friction tests, is exploited to measure the pressure dependency of friction coefficient in the new approach.

CHAPTER 4

NEW METHOD TO DETERMINE FRICTION COEFFICIENTS

4.1. Introduction

The conventional method to estimate the friction coefficient from the test data is based on the following two assumptions, which are the characteristics of a flexible rope sliding over a cylindrical pin.

1) The pin/strip contact angle is equal to the geometric wrap angle.
2) The pressure distribution at the contact is uniform.

However, these assumptions are not true due to the stiffness of sheet metals. Alinger et al. (1999) measured the strains on the outer surfaces of metal strips through the test and noticed that the real contact angle is less than a geometric wrap angle. Coubrough et al. (2002) observed the existence of pressure peaks at the pin/strip contact by using a contact sensor on the pin. Figure 4.1 shows the pin unit with contact sensor and the obtained sensor output from their experiment. They also observed that the real contact angle is less than the geometric wrap angle.

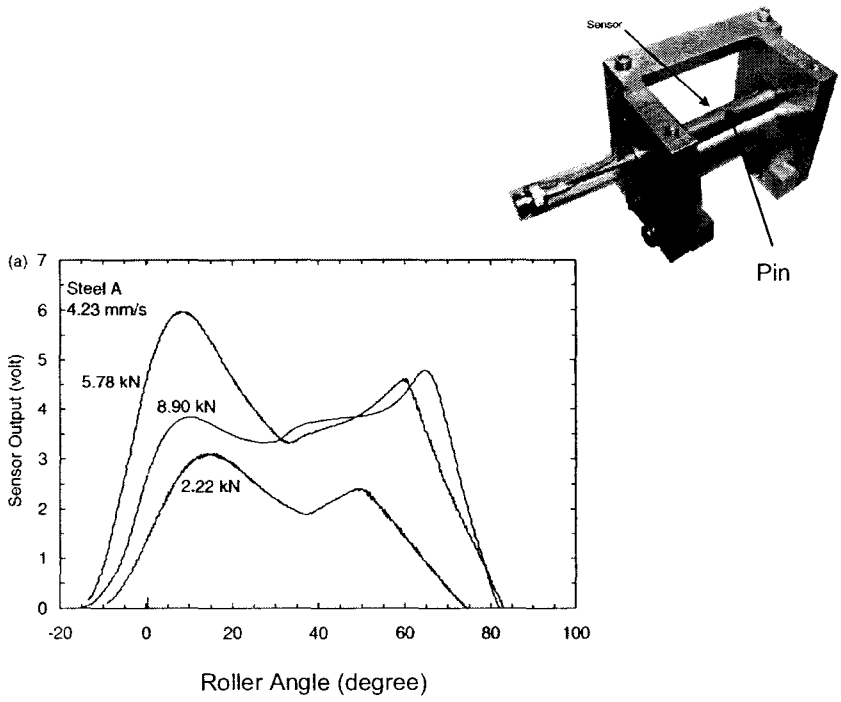

Figure 4.1 Experimental evidence of non-uniform pressure (Coubrough el al., 2002).

The finite element study as described in the previous chapters clearly revealed and quantified the phenomena concerning wrap angle and pressure variation. The conventional method, which assumes uniform pressure distribution to estimate friction coefficients from draw-bend friction tests, has been evaluated and it is concluded that the conventional method is valid only for measuring an average friction coefficient over the pressure range, which exists in the specific draw-bend system.

In this chapter, a new method to extract non-constant friction coefficients from draw-bend friction tests is suggested. In this method, contact pressure maps obtained from simulations, instead of the uniform pressure assumption, are included in the analysis of

test data to account for the pressure dependency of friction coefficient. The method is tested by applying the method to back predict the input friction data from finite element simulation results of draw-bend friction tests, in which non-constant friction models are used as friction input.

4.2. Contact Pressure Maps from Simulations

Simulations were performed closely following the general procedure of the draw-bend test. In step 1, while fixing the inlet end, the outlet end was loosely bent around the pin by applying a circular motion to outlet end nodes. In step 2, nodes at the outlet end were moved until the inlet tension (a back tension stress of 57 MPa for the simulations in this chapter) reached a certain value. In step 3, the outlet end moved with a defined velocity (50 mm/s) while the inlet end followed with a constant tension force. Steps 1 and 3 have been performed by the normal explicit dynamic approach without applying damping. Artificial damping is often applied in explicit methods to smooth out dynamically induced vibrations, but here such damping will introduce error into the force required to drive the motion. But for step 2, the dynamic relaxation (Sauvé and Metzger, 1995) method has been applied so that any dynamic response aroused by steps 1 and 2 can be damped out before starting step 3. Thus, the main process of the draw-bend friction test, step 3, can begin without undue numerical noise.

In the current simulations, analytical pin surfaces were defined as master surfaces and the strip surfaces as slave surfaces for pure master-slave contact algorithm, in that the contact forces and pressures are calculated for each contacting node on slave surfaces at each iteration of the explicit solution loop. The contact pressure information was obtained for the slave nodes on the 90° wrap area of the strip and plotted in Figures 4.2, 4.3, and 4.4, where x, y domain is the locations of slave nodes and z axis is contact pressure P.

As can be seen from the Figures 4.2-4.4, contact pressure peaks appear near the entry and exit points of the strip to the pin/strip contact region, where the curvature of the strip inner surface changes from infinite to the radius of the pin. There are also pressure peaks along the strip edges due to so called anticlastic deformation of bending strips (Wang et al., 2005).

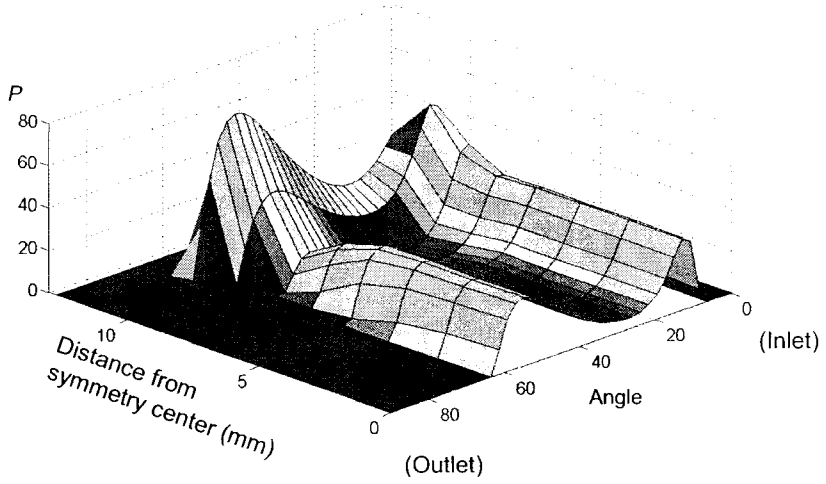

Figure 4.2 Pressure (MPa) map from 12.7 mm diameter pin simulation (frictionless).

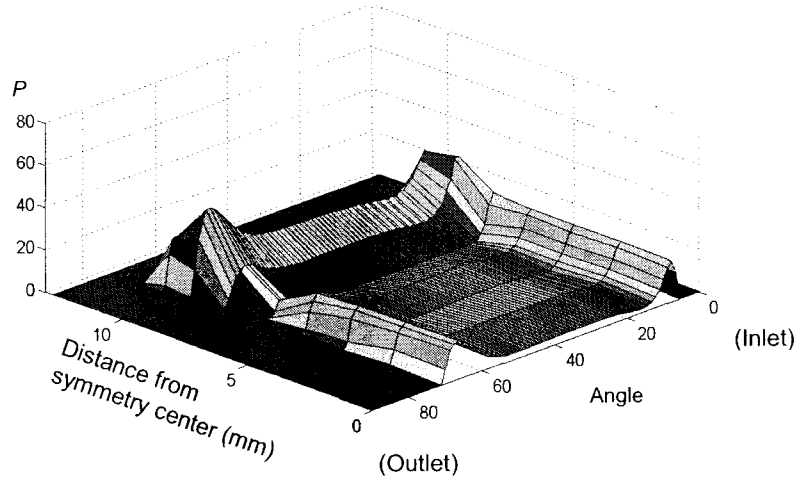

Figure 4.3 Pressure (MPa) map from 25.4 mm diameter pin simulation (frictionless).

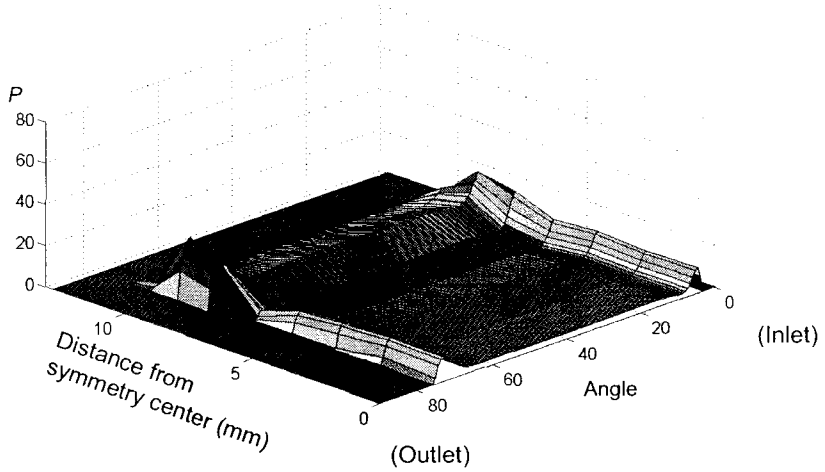

Figure 4.4 Pressure (MPa) map from 42 mm diameter pin simulation (frictionless).

To simulate the fixed pin cases, a Stribeck friction model implemented in chapter 3 is applied. Figure 4.5 shows the pressure maps from simulations with the Stribeck

friction model compared to the pressure maps from simulations without friction. The profiles of pressure maps are decided mainly by the stiffness of a strip, the size of pin, and the applied back tension force. It can be seen that the pressure maps keep their general shapes while the overall magnitudes increased slightly due to the increase of outlet tension forces by friction forces. As can be noticed from Equation (2.2) the magnitude of average pressure is proportional to the outlet tension force at the same back tension condition of this study. The pressure profile shape is not much affected by the applied friction because friction forces are applied in tangential directions of contact surfaces while pressure forces in normal to contact surfaces. This allows for the possibility of approximating the pressure distribution without detailed prior knowledge of the friction.

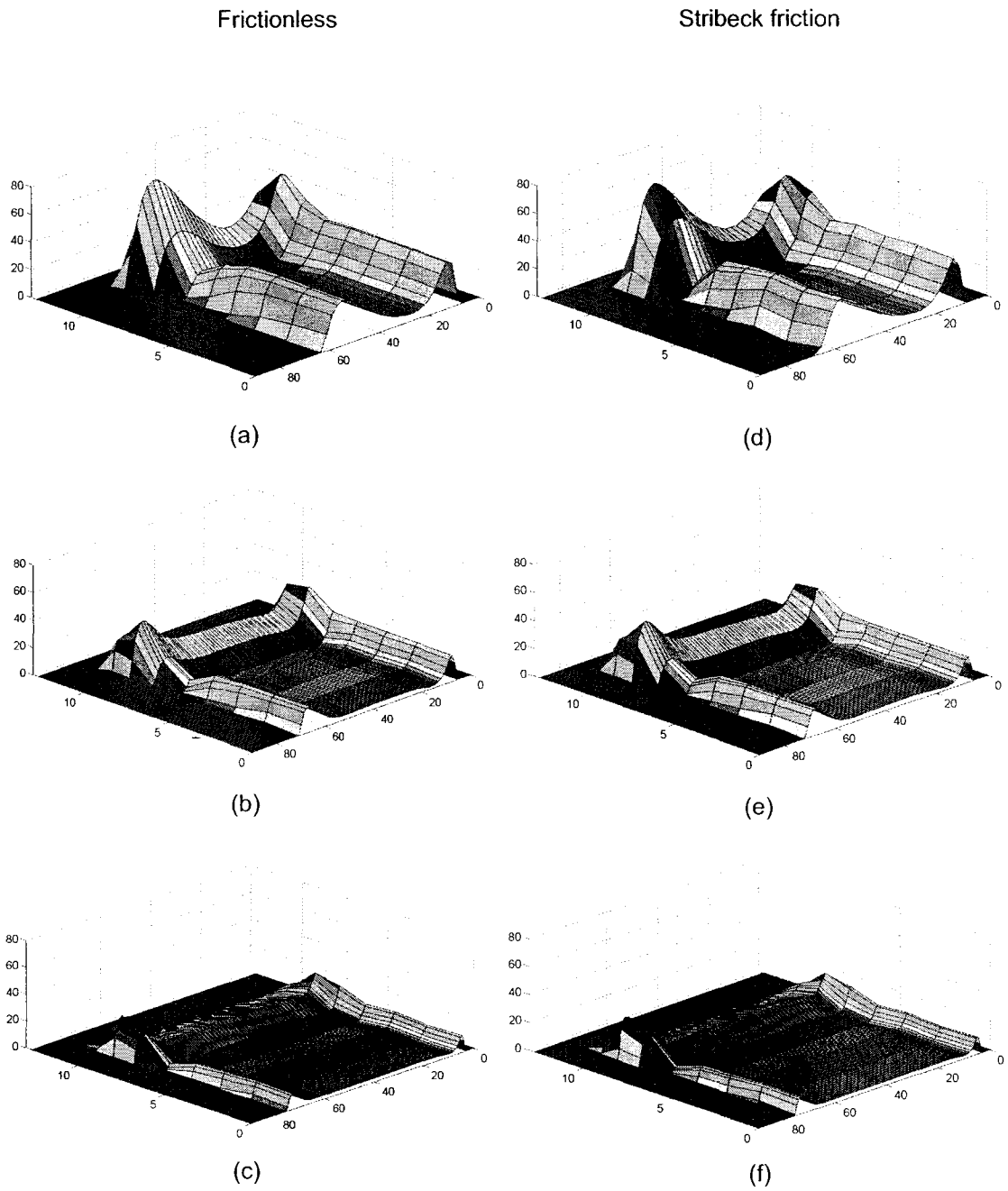

Figure 4.5 Pressure (MPa) maps from simulations for frictionless and Stribeck friction
(a) 12.7 mm diameter pin, (b) 25.4 mm diameter pin, (c) 42 mm pin diameter pin
(d) 12.7 mm diameter pin, (e) 25.4 mm diameter pin, (f) 42 mm pin diameter pin.

Figures 4.6, 4.7, and 4.8 show the outlet tension forces from frictionless and Stribeck friction simulations compared to the applied back tension force for the 3 pin diameters. The bending force F_B had been obtained from the difference between the outlet tension force F_Y' of the frictionless simulation and the back tension force F_X for each pin case. Then the friction coefficients were estimated with the force data from the Stribeck simulations by the conventional method using Equation (2.3) and the result is shown in Figure 4.9.

Even though the applied friction model (Stribeck) was the same, the obtained friction coefficient decreases as the pin diameter increases. This is because the conventional method does not consider the pressure dependency of the friction even though the input friction model was a pressure dependent function. It agrees with the experimental observations (Zheng and Overby, 1988; Kotchman et al., 1992; Saha et al., 1996; Han, 1997; Keum et al., 2004; Deng and Lovell, 2000) and shows the shortcomings of the conventional method in addressing pressure dependent friction.

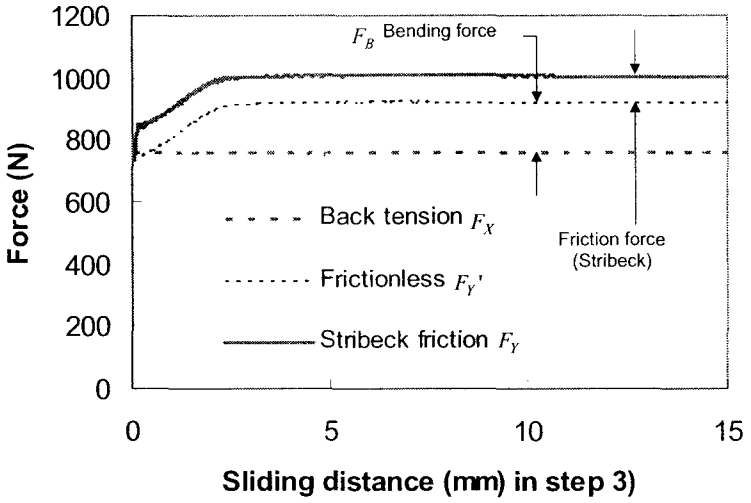

Figure 4.6 Tension forces during step 3 for 12.7 mm diameter pin.

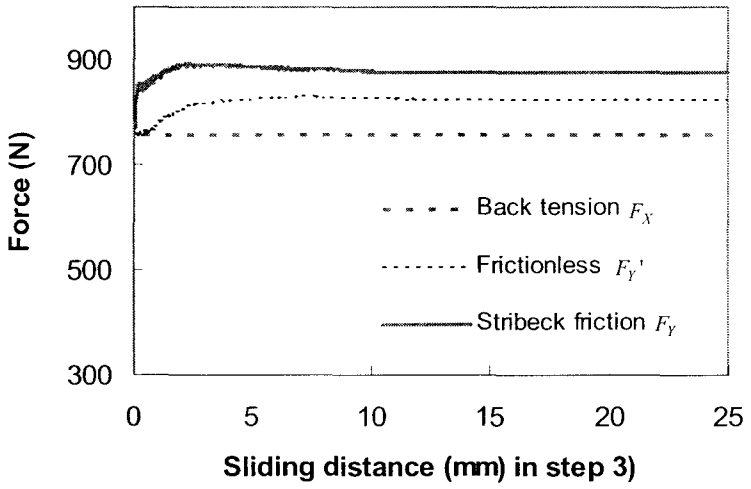

Figure 4.7 Tension forces during step 3 for 25.4 mm diameter pin.

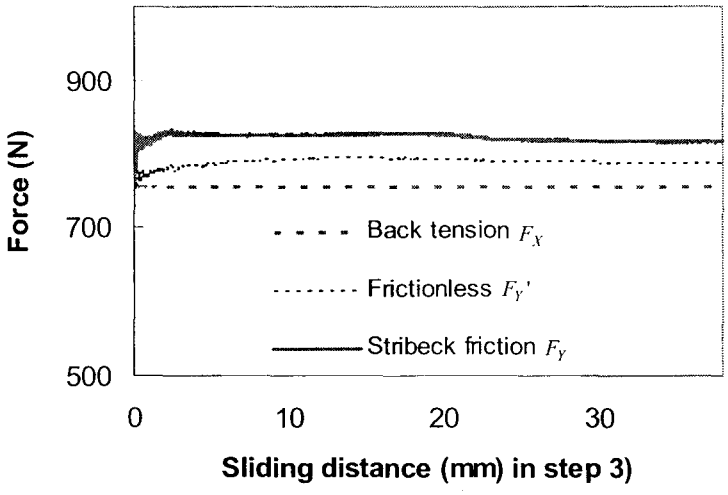

Figure 4.8 Tension forces during step 3 for 42 mm diameter pin.

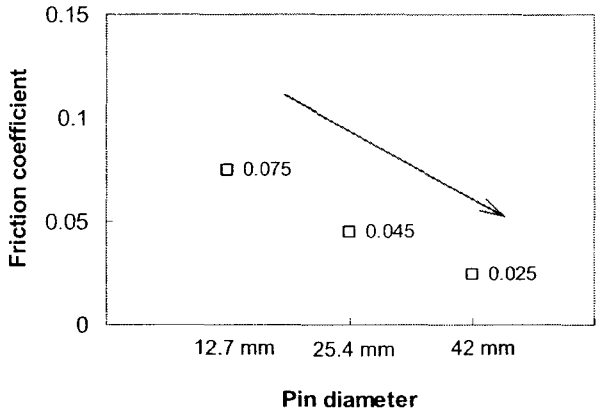

Figure 4.9 Friction coefficients estimated by the conventional method.

4.3. New Method to Determine Friction Coefficients

As mentioned in the previous sections, the conventional method (Equation 2.3) assumes a uniform pressure distribution, which is not valid for metal strips. This gives an average friction coefficient over the existing pressure range of a specific draw-bend system. In the new approach the pressure non-uniformity, which persists in draw-bend friction tests, is exploited to measure the pressure dependency of friction coefficient.

Previously, pressure maps for three pin diameter cases (12.7 mm, 25.4 mm and 42 mm) had been obtained from finite element simulations (see Figures 4.2-4.4). The accuracy of these pressure maps can be verified indirectly by comparing the tension force data between the experiments and simulations. At least the obtained pressure maps are much better approximations than the uniform pressure assumption of conventional method. With these pressure maps known a priori, any kind of friction model defined as a pressure dependent function can be applied and the resulting total friction forces can be calculated. Then the calculated total friction forces can be compared to the total friction forces from draw-bend friction experiments. The general procedure of the new approach is explained as follows.

1. Draw-bend friction experiments with fixed pins for different pin diameters (F_Y, F_X)

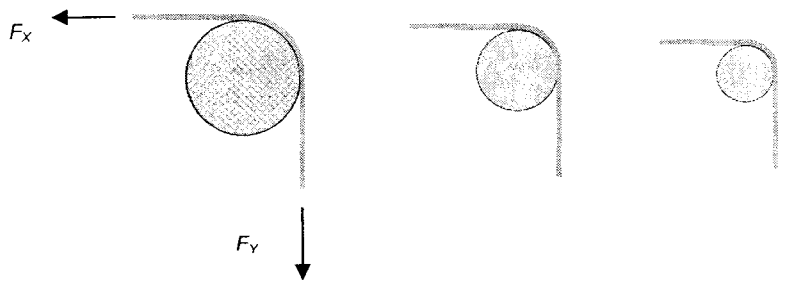

$F_Y - F_X = F_T$ (force from friction) + F_B (force from bending)

2. Draw-bend friction experiments with rotating pins (F_Y', F_X')

   1) Bending forces F_B are obtained by $F_B = F_Y' - F_X'$

   2) Friction forces F_T are obtained by $F_T = (F_Y - F_X) - F_B$

3. Draw-bend simulations for rotating pin cases

   1) Pressure maps are obtained from simulations for (P_i')'s and (A_i)'s

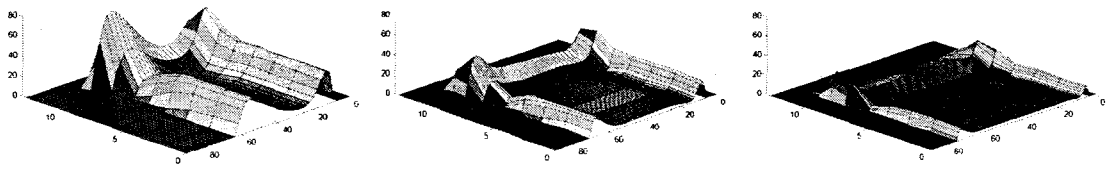

2) Friction forces F_T can be calculated using a friction model $\mu(P)$ as

$$F_T = \iint \mu(P) \cdot P \, dA \tag{4.1}$$

or in discrete forms

$$F_T = \sum_i \mu(c \cdot P_i') \cdot c \cdot P_i' \cdot A_i \tag{4.2}$$

where P and P_i' represent the contact pressures in fixed pin tests and the contact pressures from the frictionless simulations respectively, c is the total tension force ratio between the fixed pin test and rotating pin test, and (A_i)'s are the node areas of pressure map.

4. Minimize the following objective function to get optimum $\mu(p)$

$$f = \sum_j^n \left[(F_T^{\exp})_j - (F_T^{step3})_j \right]^2 \tag{4.3}$$

where n is the number of experimental cases.

If the friction coefficient is expressed as a second order polynomial function of pressure,

$$\mu(P) = a_0 + a_1 P + a_2 P^2 \tag{4.4}$$

the following matrix equation is obtained by taking partial derivatives of f with respect to a_0, a_1 and a_2 and setting to zero.

$$\begin{bmatrix} c_1 \sum_i P'_{i1} A_{i1} & c_1^2 \sum_i P'^2_{i1} A_{i1} & c_1^3 \sum_i P'^3_{i1} A_{i1} \\ c_2 \sum_i P'_{i2} A_{i2} & c_2^2 \sum_i P'^2_{i2} A_{i2} & c_2^3 \sum_i P'^3_{i2} A_{i2} \\ c_3 \sum_i P'_{i3} A_{i3} & c_3^2 \sum_i P'^2_{i3} A_{i3} & c_3^3 \sum_i P'^3_{i3} A_{i3} \end{bmatrix} \begin{Bmatrix} a_0 \\ a_1 \\ a_2 \end{Bmatrix} = \begin{Bmatrix} (F_T^{\exp})_1 \\ (F_T^{\exp})_2 \\ (F_T^{\exp})_3 \end{Bmatrix} \quad (4.5)$$

Substituting a_0, a_1 and a_2 obtained from Equation (4.5) into Equation (4.4), an optimum friction coefficient model expressed as a second order polynomial of pressure is determined.

4.4. Verification of New Method

The method has been tested by applying the method to back predict the input Stribeck friction model from force data obtained from the simulations for three pin diameter cases shown in the previous sections. The tension forces, and calculated bending forces and friction forces are summarized in Tables 4.1 and 4.2. Also, the ratios of total tension forces (fixed pin case/rotating pin case) were calculated and shown in Table 4.2.

Table 4.1 Tension forces from frictionless simulations

0.5" pin		1.0" pin		1.65" pin	
F_X'	F_Y'	F_X'	F_Y'	F_X'	F_Y'
756.2	917.8	756.2	822.1	756.2	788.7
F_B	161.6	F_B	65.9	F_B	32.5

Table 4.2 Tension forces from simulations with Stribeck friction

0.5" pin		1.0" pin		1.65" pin	
F_X	F_Y	F_X	F_Y	F_X	F_Y
756.2	1004.6	756.2	875.0	756.2	818.9
F_T	86.8	F_T	52.9	F_T	30.2
c^1	1.052	c^2	1.034	c^3	1.020

Following the new method using these data with the pressure maps (see Figures 4.2-4.4) obtained from frictionless simulations, a second order polynomial friction function was obtained as shown in Figure 4.10. The new method well predicted the input Stibeck friction curve in the range from 0 MPa to 40 MPa, but the predicted curve deviates from the input curve above the range. Two possible reasons of this deviation are:

1) Second order polynomial has limited ability to describe more general arctangent curve of Stribeck model.
2) Pressures over 40 MPa exist only at small areas of 12.7 mm diameter pin case as shown in Figures 4.2 and 4.11. Therefore the contribution to the total friction force is minor.

The friction coefficients of Figure 4.9 obtained by conventional method were also plotted in Figure 4.10 fitted with a second order polynomial curve. Values for the x axis are the average pressures calculated by Equation (2.2), so the conventional method can

only account for pressure in the average sense. The comparison shows that the conventional method overestimates the friction coefficients.

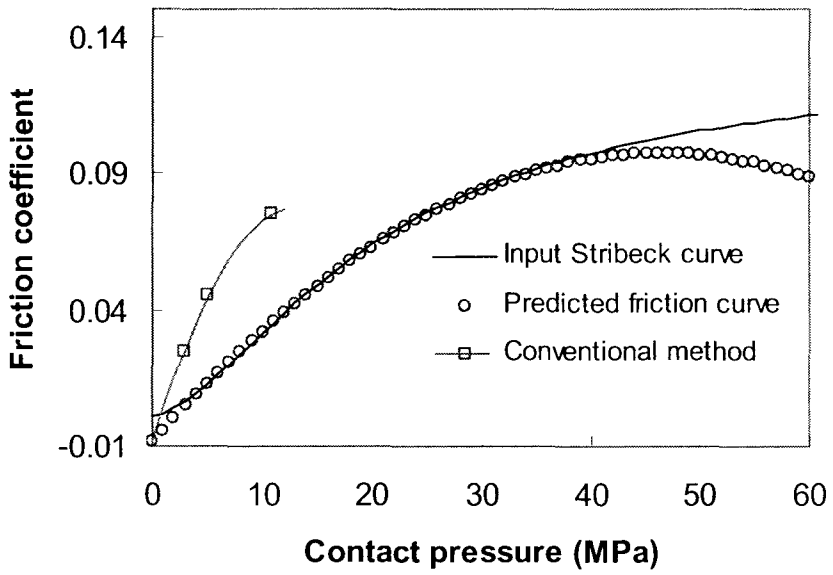

Figure 4.10 Predicted friction function compared to the input Stribeck curve.

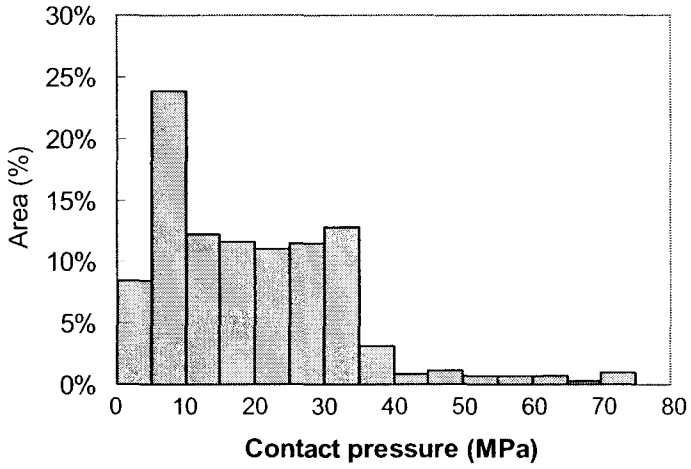

Figure 4.11 Areas corresponding to pressure ranges in 12.7 mm diameter pin case simulation.

4.5. Discussion

A new method to determine a friction coefficient as pressure dependent polynomial function has been developed. In the new method the pressure non-uniformity, which persists in draw-bend friction tests, is exploited to measure the pressure dependency of friction coefficient. The method is tested by applying the method to back predict the input Stribeck friction data from finite element simulation results of draw-bend friction tests. The method accurately determines the input friction curve over the pressure range that prevails in the draw-bend test conditions. In the next chapter, the new method will be applied to the real draw-bend friction tests for the friction measurement on aluminum sheets.

CHAPTER 5

NEW METHOD APPLIED TO FRICTION MEASUREMENT ON ALUMINUM SHEET

5.1. Introduction

In this chapter, the new pressure dependent method is applied to the friction measurements on aluminum sheets. Draw-bend friction tests have been performed on three different-size pins at three sliding speeds. The new method is applied to extract the friction coefficient as a function of contact pressure at each sliding speed. Then, the friction coefficient functions at three discrete speeds are interpolated over the domain of contact pressure and sliding speed. This produces a non-constant friction model as a continuous friction coefficient surface over domain of contact pressure and sliding speed. The function defining this surface can be effectively implemented into a finite element code.

5.2. Materials

Aluminum alloy AA5754-O is a candidate for automotive structural or body inner panels. The new method has been applied to the friction measurements of mill-finished

AA5754-O sheets. 'Mill-finished (MF)' means the natural appearance of aluminum sheets as they come from rolling mills without mechanical or chemical external finishing. MF aluminum sheets have strong directional anisotropy in surface roughness. Therefore, the friction measurements have been performed on strips oriented along the rolling direction (RD) and transverse direction (TD) of the sheets.

For this experimental work, AA5754-O sheets, cut at angles of 0° (RD) and 90° (TD) to the rolling direction with dimensions of 1.04 mm × 25.4 mm × 304.8 mm, have been provided by Novelis Global Technology Centre (NGTC). All of the tensile tests were performed at NGTC. The tensile parameters and true stress-true strain curves as received from NGTC are shown in Table 5.1 and Figure 5.1 respectively.

Table 5.1 Tensile properties of AA5754-O.

Thick (mm)	Direction	UTS (MPa)	0.2% YS (MPa)	Total Elong %	n-Value	r-Value ($\varepsilon = 0.1$)
1.05	RD	227.98	99.71	21.3	0.32	0.75
	TD	221.83	99.03	25.3	0.32	0.87

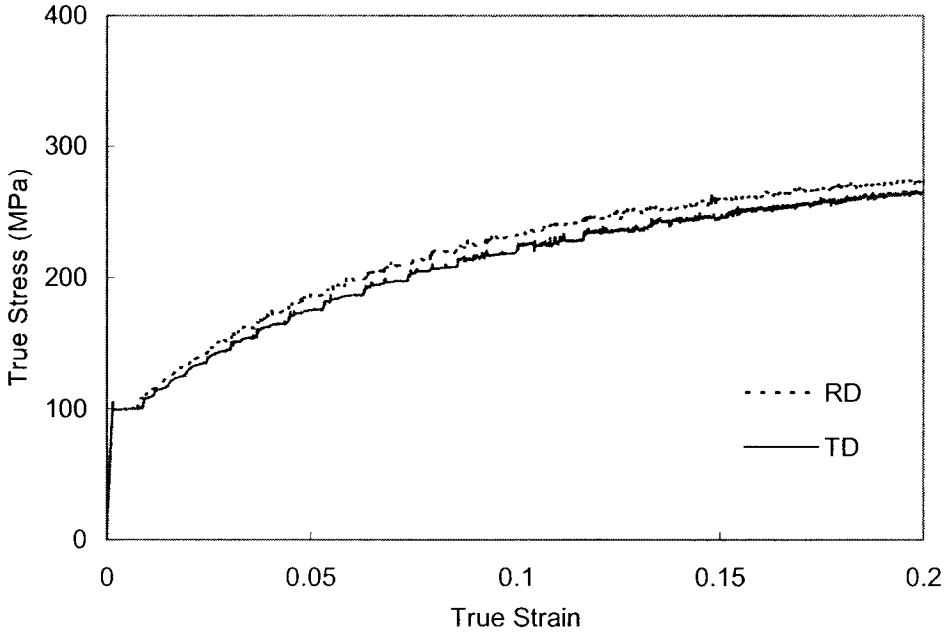

Figure 5.1 True stress-strain curves of AA5754-O for RD and TD.

5.3. Draw-Bend Friction Test Equipment

Figures 5.2 and 5.3 show the draw-bend friction test equipment in NGTC and the schematic of the test setup is shown in Figure 5.4. The setup consists of two mechanical grips which are connected to the two hydraulic actuators that are positioned perpendicular to one another. The movements of the grips are determined by a computer program that is used to control the motion of hydraulic actuators. The test procedure is as follows.

1) One end of a test strip is fastened to the inlet grip.
2) The other end of the strip is fastened to the outlet grip after the strip is bent around the pin by hand.

3) While the inlet grip is fixed, the outlet grip is moved until the outlet side tension load in the strip reaches about 1900 N.
4) Both grips are moved together as controlled by motion controller while the loads and displacements of both grips are recorded

To apply the new method for friction measurements, at least two pins of different sizes are required as demonstrated by numerical studies in the previous chapter. The NGTC had already two pins of 12.7 mm (0.5") and 25.4 mm (1.0") diameters. Therefore, the new method could produce a friction coefficient as a linear function of pressure p from the test results on these two pins. However, to obtain friction coefficients with more general forms (second order polynomial function of pressure) as explored in Chapter 4, a new pin of 42 mm diameter has been made according to the specifications for the existing pins as summarized in Table 5.2. The newly made pin with its supporting unit is shown in Figure 5.5 as well as existing pin units.

Table 5.2 Specification for existing pins.

Material	Surface Roughness (Ra)	Hardness (Rc)
H13 Tool Steel	0.1 μ m	56 ~ 58

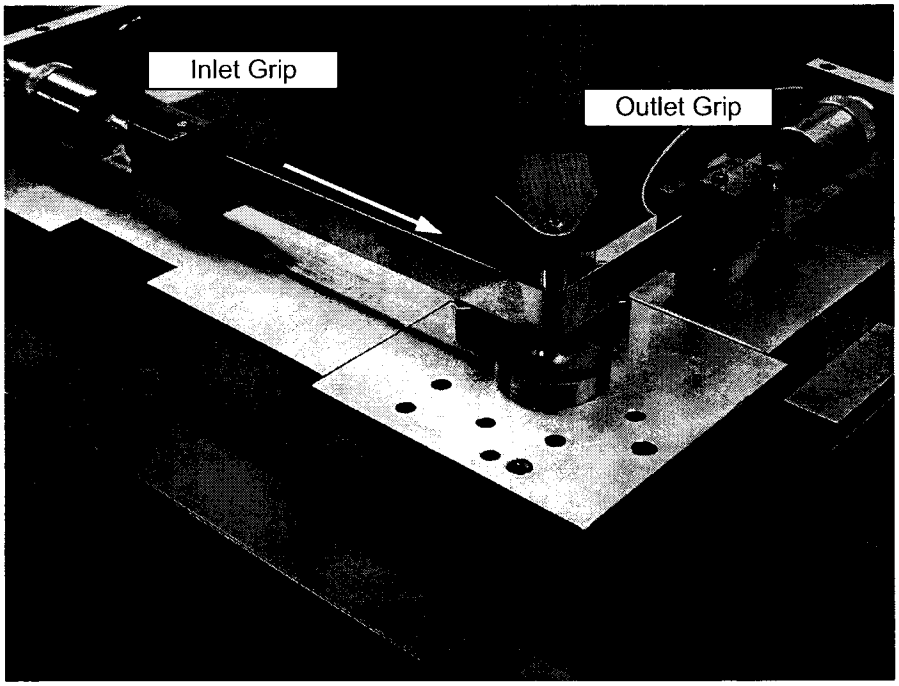

Figure 5.2 Draw-bend friction test setup (Novelis Global Technology Center).

Figure 5.3 Data acquisition system and motion controller (Novelis Global Technology Center).

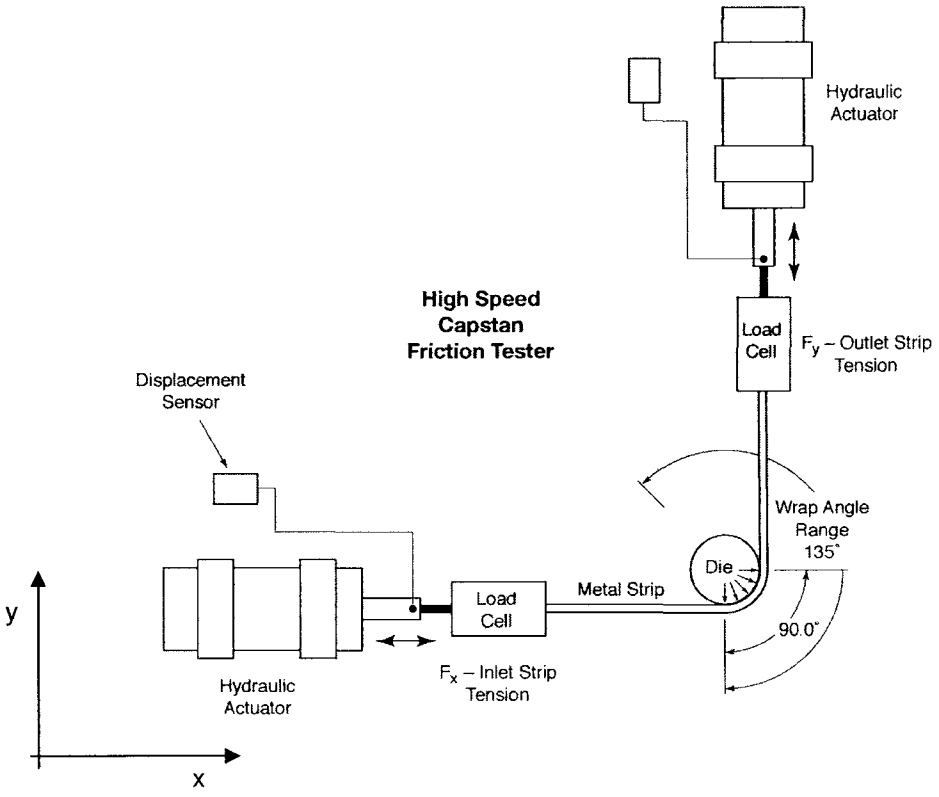

Figure 5.4 Schematic of draw-bend friction test setup (Novelis Global Technology Center).

In addition to the "fixed pins" that are fixed to a supporting structure, three "rotating pins" have been made incorporating ball bearings as shown in Figure 5.6. The rotating pins, as the name suggests, are free to rotate with minimal resistance and used for the bending force measurements. The diameters of the rotating pins are the same as those of fixed pins (12.7 mm, 25.4 mm and 42 mm). The rotating pins were made with mild steels without surface preparation because sliding will not occur at the interface. The design drawings for newly made pin units are attached in Appendix A.

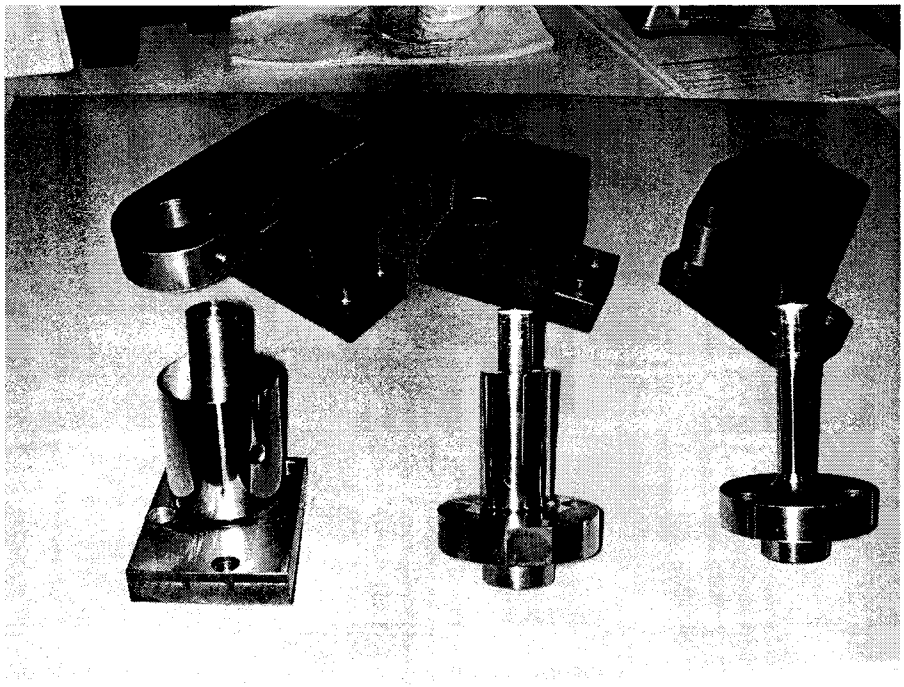

Figure 5.5 Fixed pin units: 42 mm, 25.4 mm, 12.7 mm diameters (from left).

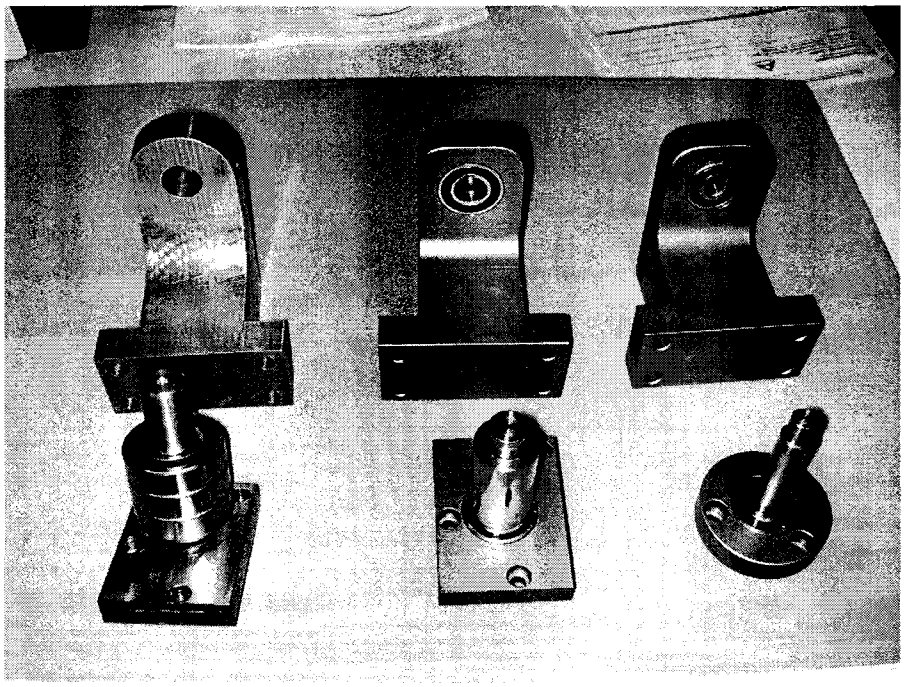

Figure 5.6 Freely rotating pin units for bending force measurements.

5.4. Rotating-Pin Tests for Bending Force Measurements

For each test condition on a fixed pin, a test has to be performed on a rotating pin of the same size to measure the bending force. The measured bending forces are subtracted from the fixed pin results to obtain pure friction forces. Thus, a series of draw-bend tests have been performed first on the rotating pins of three different sizes.

Figures 5.7, 5.8, and 5.9 show the force data from strips tested along RD at a speed of 25.4 mm/s on 12.7 mm, 25.4 mm and 42 mm diameter pins. The difference between the inlet and outlet forces is the bending force, because the rotating pins do not exert frictional forces. The fluctuations shown in the data are not electrical noises. They are fluctuations in real loads, which is due to the motions of hydraulic actuators that are not perfectly uniform (constant). This becomes clear when we plot the data in a form as shown in Figure 5.10, where horizontal axis is for the inlet force (back tension force) and vertical axis is for the outlet and bending forces.

To study the directional effect of bending forces, tests have been performed also with a TD strip on the 12.7 mm diameter pin. Figure 5.11 shows the comparison between the data from RD and TD strips and shows that the directional effect of bending force itself is minor. Therefore, bending force data obtained from tests with RD strips will be used in the later analyses of friction for both RD and TD strips.

Figures 5.12, 5.13, and 5.14 show the measured bending forces from rotating pin tests with RD strips, and their linear-fit curves are summarized in Table 5.3. Tests have been performed twice on each pin under the same conditions and the data from both tests

have been used for the linear-fits. The test shows a good repeatability. We can see from the results that the bending forces are inversely proportional to applied back tension forces and pin diameters (Figure 5.15). The gap in the data shown in Figure 5.14 results from two tests that were performed in the different ranges of back tension force.

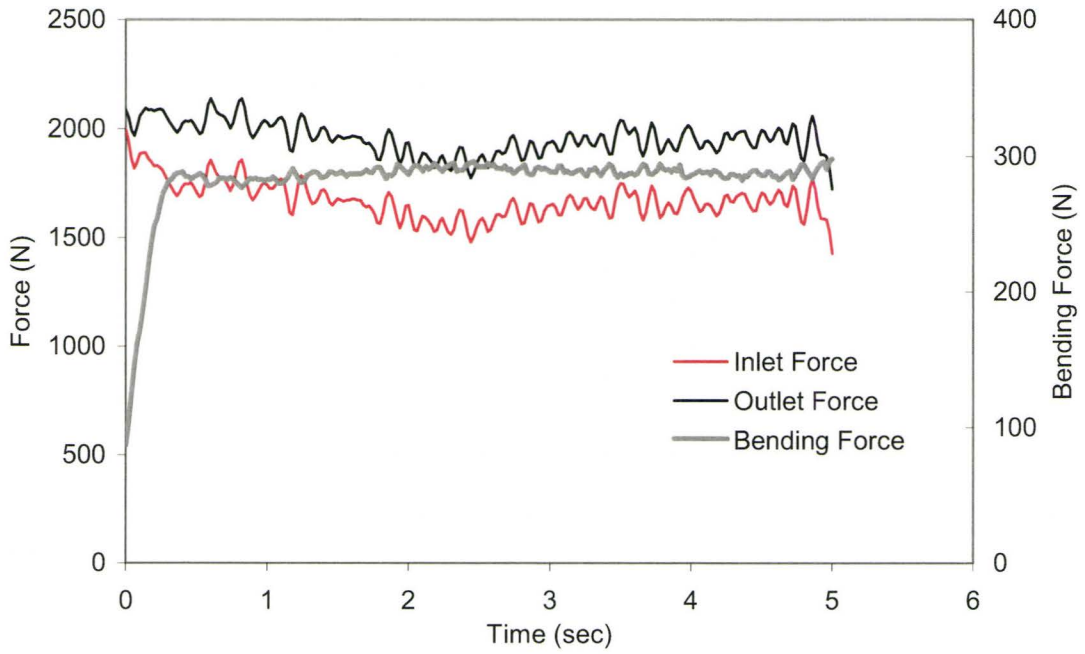

Figure 5.7 Force data from test with 12.7 mm diameter rotating pin (RD strip).

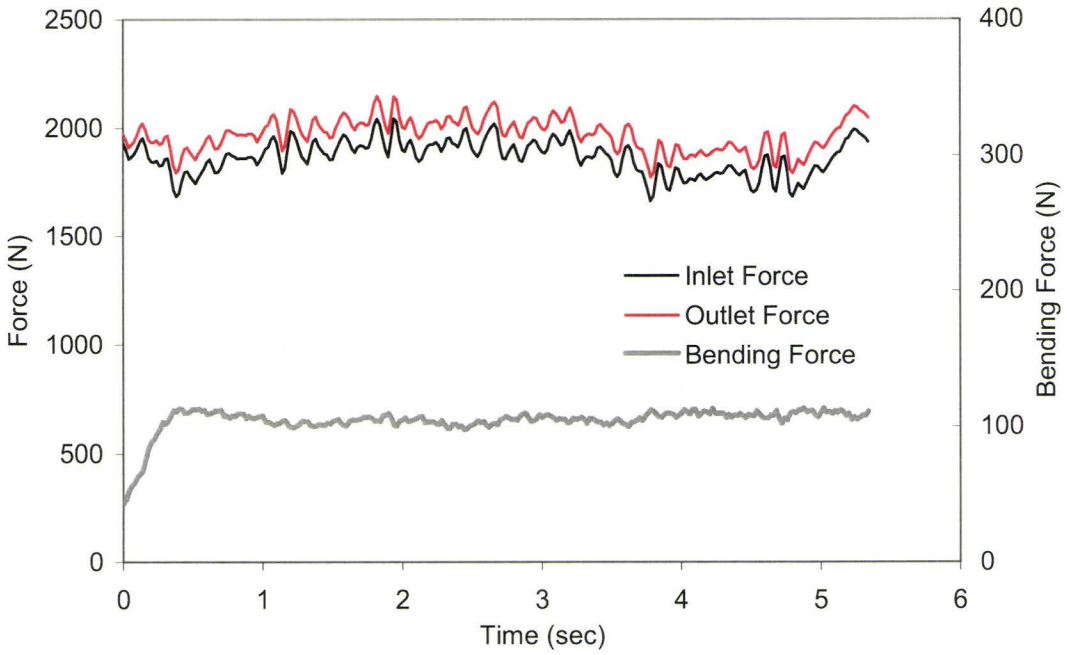

Figure 5.8 Force data from test with 25.4 mm diameter rotating pin (RD strip).

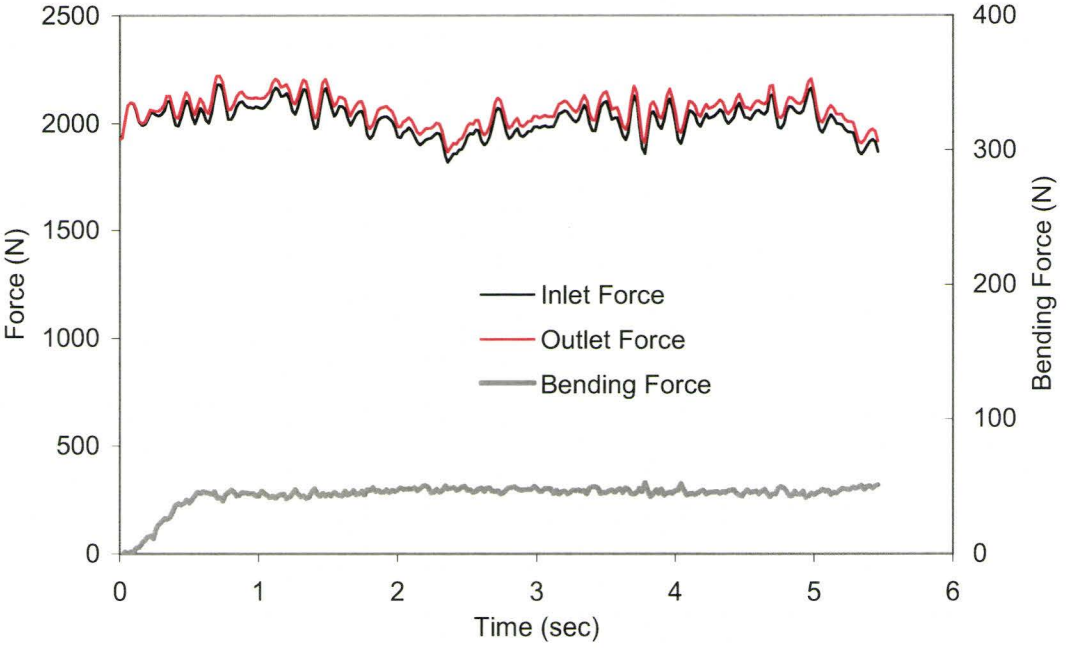

Figure 5.9 Force data from test with 42 mm diameter rotating pin (RD strip).

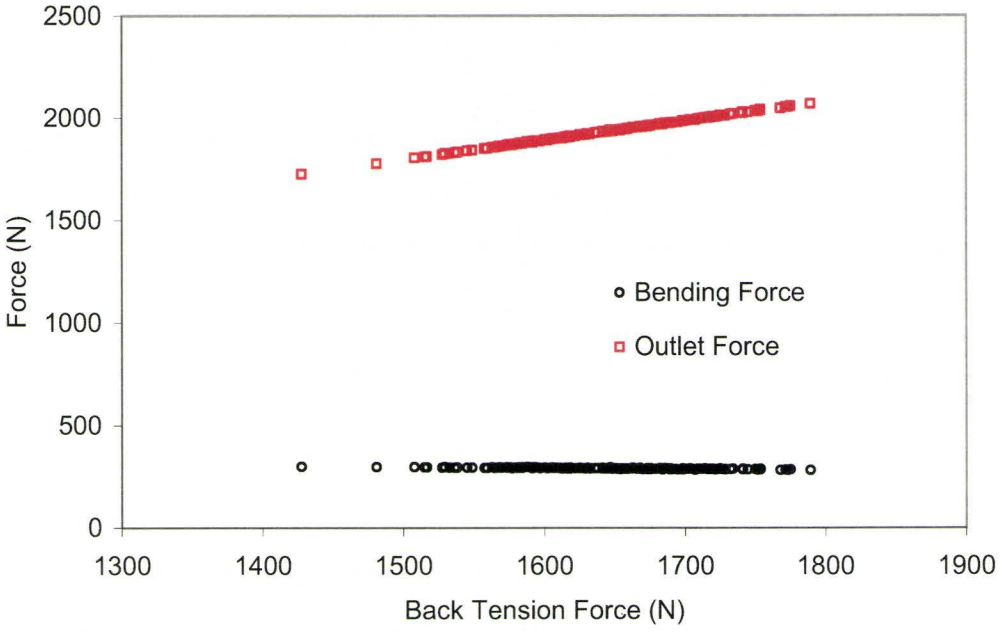

Figure 5.10 Force data from test on 12.7 mm diameter rotating pin with RD strip.

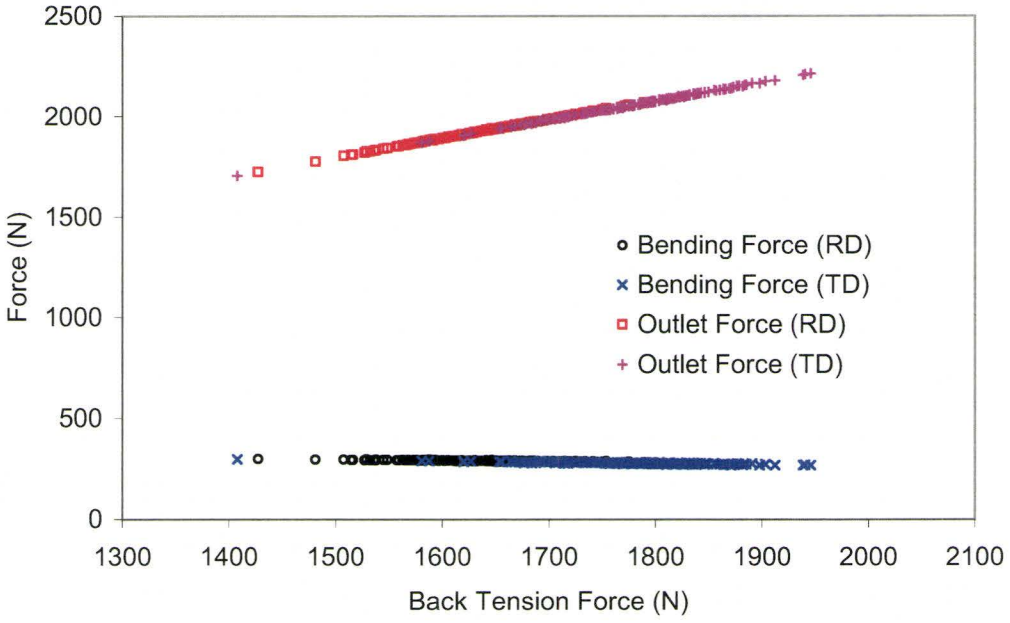

Figure 5.11 Bending force comparison for directional effect with 12.7 mm diameter pin.

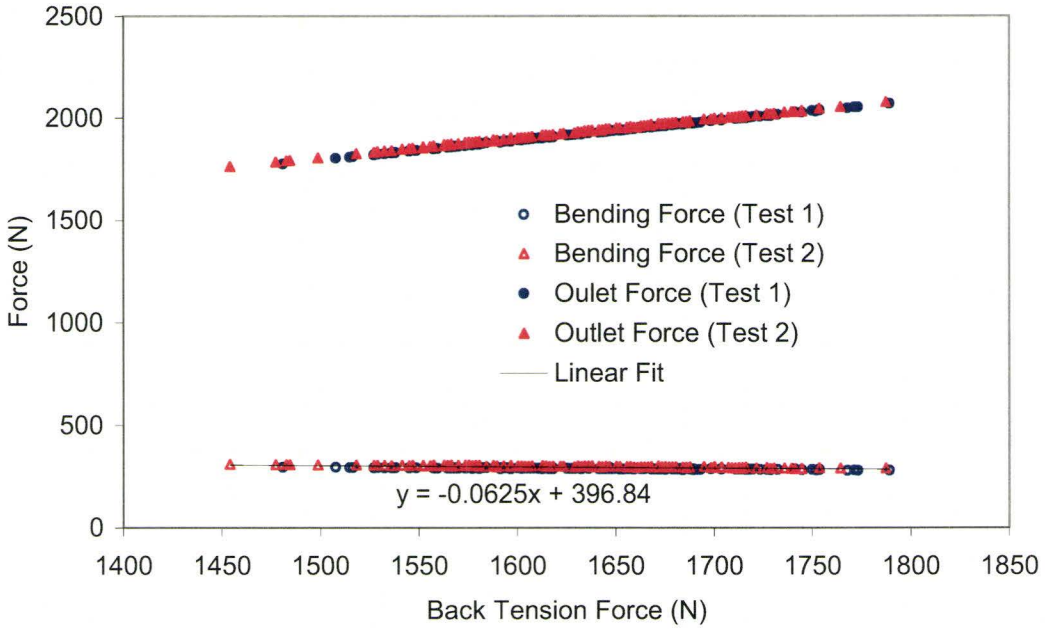

Figure 5.12 Bending force from 12.7 mm diameter pin tests.

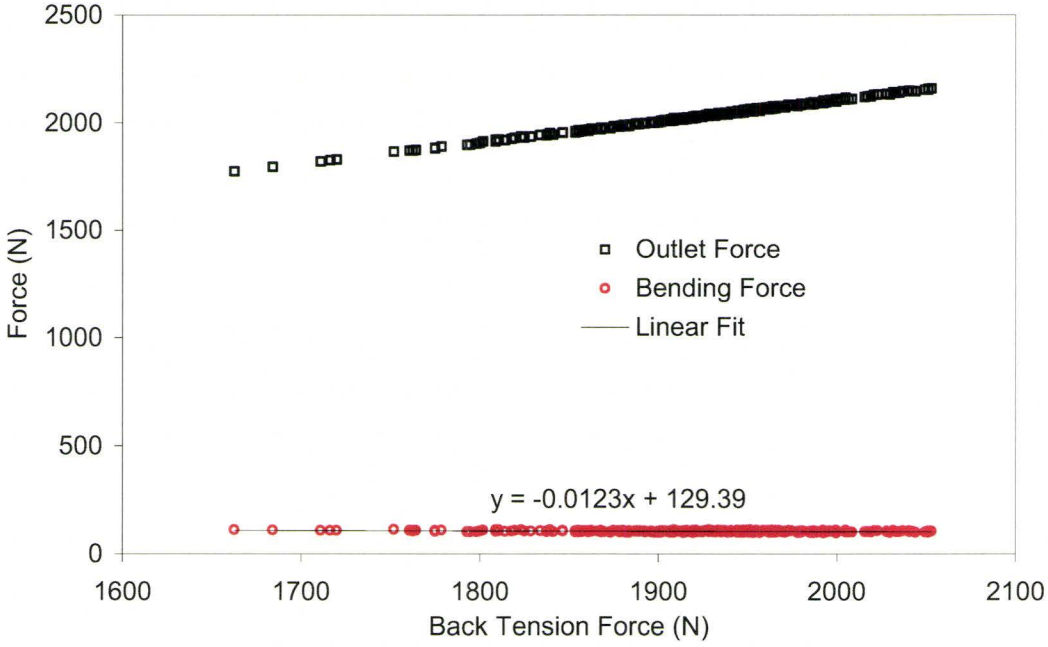

Figure 5.13 Bending force from 25.4 mm diameter pin tests.

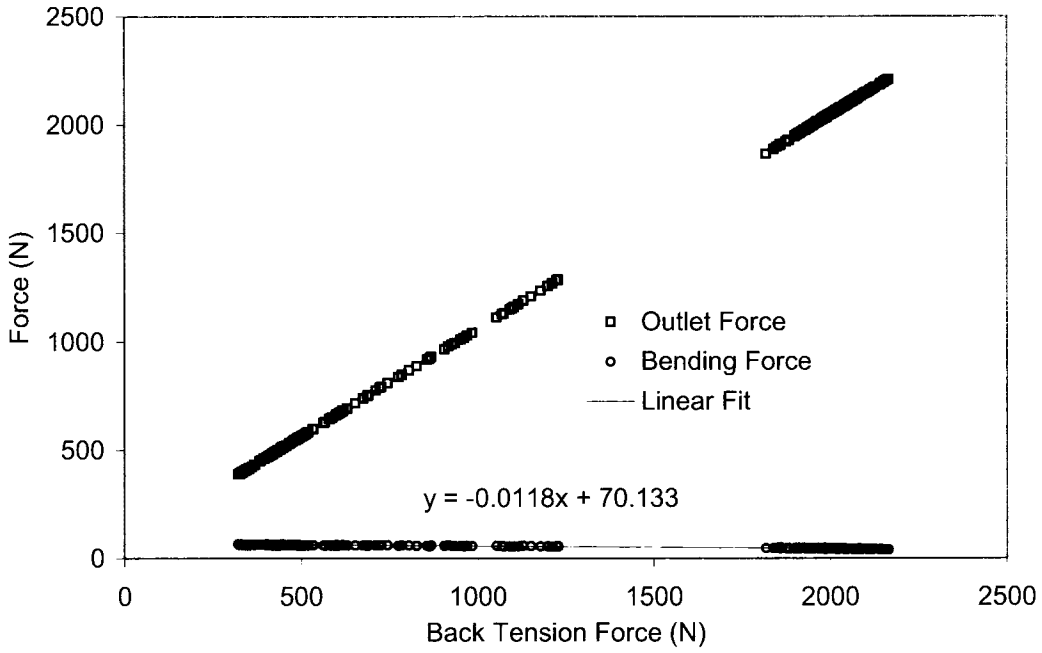

Figure 5.14 Bending force with 42 mm diameter pin (RD).

Table 5.3 Linear-fit curves for obtained bending force.

Pin Dia.	Applied Back-Tension Force Range F_{back}	Linear-fit for Bending Force (N)
12.7 mm	1,450 N ~ 1,800 N	$F_{bend} = -0.0625 \times F_{back} + 396.84$
25.4 mm	1,650 N ~ 2,050 N	$F_{bend} = -0.0123 \times F_{back} + 129.39$
42 mm	400 N ~ 2,100 N	$F_{bend} = -0.0118 \times F_{back} + 70.133$

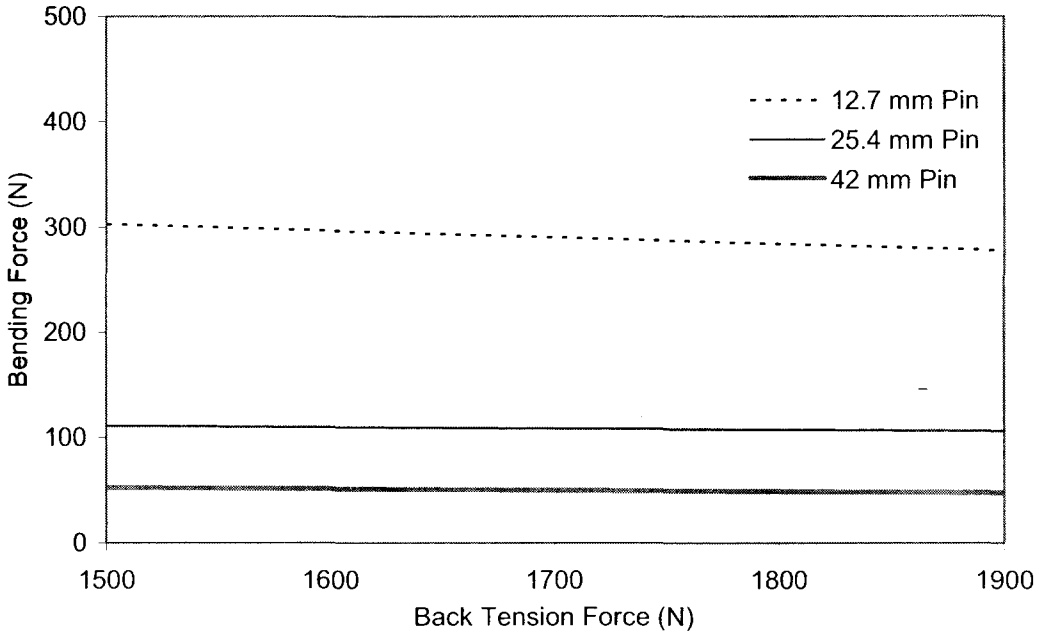

Figure 5.15 Bending forces depending on pin diameter.

5.5. Fixed-Pin Tests and Pure Friction Force Measurements

The draw-bend tests have been performed on the fixed pins with RD and TD strips. The test methods were the same as the rotating-pin tests and Table 5.4 shows the overall test matrix for fixed-pin tests. Parker MP404 lubricant was applied to the test strips by

dipping the specimens into lubricant solution diluted with Hexanes. By this way, 1.7 - 2.3 g/m^2 of lubrications were applied to the strips. Figures 5.16, 5.17 and 5.18 show the typical data of fixed-pin tests, which are from the tests at a sliding speed of 25.4 mm/s with RD strips. As in the rolling-pin tests, duplicate tests have been performed for each of the test conditions.

Table 5.4 Fxed-pin test matrix.

Direction	Speed (mm/s)	Pin Dia. (mm)	Direction	Speed (mm/s)	Pin Dia. (mm)
RD	6.35	12.7	TD	6.35	12.7
RD	6.35	25.4	TD	6.35	25.4
RD	6.35	42	TD	6.35	42
RD	25.4	12.7	TD	25.4	12.7
RD	25.4	25.4	TD	25.4	25.4
RD	25.4	42	TD	25.4	42
RD	101.6	12.7	TD	101.6	12.7
RD	101.6	25.4	TD	101.6	25.4
RD	101.6	42	TD	101.6	42

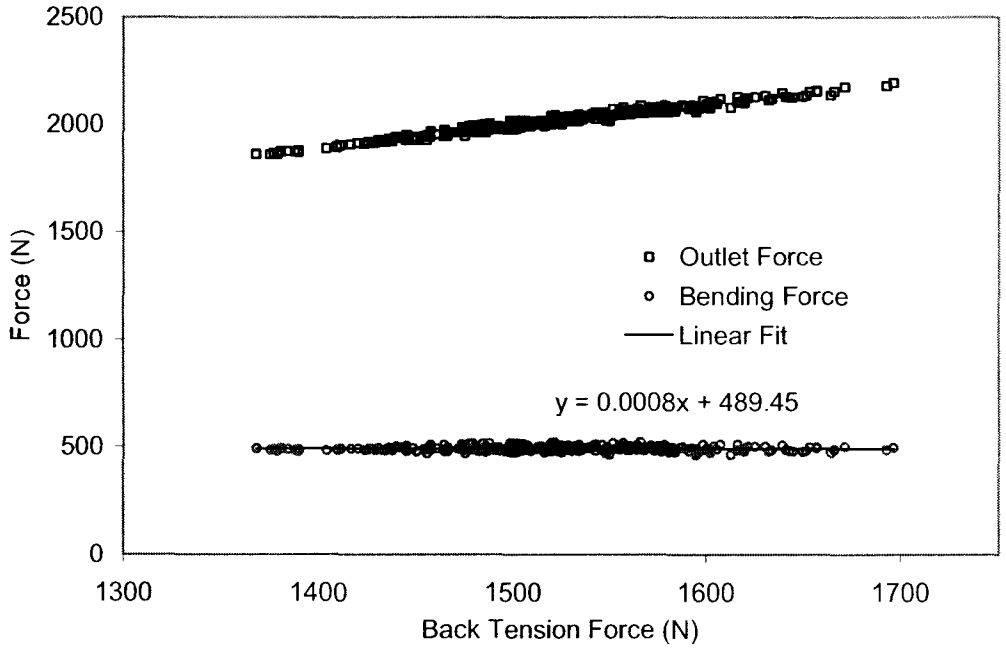

Figure 5.16 Force data from 12.7 mm diameter pin test (RD, v=25.4 mm/s).

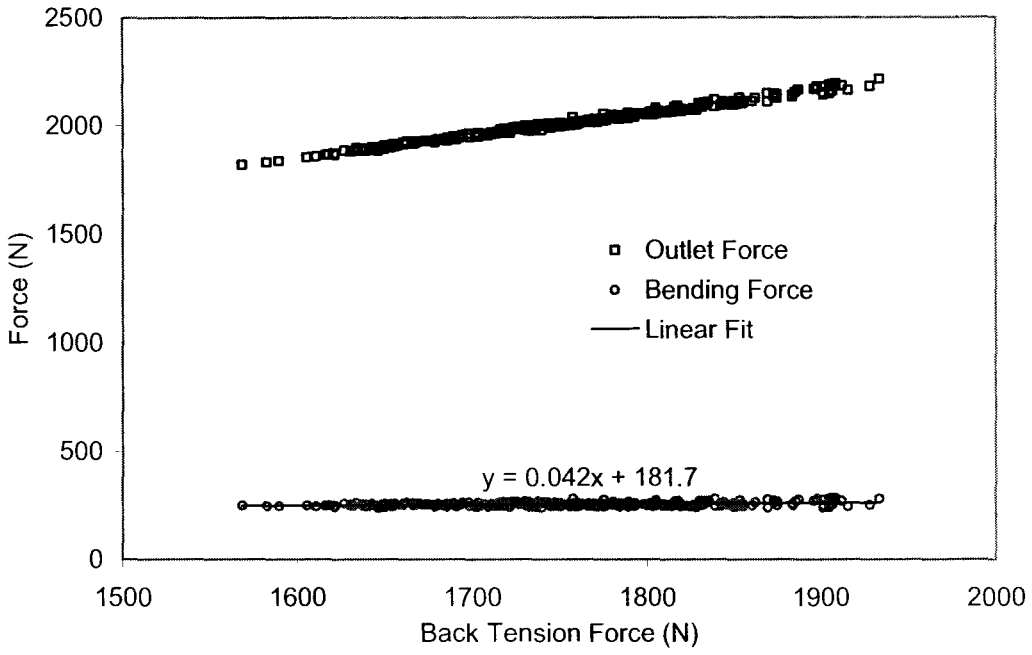

Figure 5.17 Force data from 25.4 mm diameter pin test (RD, v=25.4 mm/s).

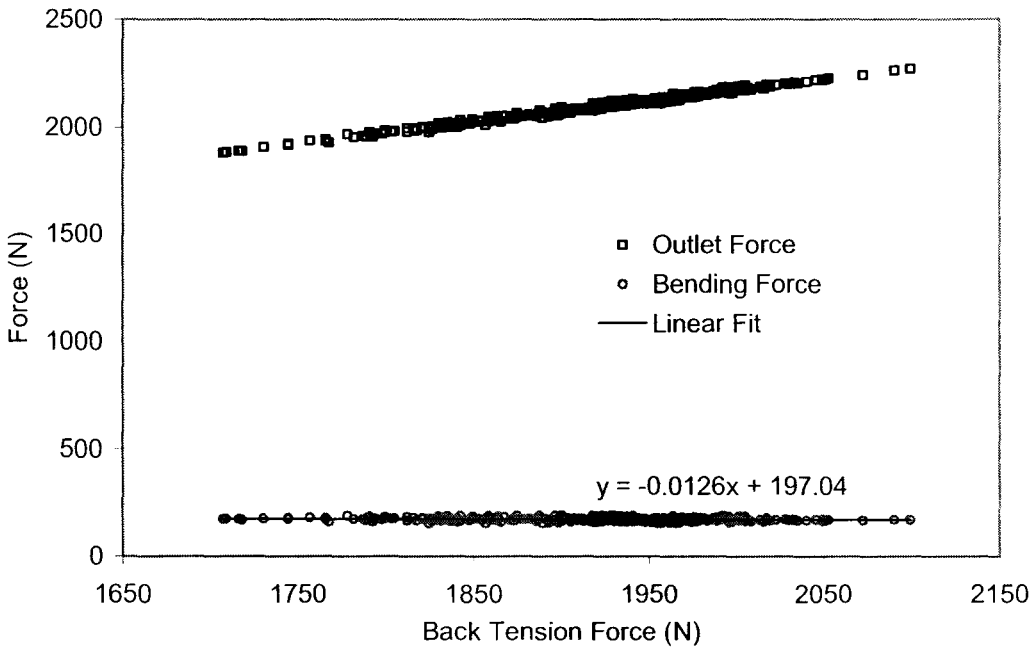

Figure 5.18 Force data from 42 mm diameter pin test (RD, v=25.4 mm/s).

The difference between the outlet and back-tension forces from fixed-pin tests comes from two sources, friction and bending forces. The linear-fit data for these friction plus bending forces are summarized in Tables 5.5 to 5.10.

Table 5.5 Friction+Bending Forces with RD Strips at v=6.35 mm/s.

Pin Dia. (mm)	Applied Back-Tension Force Range, F_{back}	Linear-fit for Friction+Bending Forces (N)
12.7	1,400 N ~ 1,700 N	$F_{fric+bend} = 0.0285 \times F_{back} + 503.6$
25.4	1,700 N ~ 2,000 N	$F_{fric+bend} = 0.0048 \times F_{back} + 258.42$
42	1,500 N ~ 2,100 N	$F_{fric+bend} = 0.0309 \times F_{back} + 188.78$

Table 5.6 Friction+Bending Forces with RD Strips at v=25.4 mm/s.

Pin Dia. (mm)	Applied Back-Tension Force Range, F_{back}	Linear-fit for Friction+Bending Forces (N)
12.7	1,400 N ~ 1,700 N	$F_{fric+bend} = 0.0008 \times F_{back} + 489.45$
25.4	1,600 N ~ 1,900 N	$F_{fric+bend} = 0.042 \times F_{back} + 181.7$
42	1,700 N ~ 2,100 N	$F_{fric+bend} = -0.0126 \times F_{back} + 197.04$

Table 5.7 Friction+Bending Forces with RD Strips at v=101.6 mm/s.

Pin Dia. (mm)	Applied Back-Tension Force Range, F_{back}	Linear-fit for Friction+Bending Forces (N)
12.7	1,450 N ~ 1,670 N	$F_{fric+bend} = -0.0062 \times F_{back} + 394.54$
25.4	1,850 N ~ 1,960 N	$F_{fric+bend} = -0.0447 \times F_{back} + 252.41$
42	1,750 N ~ 2,050 N	$F_{fric+bend} = -0.106 \times F_{back} + 388.58$

Table 5.8 Friction+Bending Forces with TD Strips at v=6.35 mm/s.

Pin Dia. (mm)	Applied Back-Tension Force Range, F_{back}	Linear-fit for Friction+Bending Forces (N)
12.7	1,450 N ~ 1,700 N	$F_{fric+bend} = 0.0037 \times F_{back} + 430.88$
25.4	1,750 N ~ 2,000 N	$F_{fric+bend} = -0.0016 \times F_{back} + 233.84$
42	1,500 N ~ 1,800 N	$F_{fric+bend} = 0.0433 \times F_{back} + 128.09$

Table 5.9 Friction+Bending Forces with TD Strips at v=25.4 mm/s.

Pin Dia. (mm)	Applied Back-Tension Force Range, F_{back}	Linear-fit for Friction+Bending Forces (N)
12.7	1,350 N ~ 1,650 N	$F_{fric+bend} = 0.0154 \times F_{back} + 385.85$
25.4	1,600 N ~ 1,870 N	$F_{fric+bend} = 0.0339 \times F_{back} + 149.64$
42	1,650 N ~ 2,100 N	$F_{fric+bend} = 0.0403 \times F_{back} + 123.04$

Table 5.10 Friction+Bending Forces with TD Strips at v=101.6 mm/s.

Pin Dia. (mm)	Applied Back-Tension Force Range, F_{back}	Linear-fit for Friction+Bending Forces (N)
12.7	1,400 N ~ 1,600 N	$F_{fric+bend} = -0.0539 \times F_{back} + 466.01$
25.4	1,600 N ~ 1,900 N	$F_{fric+bend} = -0.0212 \times F_{back} + 233.1$
42	1,700 N ~ 2,000 N	$F_{fric+bend} = -0.0917 \times F_{back} + 374.76$

On subtracting the bending forces in Table 5.3 from the friction plus bending forces, pure friction forces are obtained as summarized in Tables 5.11 and 5.12.

Table 5.11 Friction Forces with RD Strips.

Pin Dia. (mm)	Linear-fit for Pure Friction Force (N), F_{fric} =		
	at v=6.35 mm/s	at v=25.4 mm/s	at v=101.6 mm/s
12.7	$0.091 \times F_{back} + 106.76$	$0.0633 \times F_{back} + 92.61$	$0.0563 \times F_{back} - 2.3$
25.4	$0.0171 \times F_{back} + 129.03$	$0.0543 \times F_{back} + 52.31$	$-0.0324 \times F_{back} + 123.02$
42	$0.0427 \times F_{back} + 118.65$	$-0.0008 \times F_{back} + 123.91$	$-0.0942 \times F_{back} + 318.45$

Table 5.12 Friction Forces with TD Strips.

Pin Dia. (mm)	Linear-fit for Pure Friction Force (N), F_{fric} =		
	at v=6.35 mm/s	at v=25.4 mm/s	at v=101.6 mm/s
12.7	$0.0662 \times F_{back} + 34.04$	$0.0779 \times F_{back} - 10.99$	$0.0086 \times F_{back} + 69.17$
25.4	$0.0107 \times F_{back} + 104.45$	$0.0462 \times F_{back} + 20.25$	$-0.0089 \times F_{back} + 103.71$
42	$0.0551 \times F_{back} + 57.96$	$0.0521 \times F_{back} + 52.91$	$-0.0799 \times F_{back} + 304.63$

5.6. Friction Coefficient Estimation by Conventional Method

In the conventional method, it is assumed that the pressure distribution at a pin/strip interface is uniform and that the extent of contact is equal to the wrap angle (90° in this study). Based on these assumptions, a contact pressure is calculated from the inlet and outlet forces and the friction force per unit area is obtained by dividing the measured friction force by the contact area. This conventional method gives an Equation (2.3) introduced in Chapter 2. Equation (2.3) can be rewritten as Equation (5.1) to apply the pure friction force data from Tables 5.11 and 5.12 directly.

$$\mu = \frac{2}{\pi} \ln \frac{(F_{fric} + F_{back})}{F_{back}} \tag{5.1}$$

where F_{fric} and F_{fric} are pure friction and back tension forces respectively.

Figures 5.19 and 5.20 show the friction coefficients estimated by Equation (5.1), in that the pure friction force data at the back-tension force of F_{back}=1,700 N have been applied. Except for the case with the 42 mm diameter pin, the obtained friction coefficients show the same trend observed by others (Zheng and Overby, 1988; Kotchman et al., 1992; Saha et al., 1996; Han, 1997; Keum et al., 2004; Deng and Lovell, 2000) that the friction coefficient decreases as the pin diameter increases.

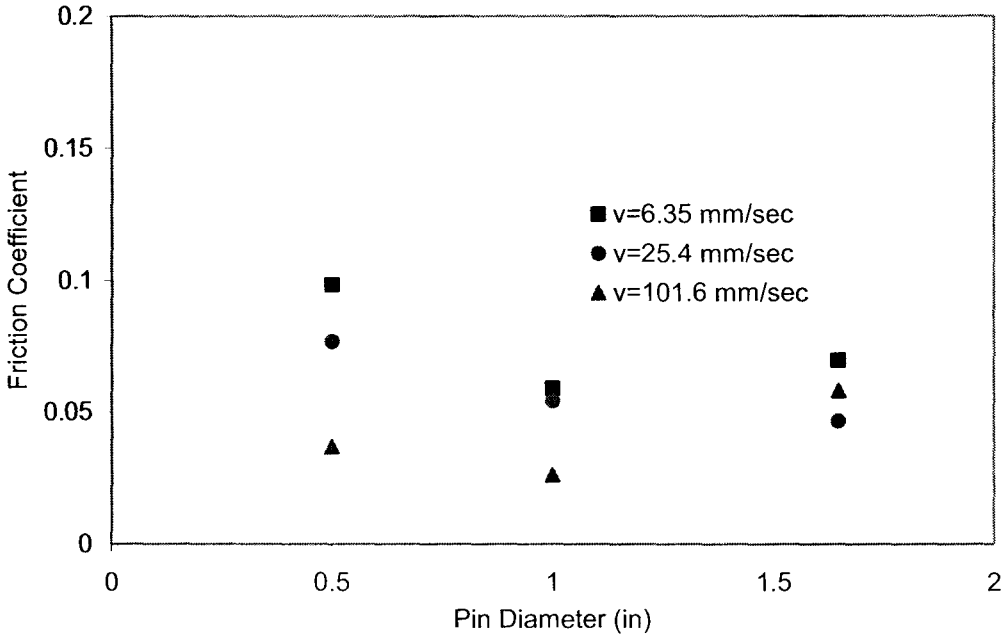

Figure 5.19 Friction coefficients of RD strips by conventional method.

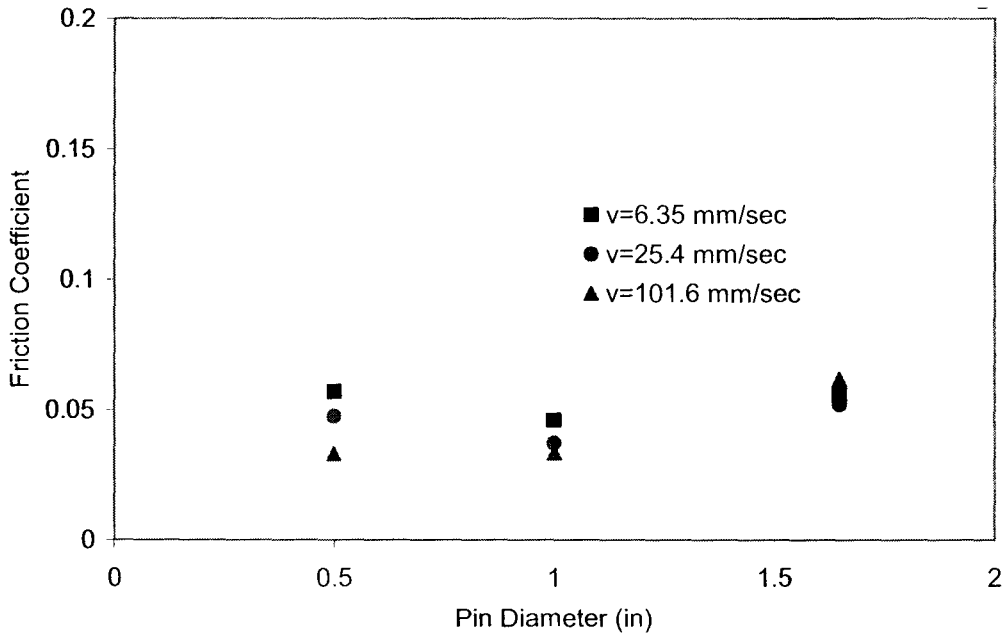

Figure 5.20 Friction coefficients of TD strips by conventional method.

To investigate the cause of odd data from 42 mm diameter pin, the surfaces of the 42 mm diameter pin and 25.4 mm diameter pin have been looked into by an optical microscope (ZYGO optical profiler). It was found that the surface profile of newly made 42 mm diameter pin is quite different from the existing pins as shown in Figure 5.21. Therefore, in the next section the new friction measurement method will be applied to the test results from the 12.7 mm and 25.4 mm diameter pins only not including the 42 mm diameter pin. This will make the new method to estimate the friction coefficients as linear functions of pressure. In Section 5.8, the same tests are repeated with the three pins in an undiluted (or rich) lubricant condition to reduce the effect of surface roughness on friction. Then, the new method is applied to the test results including the 42 mm diameter pin case to demonstrate the capability of new method to estimate friction coefficient functions in a more general form of a second-order polynomial.

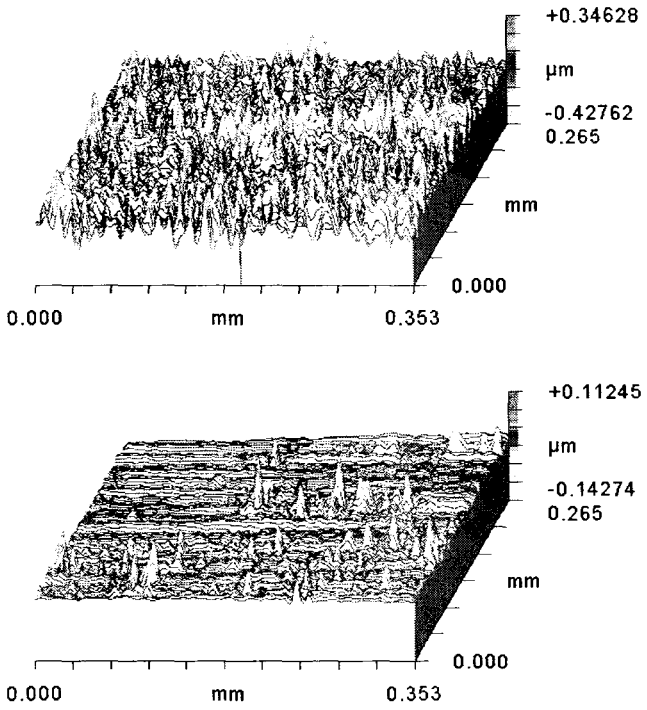

Figure 5.21 Surface profiles : existing 25.4 mm diameter pin (top), newly made 42 mm diameter pin (bottom).

5.7. Friction Coefficient Measurement by New Method

5.7.1. Contact Pressure Maps

In the new method, contact pressure maps, which are obtained from finite element simulations, are used to measure the pressure dependency of friction coefficient. The details of how to obtain pressure maps from simulations and the methodology for the estimation of friction coefficient have been explained in Chapter 4.

To obtain the pressure maps at the current test conditions, simulations similar to the ones in Chapter 4 have been performed for the three pin cases. The finite element models for the simulations are shown in Figure 5.22. To increase the pressure collection points toward the strip edges where the pressure changes are higher than the center, meshes were refined near the strip edges. The stress-strain data from a RD strip, shown earlier in Figure 5.1 has been used as input for a multi-linear plasticity model. The back-tension force was selected for each pin case from the ranges of the values applied both in rotating-pin and fixed-pin tests (see Tables 5.3 through 5.11). Table 5.12 shows the selected back-tension forces and half the amounts of forces were applied to the simulations due to the symmetry conditions.

The contact pressure data at the nodes of pin/strip interfaces and the area data associated with the nodes were obtained from the simulations. The acquired contact pressure maps (pressure and area data) from the simulations are plotted in Figures 5.23, 5.24, and 5.25.

Table 5.13 Back-Tension Forces Selected for Simulations

12.7 mm Pin	25.4 mm Pin	42 mm Pin
1,500 N	1,800 N	1,900 N

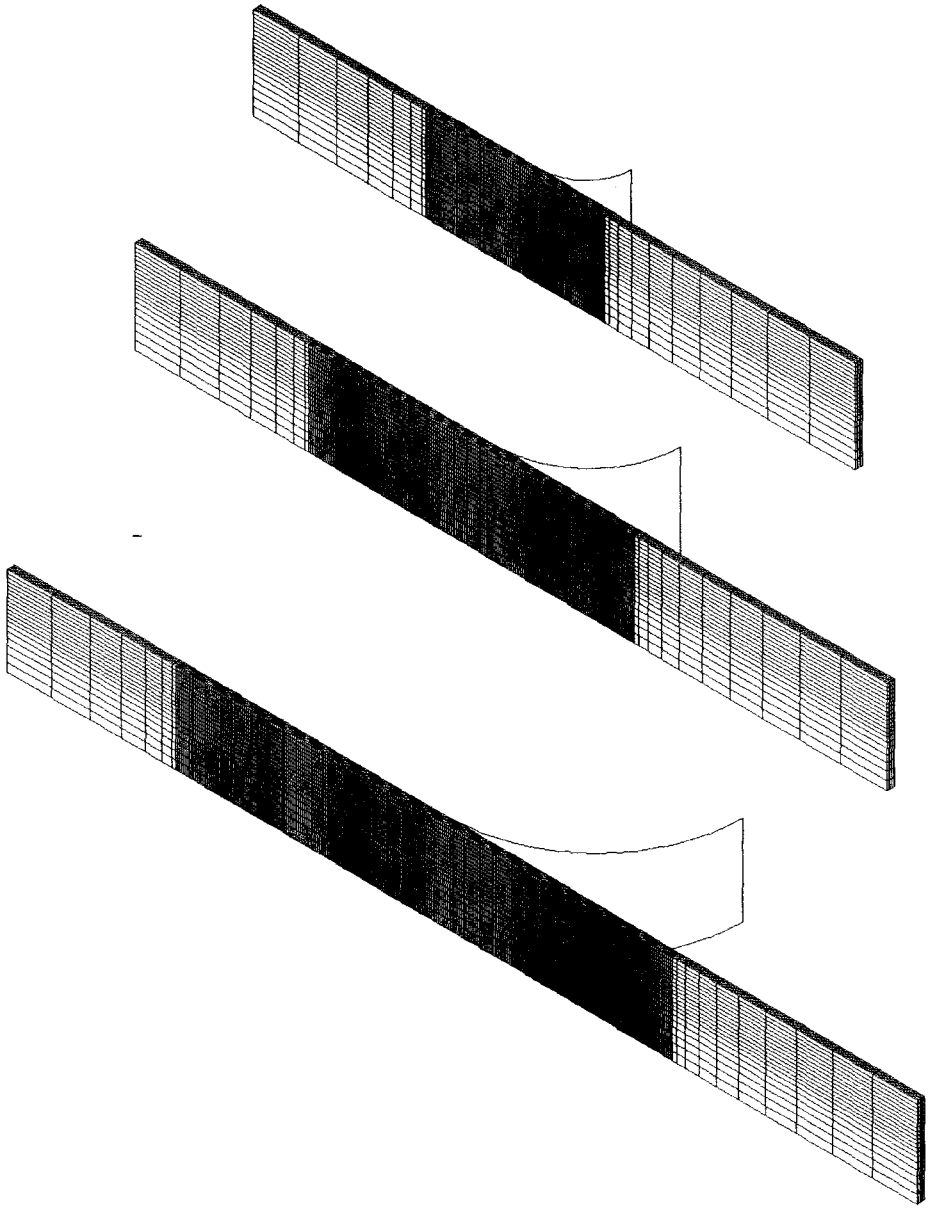

Figure 5.22 Finite element modes for draw-bend tests with 12.7 mm (top), 25.4 mm (middle), and 42 mm diameter (bottom) pins.

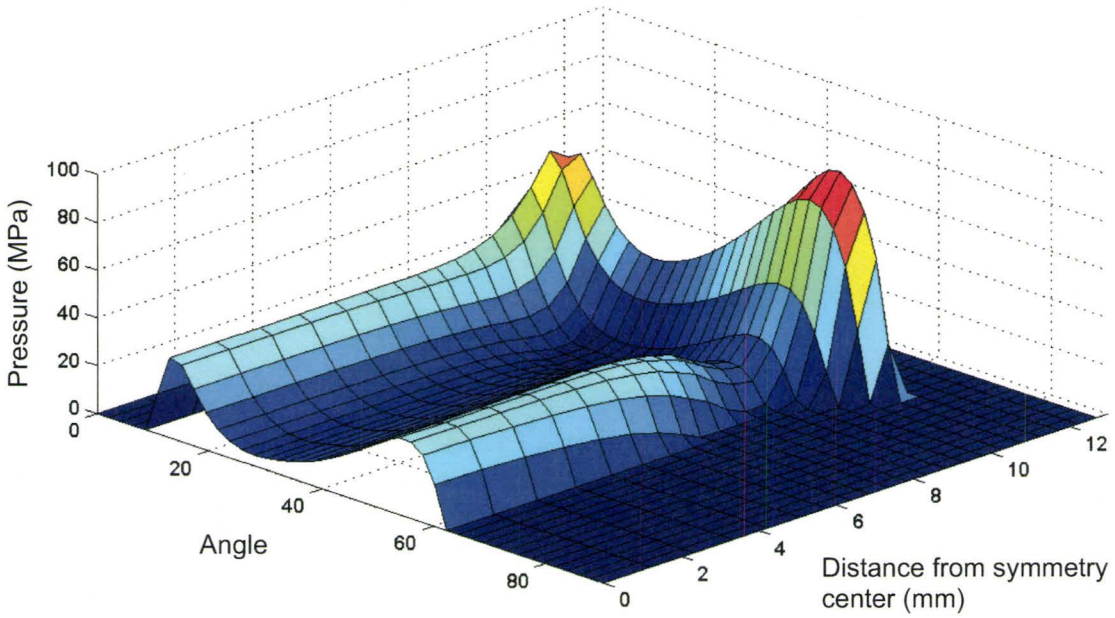

Figure 5.23 Pressure map obtained from 12.7 mm diameter pin simulation.

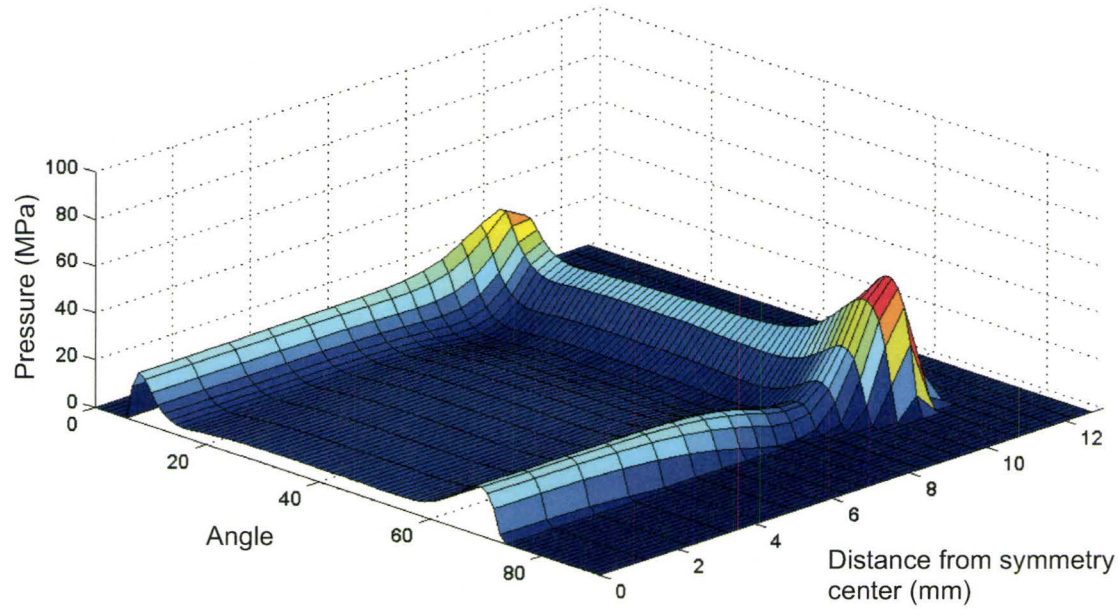

Figure 5.24 Pressure map obtained from 25.4 mm diameter pin simulation.

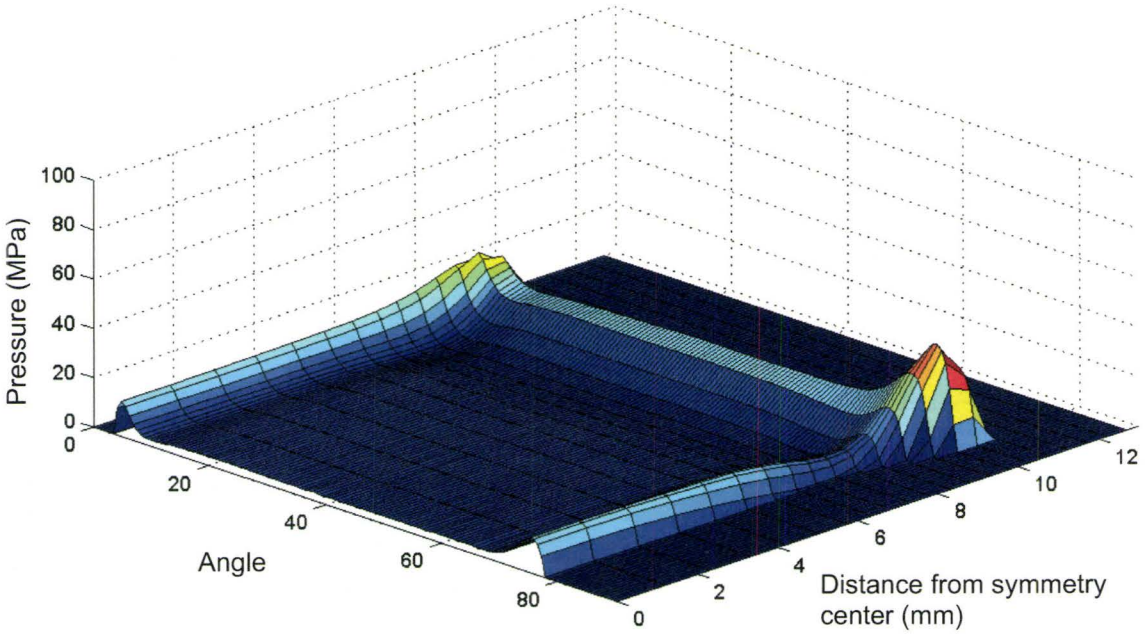

Figure 5.25 pressure map obtained from 42 mm diameter pin simulation (MPa).

5.7.2. Application of the New Method

To apply the new method, the measured friction forces were taken from the linear-fit equations in Tables 5.11 and 5.12 at the back-tension force levels that were chosen in Table 5.13. The resulting friction forces are summarized in Table 5.14. Test results with the 42 mm diameter pin were omitted due to the uncertainties explained previously. The average contact pressure ratios c_j between fixed-pin tests and rotating-pin tests have been calculated by comparing the average pressures using the formula in Equation (2.2) as shown in Table 5.15.

Table 5.14 Friction Forces with Diluted Lubricant.

Speed	RD		TD	
	12.7 mm Pin $(F_{fric})_1$	25.4 mm Pin $(F_{fric})_2$	12.7 mm Pin $(F_{fric})_1$	25.4 mm Pin $(F_{fric})_2$
6.35 mm/s	243.26 N	159.81 N	133.34 N	123.71 N
25.4 mm/s	187.56 N	150.05 N	105.86 N	103.41 N
101.6 mm/s	82.15 N	64.70 N	82.07 N	87.69 N

Table 5.15 Average Pressure Ratio (Fixed-Pin Test / Rotating-Pin Test).

Speed	RD		TD	
	12.7 mm Pin c_1	25.4 mm Pin c_2	12.7 mm Pin c_1	25.4 mm Pin c_2
6.35 mm/s	1.064	1.039	1.031	1.029
25.4 mm/s	1.047	1.036	1.023	1.024
101.6 mm/s	1.016	1.013	1.016	1.020

With test results from two pins only, the friction coefficient can be estimated as a linear function in Equation (5.2) instead of a second order polynomial function in Equation (4.4). Consequently, the matrix equation relating pressure, area and force components reduces to Equation (5.3), where p_{i1} and p_{i2} are pressure data from simulations for 12.7 mm diameter pin and 25.4 mm diameter pin cases respectively, A_{i1} and A_{i2} are mesh area data, and c_1 and c_2 are ratios in average pressures. Applying these pressure maps, measured friction forces, and average contact pressure ratios to Equation (5.3), the friction coefficient function is obtained at each sliding speed for RD and TD strips as shown in Table 5.16 and Figures 5.26 and 5.27.

$$\mu(p) = a_0 + a_1 p \tag{5.2}$$

$$\begin{bmatrix} c_1 \sum_i p_{i1} A_{i1} & c_1^2 \sum_i p_{i1}^2 A_{i1} \\ c_2 \sum_i p_{i2} A_{i2} & c_2^2 \sum_i p_{i2}^2 A_{i2} \end{bmatrix} \begin{Bmatrix} a_0 \\ a_1 \end{Bmatrix} = \begin{Bmatrix} (F_{fric})_1 \\ (F_{fric})_2 \end{Bmatrix} \tag{5.3}$$

Table 5.16 Obtained Friction Coefficient Functions.

Speed	RD Strips	TD Strips
6.35 mm/s	$\mu(p) = 0.0142 + 0.0025p$	$\mu(p) = 0.0314 + 0.0007p$
25.4 mm/s	$\mu(p) = 0.0279 + 0.0015p$	$\mu(p) = 0.0286 + 0.0005p$
101.6 mm/s	$\mu(p) = 0.0234 + 0.0003p$	$\mu(p) = 0.0296 + 0.0002p$

Then, the obtained friction coefficient functions are plotted on the axes of contact pressure and sliding speed as shown in Figures 5.28 and 5.29. The red dotted lines are the original curves at discrete speeds and the friction coefficient surface is created based on those using quadratic shape functions, which are pertinent to a finite element method. The created friction surfaces can be effectively implemented to a finite element code and the details will be discussed in the next chapter.

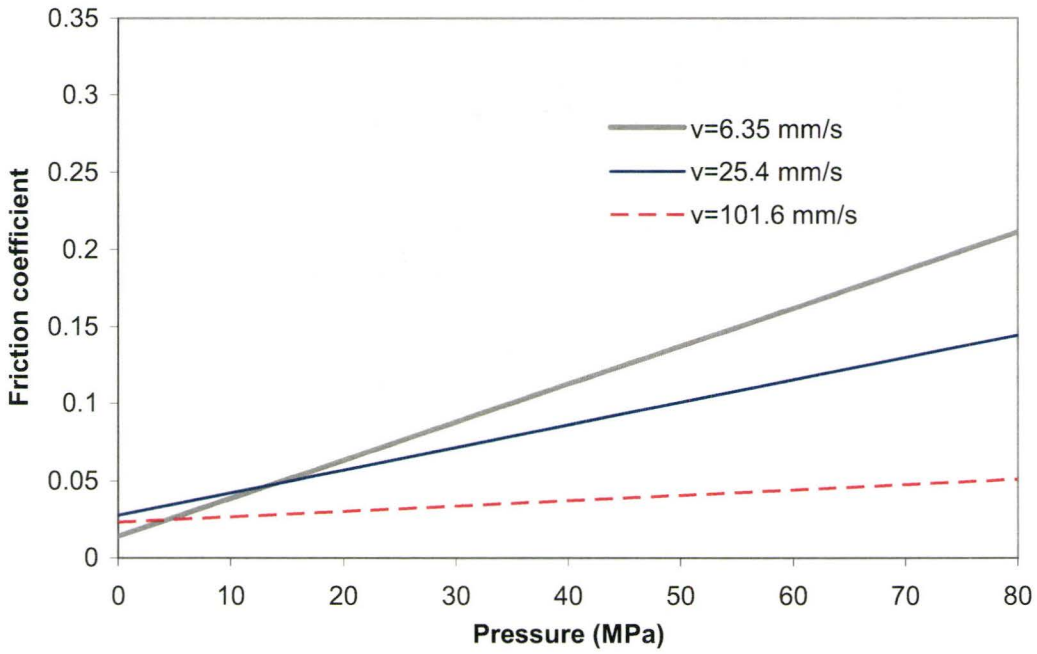

Figure 5.26 Friction coefficients with diluted lubricant (RD).

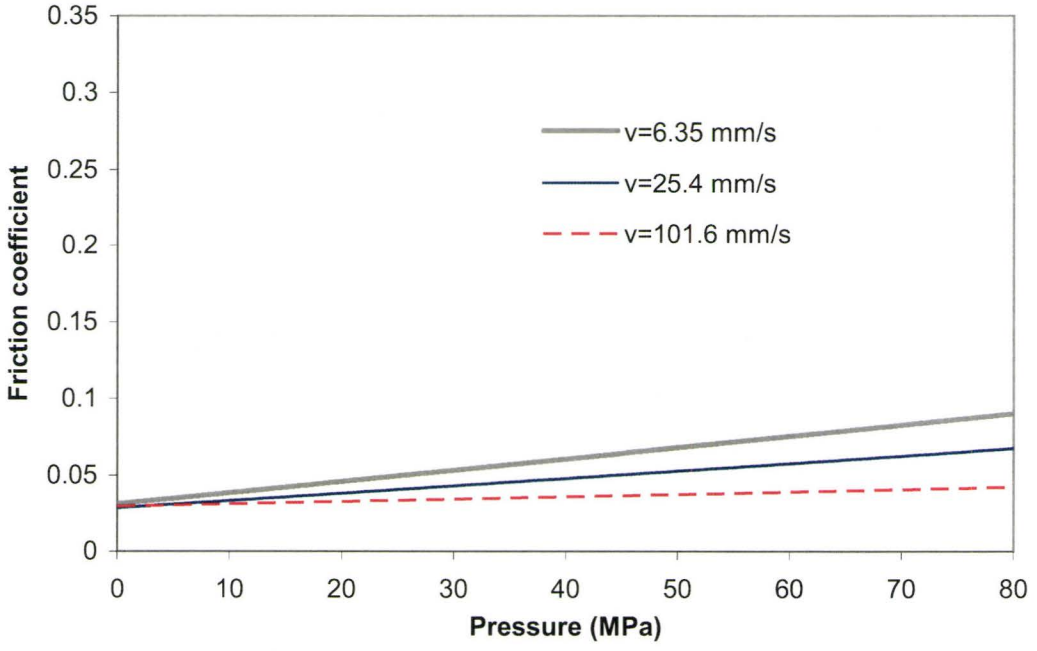

Figure 5.27 Friction coefficients with diluted lubricant (TD).

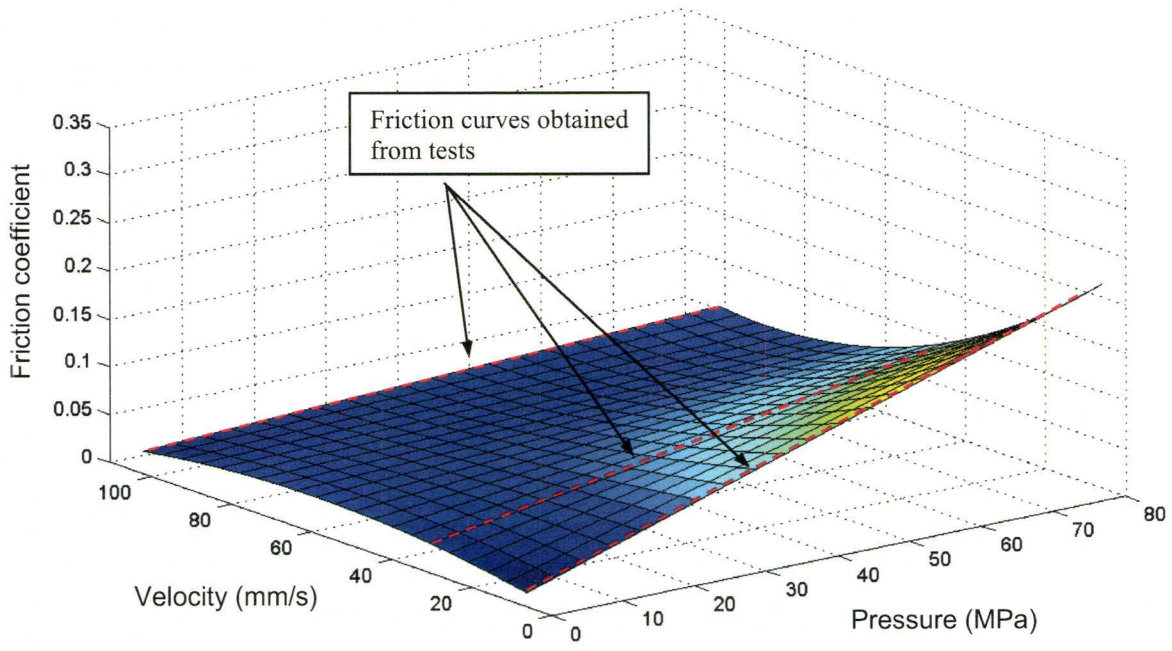

Figure 5.28 Friction coefficient surface with diluted lubricant (RD strips).

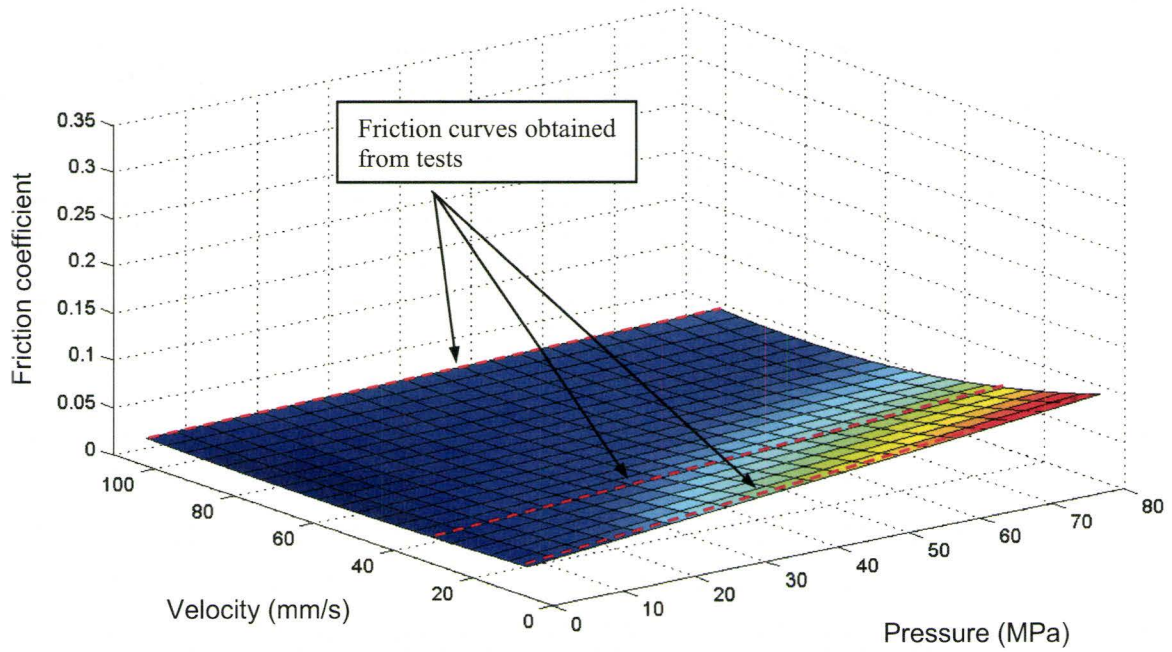

Figure 5.29 Friction coefficient surface with diluted lubricant (TD strips).

5.8. Friction Tests in Undiluted Lubricant Condition

In the friction tests and analyses presented in the previous sections, the 42 mm diameter pin case was omitted because the surface profile of this newly made pin was different from the existing 12.7 mm and 25.4 mm diameter pins. This limited the new method to estimating the friction coefficients as linear functions of pressure. To demonstrate the capability of the new method for the estimation of friction coefficient functions in a more general form, the same tests are repeated in a rich lubricant condition. In this way, the effect of surface roughness on friction is expected to be reduced because more loads will be carried by the lubricant than the interacting surface roughness. Then, the new method is applied to the test results including the 42 mm diameter pin case. For the demonstration purpose of this section, an undiluted MP404 lubricant has been brushed on the surfaces of RD strips (approximately 5 - 6 g/m^2). The draw-bend tests have been performed on the three fixed pins at three speeds.

Figure 5.30 shows the friction coefficients estimated from the tests by the conventional method. The increase of the friction coefficient with 42 mm diameter pin compared to the friction coefficient with 25.4 mm diameter pin has been reduced. Then, the new method has been applied to all three pin results. Now, with test results with three pins the friction coefficient can be estimated as a second of polynomial function of pressure. The measured friction forces and average pressure ratios were summarized in Tables 5.17 and 5.18. Solving the matrix equations in Equation (5.3) applying these data

with pressure maps, the friction coefficient function is obtained as shown in Figures 5.31 and 5.32.

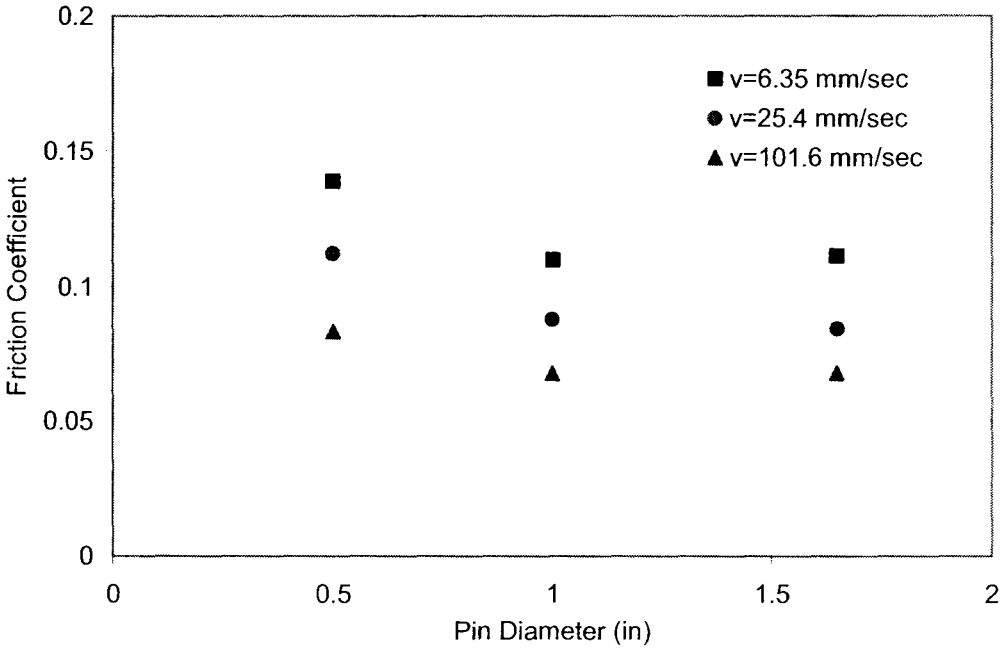

Figure 5.30 Friction coefficients of RD strips by conventional method (undiluted lubricant).

Table 5.17 Friction Forces with Undiluted Lubricant.

Speed	RD		
	12.7 mm Pin $(F_{fric})_1$	25.4 mm Pin $(F_{fric})_2$	42 mm Pin $(F_{fric})_3$
6.35 mm/s	344.15 N	312.13 N	325.15 N
25.4 mm/s	267.67 N	248.82 N	261.74 N
101.6 mm/s	219.29 N	186.29 N	176.35 N

Table 5.18 Average Pressure Ratio (Fixed-Pin Test / Rotating-Pin Test).

Speed	RD		
	12.7 mm Pin c_1	25.4 mm Pin c_2	42 mm Pin c_3
6.35 mm/s	1.094	1.080	1.082
25.4 mm/s	1.071	1.063	1.066
101.6 mm/s	1.057	1.046	1.044

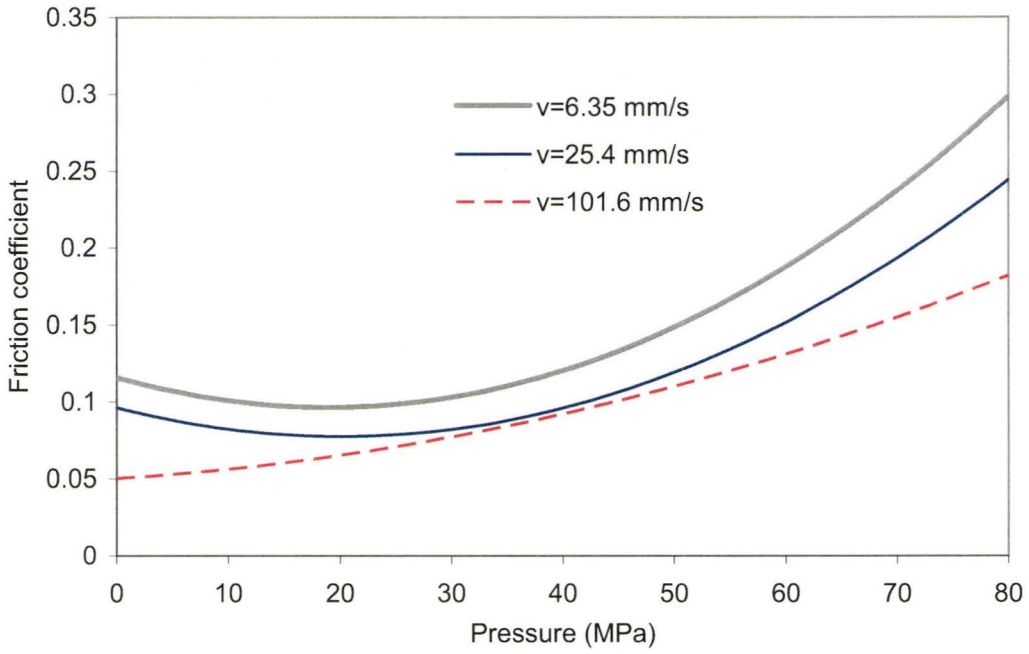

Figure 5.31 Friction coefficients with undiluted lubricant (RD).

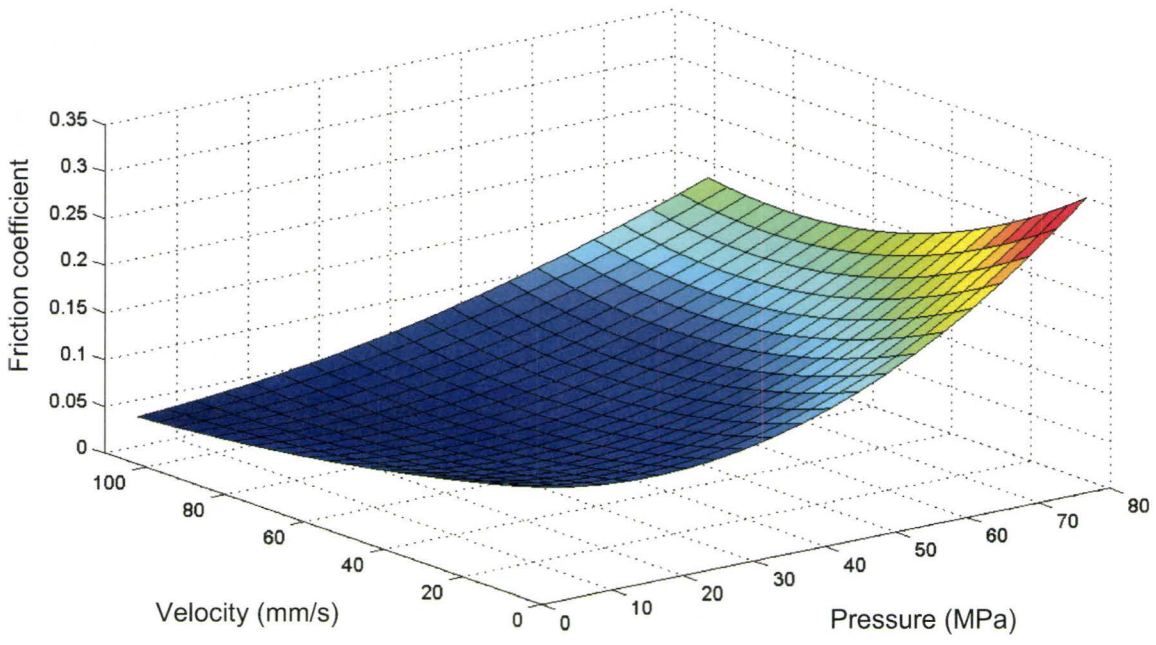

Figure 5.32 Friction coefficient surface with undiluted lubricant (RD).

5.9. Discussion of the Results

5.9.1. Friction Coefficient with Diluted Lubricant

By the new method the friction coefficient surfaces have been obtained as shown in Figures 5.28 and 5.29 for RD and TD strips with diluted MP404 lubricants. RD strips show higher friction coefficient values than TD strips in general. At higher sliding speeds the friction coefficients become more pressure independent and the difference between RD and TD strips is also reduced. This is because the contact comes close to a hydrodynamic lubrication condition at higher sliding speed while the load is carried more by lubricant films.

The friction coefficient is higher in rolling direction than transverse direction, which agrees with the test results by other researchers for mill-finished aluminum sheets (Murtha et al., 1995; Saha et al., 1996; Kenny et al., 2000; Roizard et al., 1999).

5.9.2. Friction Coefficient with Undiluted Lubricant

Figure 5.32 shows the obtained friction coefficient surface for RD strips with undiluted lubricants. Including the 42 mm diameter pin case to the analysis, the friction coefficient could be estimated at each sliding speed as a second order polynomial function. The friction coefficient value at a lower pressure region seems to have some error due to the 42 mm diameter pin data, which have more decisive effect on the shape

of friction curves at lower pressure regions. These additional tests and analyses have been performed to show the capability of the new method for the estimation of friction coefficient functions in a general form.

CHAPTER 6

APPLICATION OF FRICTION MODEL TO SHEET METAL FORMING SIMULATIONS

6.1. Introduction

In this chapter, the friction model developed in the previous chapters is implemented into the finite element code, H3DMAP. Using interpolation (shape) functions, which are pertinent in finite element method, the model is effectively implemented into a finite element code. The implementation of the model is validated by simulations of a simple block model sliding on a flat surface.

For experimental validation of the new friction model, circular cup drawing tests and simulations are performed with a wide range of punch speeds. The friction model is validated by comparing the punch forces, drawn cup sizes, and failure locations.

6.2. New Friction Model

In Chapter 5, friction curves were acquired as functions of contact pressure at discrete sliding speeds. Using polynomial functions, the friction coefficient μ can be interpolated over the domain of contact pressure p and sliding speed v. Figures 5.28,

5.29 and 5.32 showed the friction coefficient curves obtained from the tests and a friction coefficient surface interpolated from the curves. Figure 6.1 and Equation (6.1) show a nine-node isoparametric element and its shape functions, which was used for the interpolation (Kwon and Bang, 2000).

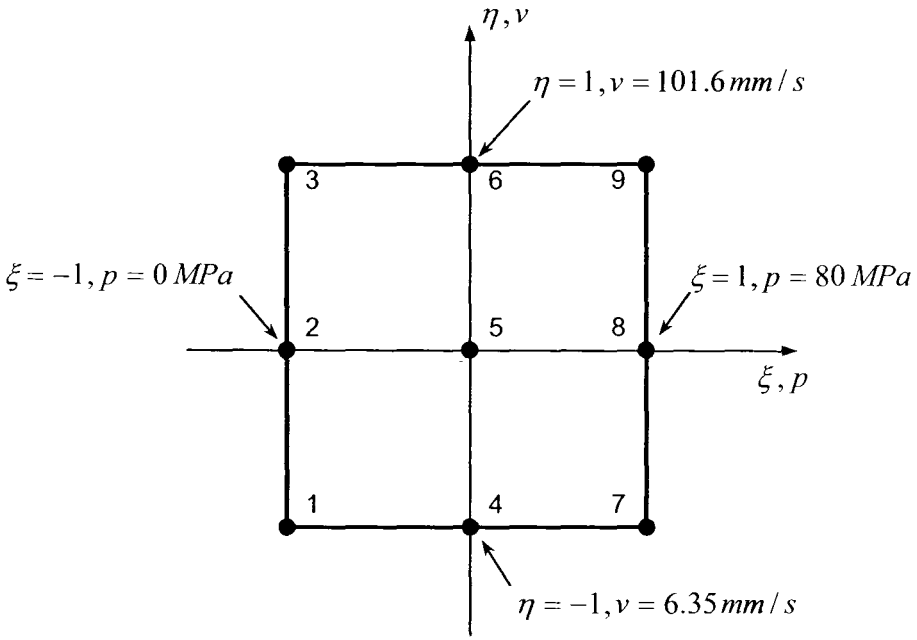

Figure 6.1 Nine-node isoparametric element.

$$
\begin{aligned}
N_1 &= \frac{1}{4}(\xi^2-\xi)(\eta^2-\eta) \quad & N_2 &= \frac{1}{2}(\xi^2-\xi)(1-\eta^2) \quad & N_3 &= \frac{1}{4}(\xi^2-\xi)(\eta^2+\eta) \\
N_4 &= \frac{1}{2}(1-\xi^2)(\eta^2-\eta) \quad & N_5 &= \frac{1}{2}(1-\xi^2)(\eta^2-\eta) \quad & N_6 &= \frac{1}{2}(1-\xi^2)(\eta^2+\eta) \\
N_7 &= \frac{1}{4}(\xi^2+\xi)(\eta^2-\eta) \quad & N_8 &= \frac{1}{2}(\xi^2+\xi)(1-\eta^2) \quad & N_9 &= \frac{1}{4}(\xi^2+\xi)(\eta^2+\eta)
\end{aligned} \tag{6.1}
$$

In the interpolation, the horizontal coordinate of the element is regarded as a contact pressure, the vertical coordinate represents sliding speed, and the friction coefficient μ is obtained over the element domain as follows.

$$\mu = \sum_{1}^{9} N_i(p, v)\mu_i \tag{6.2}$$

where $N_i's$ are shape functions in Equation (6.1) and $\mu_i's$ are friction coefficients at nodal locations.

Figure 6.2 shows the process of interpolation for the case of RD strips with diluted lubricant in Chapter 5, where red-dotted lines are the friction curves obtained from tests. The nodal values are directly decided from the friction curves except at nodal locations of 2, 5, and 8. However, those values can be assessed as illustrated by white-dotted lines in Figure 6.2. For example, the value at node 5 can be interpolated from the values at nodes 4, 5′, and 6.

Table 6.1 summarizes the friction coefficient values at nine nodal locations for RD and TD strips with diluted lubricant. Equation (6.2) with these nodal values as input becomes the new friction model, which is ready to be implemented into a finite element code.

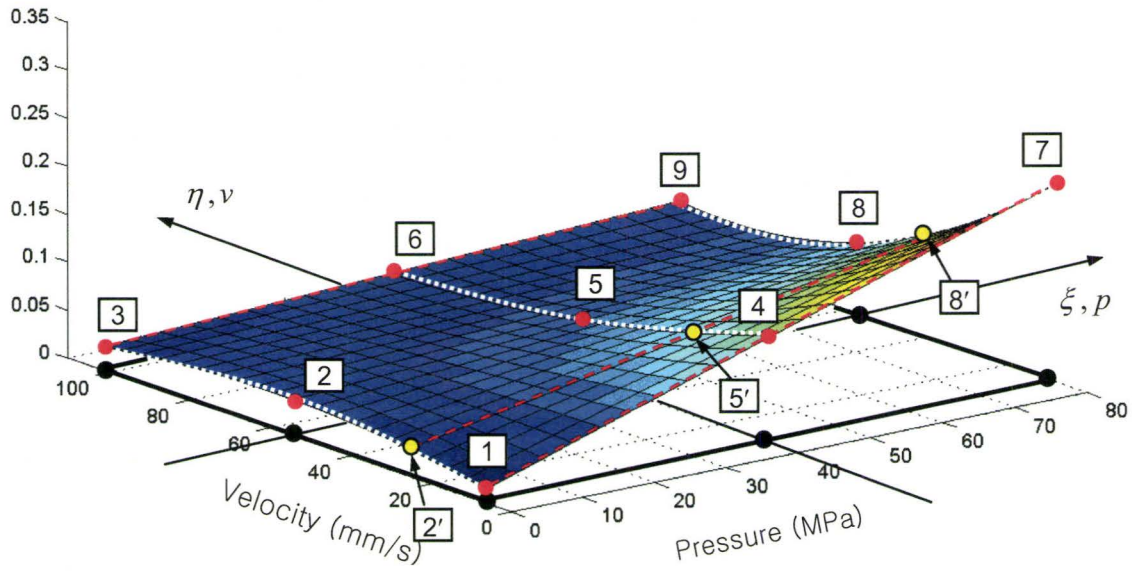

Figure 6.2 Friction coefficient surface obtained for RD strips with diluted lubricant.

Table 6.1 Friction coefficients at nine nodal locations for RD and TD strips with diluted lubricant

	RD	TD
node 1	0.0142	0.0314
node 2	0.0373	0.0267
node 3	0.0234	0.0296
node 4	0.1142	0.0594
node 5	0.0583	0.0384
node 6	0.0354	0.0376
node 7	0.2142	0.0874
node 8	0.0793	0.0502
node 9	0.0474	0.0456

6.3. Implementation of New Friction Model

Figure 6.3 shows the existing contact algorithm with Coulomb friction model in H3DMAP code. In the algorithm, nodes (slave nodes) on one of contact-boundary pair are checked for the penetration into the surfaces (master segments) of the opposing contact-boundary. The contact force normal to the master segment is calculated by multiplying contact penalty stiffness α_k to the penetration δ (see Step 1 in Figure 6.3). The contact stiffness α_k is based on the properties of underlying elements at the contact boundary and is determined according to the geometry and material properties of the contacting element [Shi]. In the presence of friction, two surfaces in contact do not start sliding relative to one another until a tangential force reaches a certain magnitude. This critical force F_T^{crit} is defined as a fraction of the normal force F_N. The fraction μ, which is a constant in the current friction model, is referred to as friction coefficient. The algorithms for this stick/slip conditions are explained in Steps 3 to 5.

The new friction model was implemented into the finite element code H3DMAP (Sauvé, 1999) by modification of the existing friction model. Instead of constant μ in the existing Coulomb friction model, Equation (6.2) with its shape functions was coded so that μ can be calculated from the current conditions of contact pressure and sliding velocity. Because the shape functions in Equation (6.2) are expressed in natural coordinates, the pressure and sliding speed are mapped to the natural coordinates according to the Equation (6.3). The nine nodal values in Table 6.1 become the input for

the friction model, flow of calculations for this modification with new friction model are shown in Figure 6.4.

$$\xi = 2p/(p_{\max} - p_{\min}) - 1, \ \eta = 2v/(v_{\max} - v_{\min}) - 1 \tag{6.3}$$

where $p_{\max}$ (80 MPa) and $p_{\min}$ (0 MPa) are the range of the applied contact pressure, and $v_{\max}$ (101.6 mm/s) and $v_{\min}$ (6.35 mm/s) are the range of speeds applied in the tests.

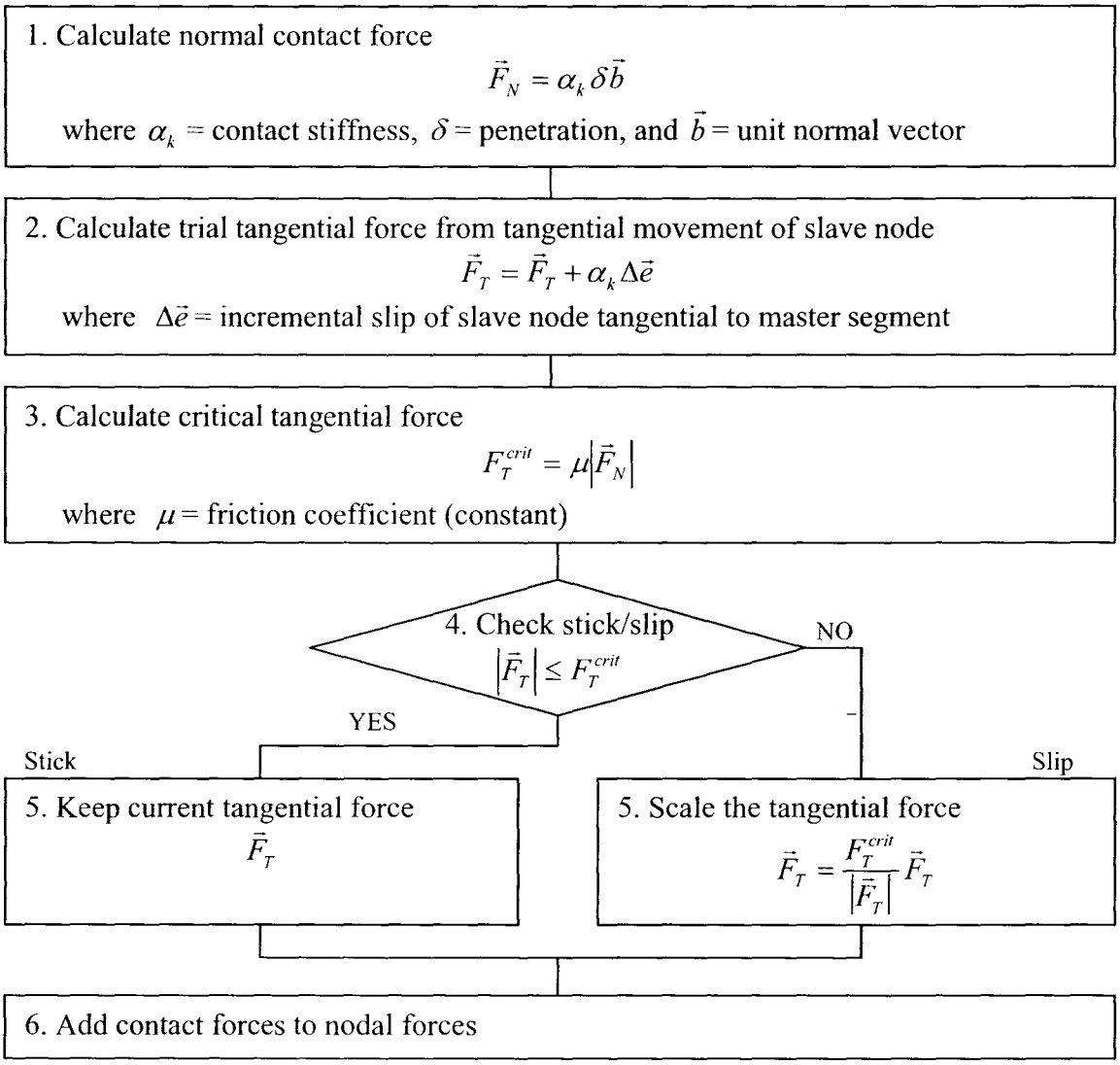

Figure 6.3 Contact algorithm with current friction model.

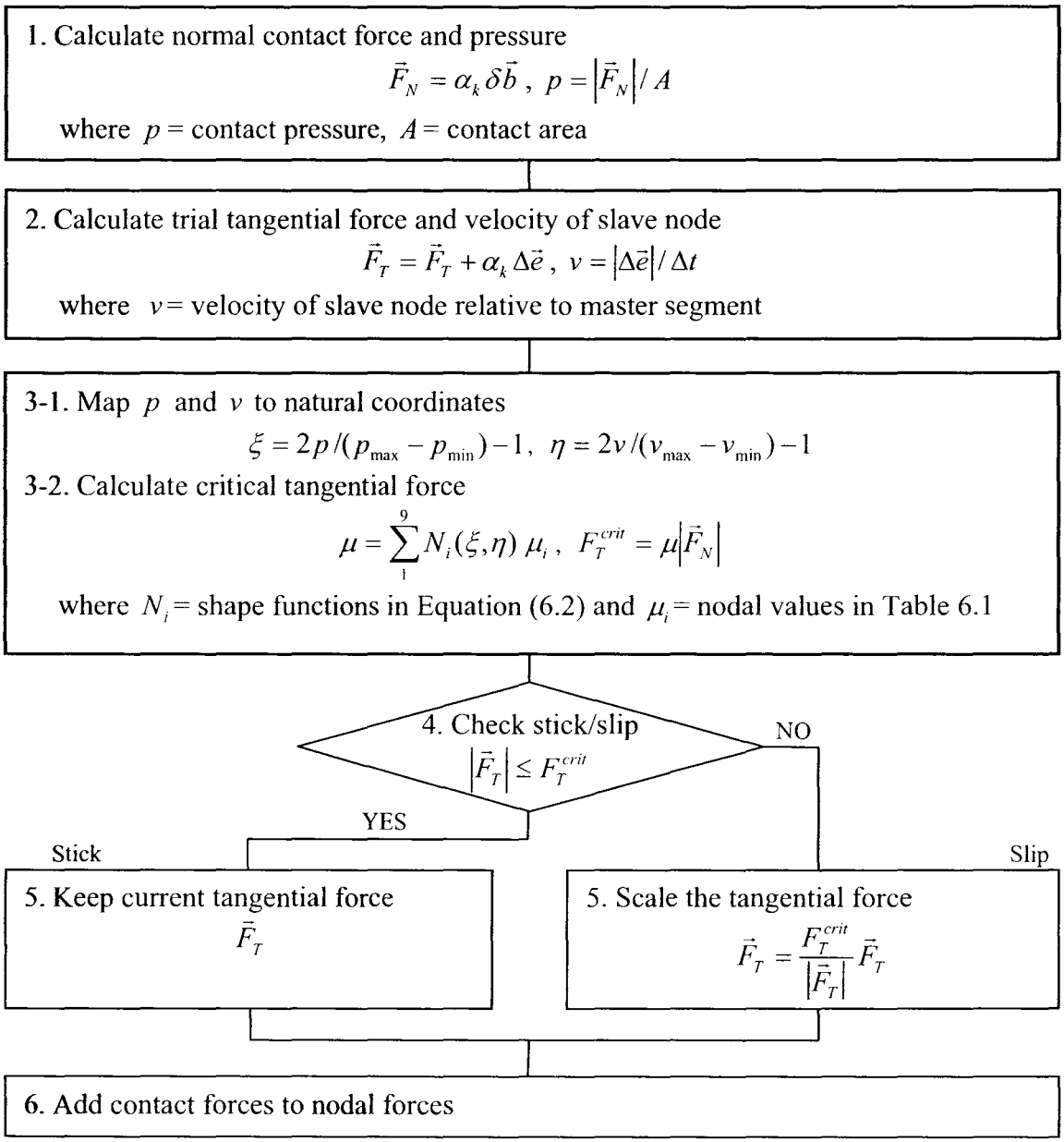

Figure 6.4 Contact algorithm with new friction model (isotropic friction).

6.4. Consideration of Friction Anisotropy in the New Model

It has been reported that mill-finished aluminum sheets have strong directionality in frictional behavior (Murtha et al., 1995; Saha et al., 1996; Kenny et al., 2000; Roizard et al., 1999). The test results in Chapter 5 also showed the same trend with a higher value of friction coefficient in the rolling direction than in the transverse direction. Therefore, two friction coefficient surfaces for RD and TD strips are obtained from tests as shown in Figures 5.28 and 5.29. Two sets of nodal values from these tests as summarized in Table 6.1 become input for the new friction model.

In order to include the friction anisotropy in the new friction model, the algorithm in Figure 6.4 has been extended by adopting the methodology in reference (Abaqus, 1999). In the extended algorithm, the stick/slip criterion is represented by an ellipse as shown in Figure 6.5, whose extreme ends are decided by two values from Equation (6.3). An ellipse is a mathematical form to continuously connect values measured in two orthogonal directions (RD and TD). In the algorithm with the new friction model, the size and shape of this ellipse will change depending on the pressure and velocity conditions. Figure 6.6 shows the details of the algorithm for the new model with considered frictional anisotropy.

$$F_{Tx}^{crit} = \mu_x \left| \vec{F}_N \right|, \quad F_{Ty}^{crit} = \mu_y \left| \vec{F}_N \right| \tag{6.3}$$

where μ_x and μ_y are friction coefficients for local slip directions denoted as x and y in Equation (6.3) and the local slip directions are defined by the projection of the global X and Y axes onto the contact surface.

For the current model implementation, the projection of the global x-axis onto the contact surface was selected as RD and the projection of y-axis as TD. In Step 2-1) of Figure 6.6, incremental slip $\Delta\vec{e}$ in global coordinate is converted to $\Delta\vec{e}'$ in the projected local coordinate before it is used for the calculation of trial tangential force. Hence, in the sheet forming simulations with the implemented friction model, the RD of the blank sheet has to be oriented to the global x-axis. This algorithm for local textural directions will work well for axisymmetric sheet forming cases such as the circular cup drawing tests, which are used for the model validation in this Chapter. However, this algorithm needs improvements for the general sheet forming cases by defining corotational local axes, which will follow the rotations of the local textural directions of a sheet as deformation proceeds.

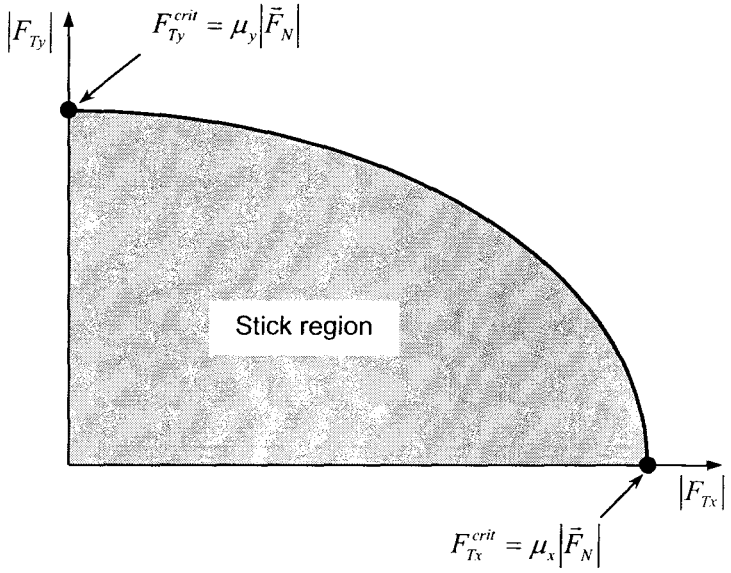

Figure 6.5 Critical shear force surface for anisotropic friction model.

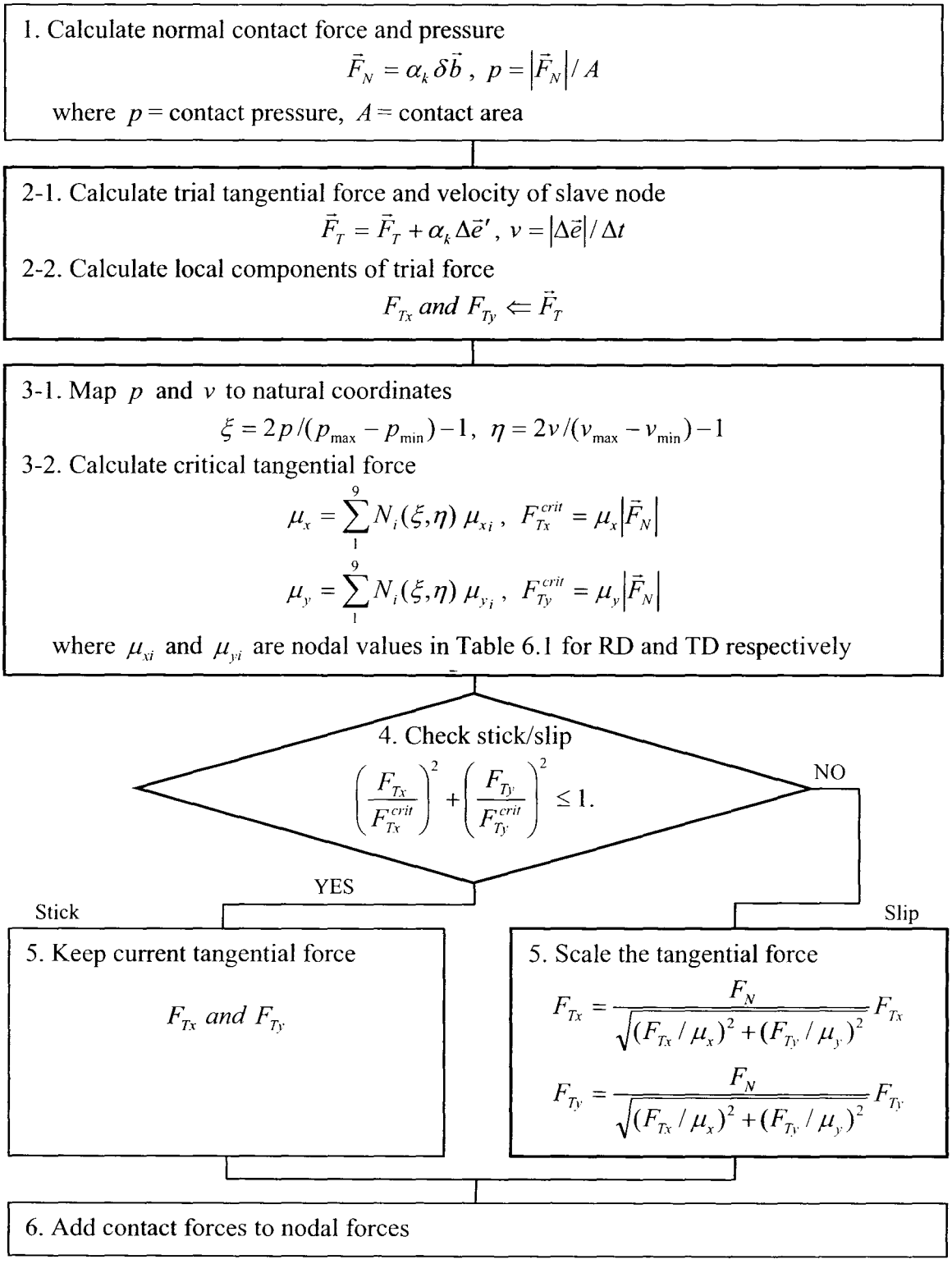

Figure 6.6 Contact algorithm with new friction model (anisotropic friction).

6.5. Verification of the New Friction Model

The code modification for implementation of the new friction model is substantial enough to warrant verification. For this purpose, simple block sliding simulations as shown in Figure 6.7 have been performed. In the simulations, a block with unit width and length was pressed onto the rigid floor by the pressure loads and slid by applying the velocities on the nodes. The shearing forces F_{Tx} *and* F_{Ty} at the contact interface were obtained from the simulation results and the friction coefficients μ_x and μ_y were calculated by dividing them with the applied normal force F_N.

Tables 6.2, 6.3, and 6.4 summarize the simulation cases. For cases in Table 6.2 the block was slid in x-axis (RD) with various pressure loads (10, 40, 70 MPa) and velocities (10, 40, 70, 100 mm/s). For cases in Table 6.3, the block was slid in y-axis with the same pressure loads and velocities. In the cases of Table 6.4, the block was slid in various directions (0° - 90°) at pressure load of 10 MPa and velocity of 50 mm/s. Figures 6.8, 6.9 and 6.10 compare the retrieved friction coefficients and the data from input friction model. The comparisons show good agreements verifying the correct implementation of the new friction model in the code.

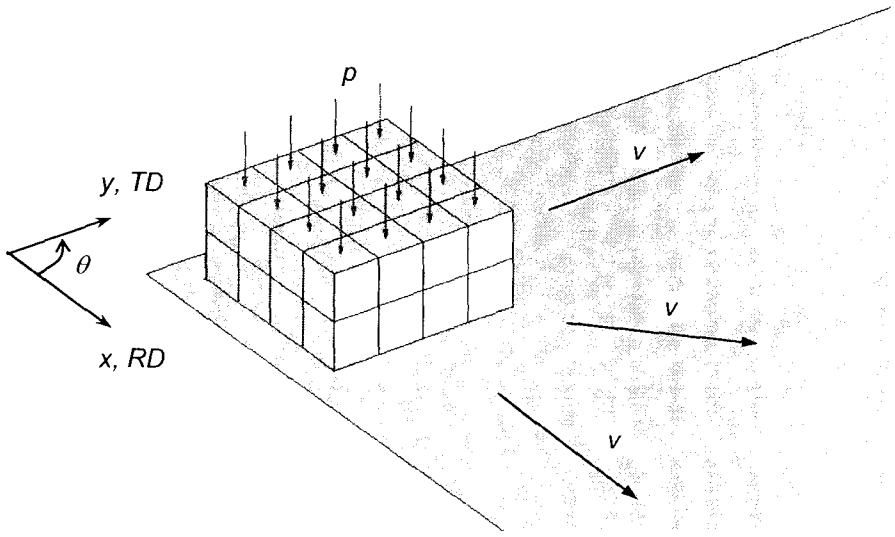

Figure 6.7 Block sliding simulations for verification of new friction model.

Table 6.2 Simulation cases of sliding in rolling direction (0°)

Direction	Pressure (MPa)	Speed (mm/s)
RD	10	10
RD	10	40
RD	10	70
RD	10	100
RD	40	10
RD	40	40
RD	40	70
RD	40	100
RD	70	10
RD	70	40
RD	70	70
RD	70	100

Table 6.3 Simulation cases of sliding in transverse direction (90°)

Direction	Pressure (MPa)	Speed (mm/s)
TD	10	10
TD	10	40
TD	10	70
TD	10	100
TD	40	10
TD	40	40
TD	40	70
TD	40	100
TD	70	10
TD	70	40
TD	70	70
TD	70	100

Table 6.4 Simulation cases of sliding in various directions

Direction	Pressure (MPa)	Speed (mm/s)
0°	10	50
15°	10	50
30°	10	50
45°	10	50
60°	10	50
75°	10	50
90°	10	50

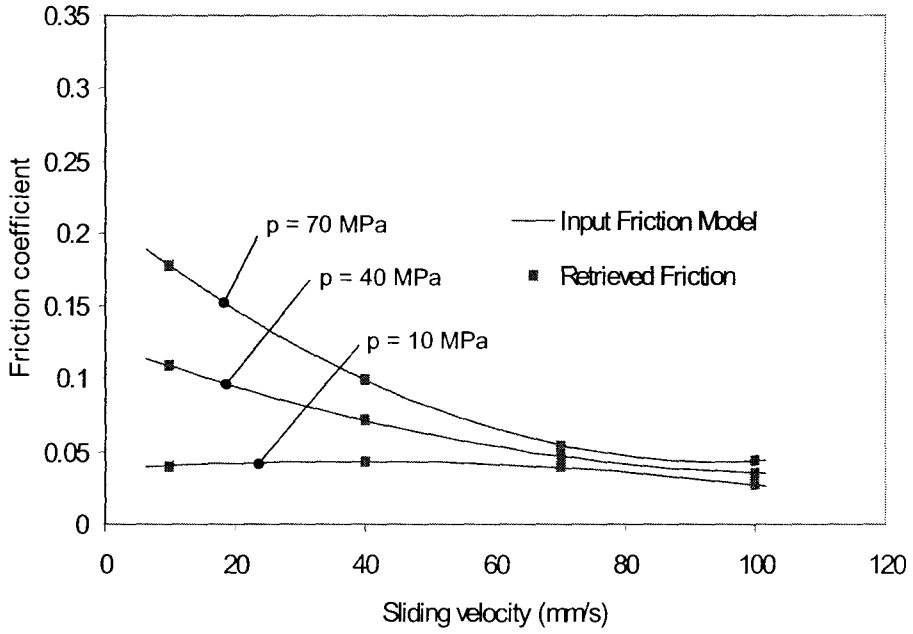

Figure 6.8 Comparison: input friction model data vs. retrieved friction coefficients for RD sliding cases.

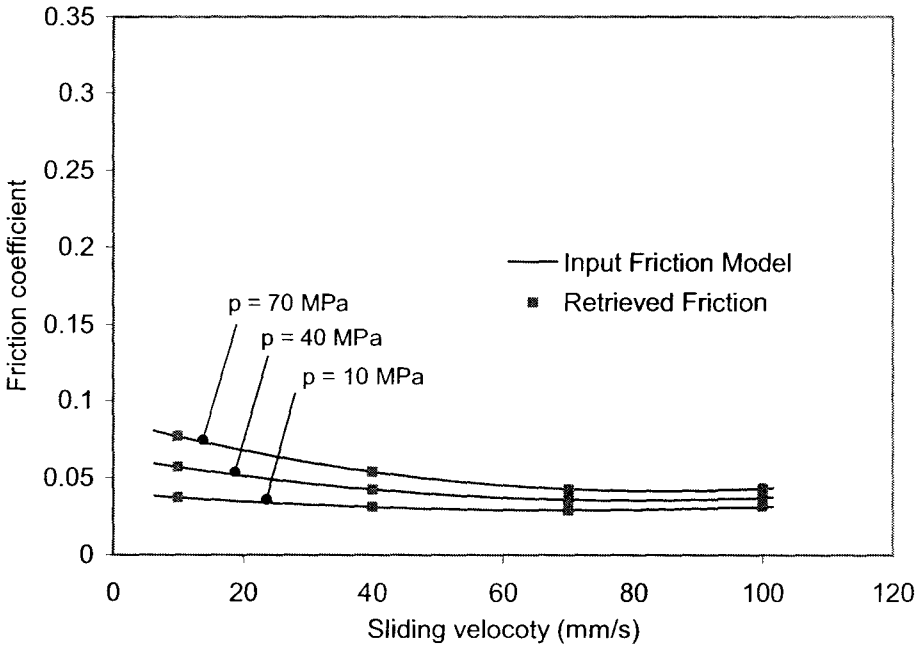

Figure 6.9 Comparison: input friction model data vs. retrieved friction coefficients for TD sliding cases.

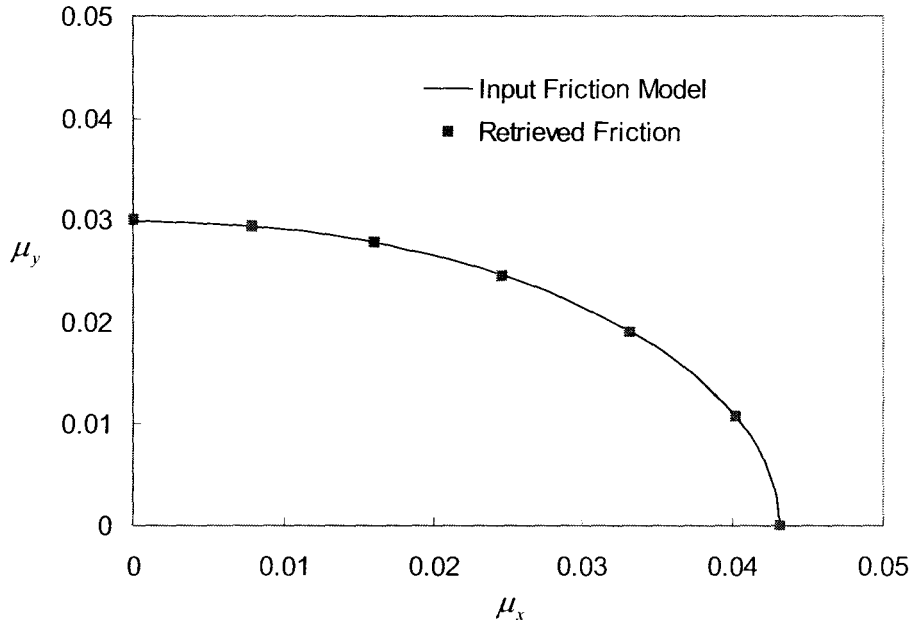

Figure 6.10 Comparison: input friction model data vs. retrieved friction coefficients for sliding cases in various directions (with p=10 MPa and v=50 mm/s).

6.6. Experimental Validation of the New Friction Model

Using simple block sliding simulations, the computational aspect of the new friction model has been verified in the previous section. Now, the model will be validated using circular cup drawing experiments. Among various lab based sheet forming tests, the cup drawing test involves sliding of material in the flange as well as bending, unbending and stretching - all modes that apply to 'real' forming processes.

6.6.1. Circular Cup Drawing Experiments

Circular cup drawing experiments have been performed to validate the new friction model. A 250 kN servo-hydraulic mechanical testing system (MTS) available at McMaster University with existing tool and dies was used for the experiments as shown in Figure 6.11. The device has two hydraulic actuators, which control the motions of the upper die and a punch. The geometries of the punch and dies are given in Figure 6.12. The punch and dies are made of A2 tool steel and hardened to 55 to 58 Rc and the surfaces are in near-mirror polished conditions. The surface conditions of the punch and dies are similar to the conditions of the pins used in the friction tests in Chapter 5 except that the material is A2 tool steel instead of H13 tool steel.

For this experimental work, AA5754-O sheets had been machined to 111.25 mm diameter disks. Figure 6.13 shows the sheet samples prepared for the cup drawing experiments. The sheet materials were provided also by Novelis Global Technology Centre (NGTC) from the same coil (49256-B1D1 at 1.05 mm) used for the draw-bend

friction tests in Chapter 5. Lubrications were carefully applied to the sheet samples by dipping the samples into MP404 lubricant solution diluted with Hexanes following the method used to prepare the strips for the draw-bend friction tests.

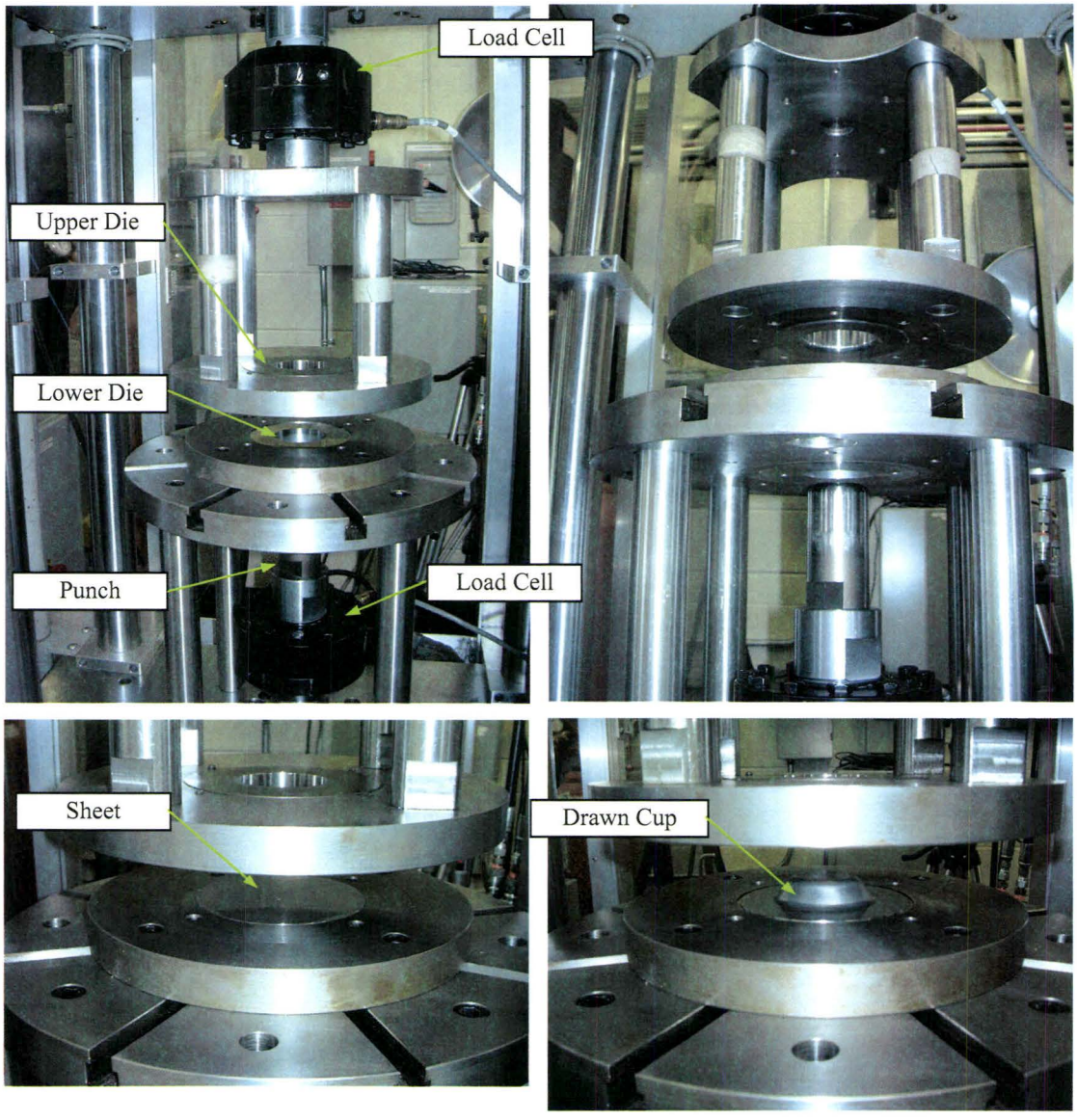

Figure 6.11 Details of circular cup drawing device.

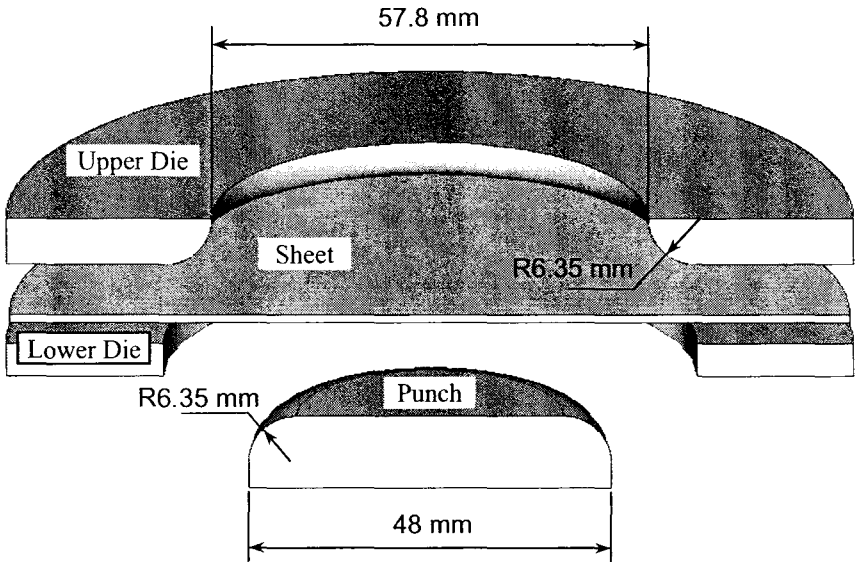

Figure 6.12 Geometries of punch and dies.

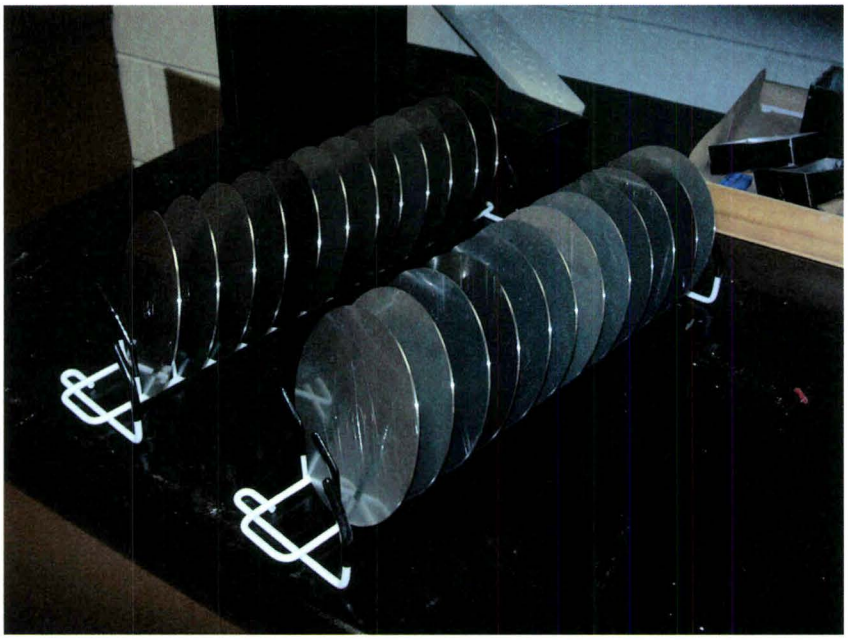

Figure 6.13 Sheet samples for cup drawing experiments.

The test procedures were as follows.

1) A sheet sample is placed on top of lower die, which is fixed to the bed of the test system.
2) The upper die moves down by the actuator until the sheet sample is clamped between the dies with clamping force of ~20 kN.
3) The punch moves upward by the actuator with a predefined speed while the upper die is stationary.

During the tests, the forces from the upper die and the punch and the displacement of the punch were measured.

Due to the relatively large difference between punch (48 mm) and upper die (57.8 mm) diameters, the drawn cups become conical shapes and the punch displacement of

~17 mm was the maximum before the material fails as shown in Figure 6.14. Tests were performed with the nine different punch speeds shown in Table 6.5. The actuator for the punch motion was controlled to stop at the punch displacement of ~17 mm for each case.

Table 6.5 Punch speeds applied in tests

Case 1	Case 2	Case 3	Case 4	Case 5	Case 6	Case 7	Case 8	Case 9
6.4 mm/s	12.8 mm/s	19.3 mm/s	25.3 mm/s	31.5 mm/s	37.5 mm/s	42.8 mm/s	47.6 mm/s	77.1 mm/s

Figure 6.15 shows the force and displacement data from the test Case 1. It can be noticed from the circled part of the graph that the punch was not in touch with the sheet because the punch force is not increased until some displacement of the punch. Calibrating this offset of the data, punch forces were plotted against the punch displacements for the all nine cases as shown in Figure 6.16. As the punch speed increased, the punch force decreased, clearly showing the effect of the sliding speed dependence of the frictional force.

Cup sizes of the drawn samples were measured for the nine test Cases. Measurements were done on the rolling and transverse direction of the samples as marked in Figure 6.14. Measured cup sizes were plotted against the punch speed as given in Figure 6.17. They show the frictional effects on the final shape of the sample. As the punch speed increases, the sheet material draws in more resulting in a smaller cup size. The draw-in is greater in the transverse direction due to the lower frictional force in that direction.

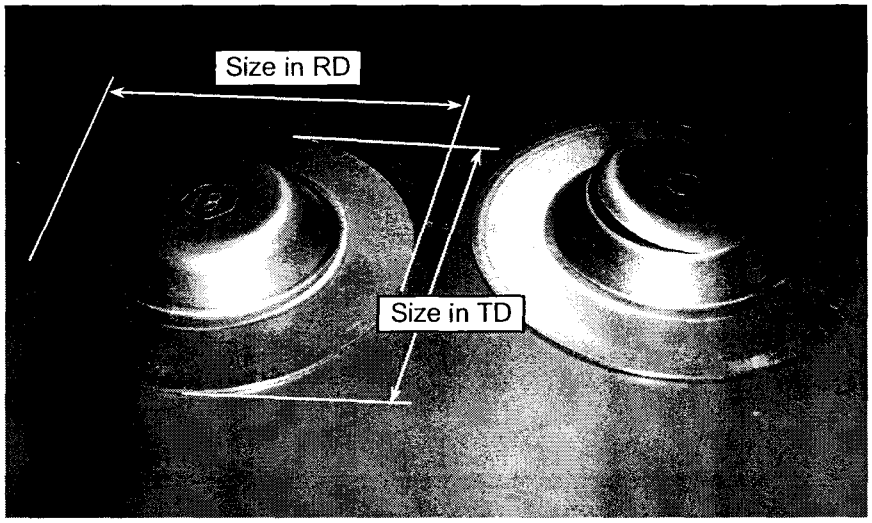

Figure 6.14 Drawn cup samples.

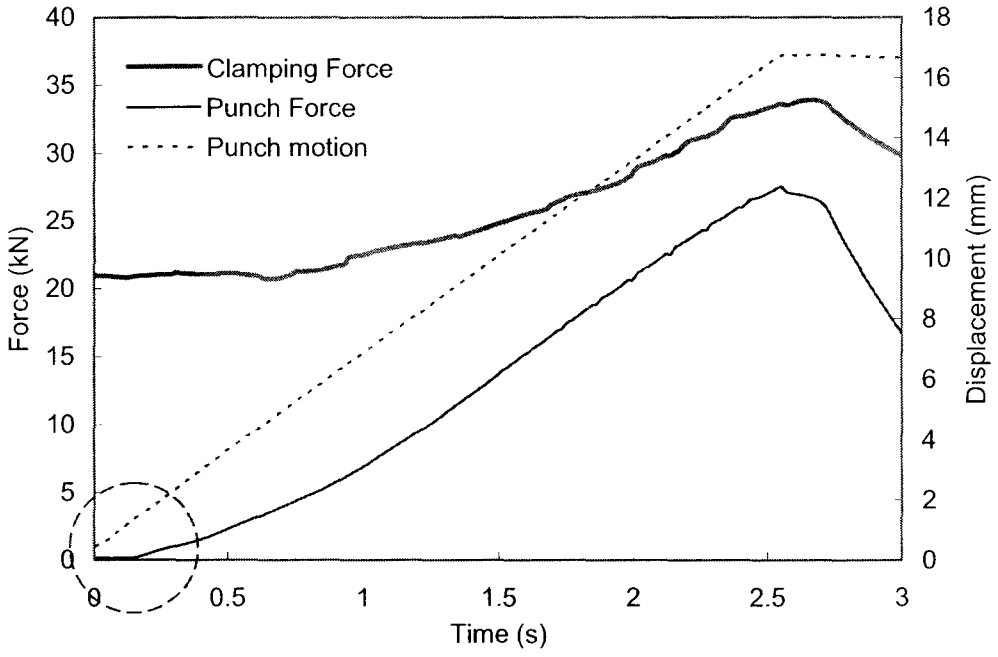

Figure 6.15 Force and displacement data from case 1 (punch speed: 6.4 mm/s).

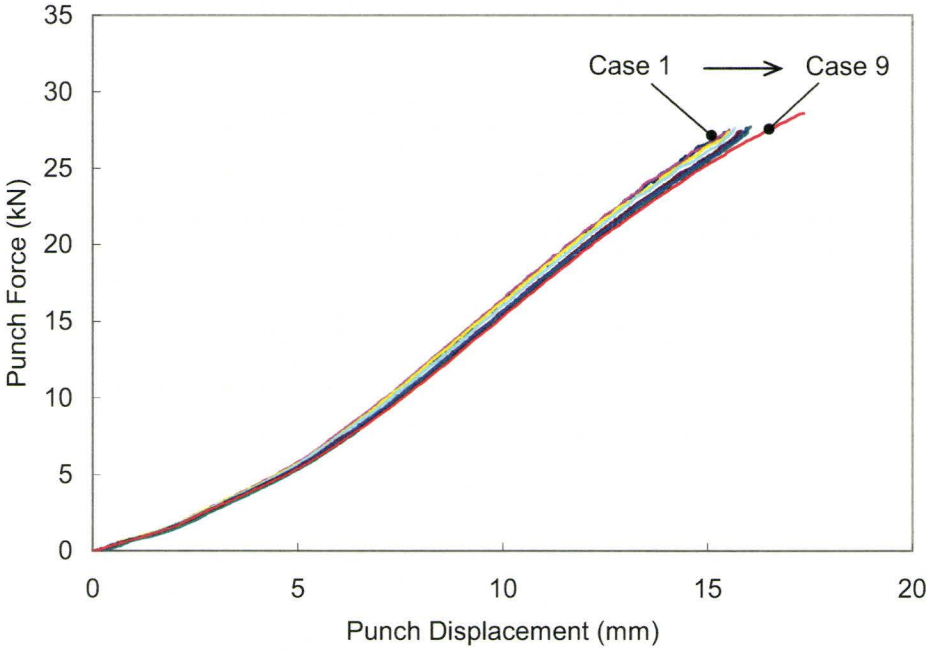

Figure 6.16 Punch force/displacement curves from tests for all nine cases.

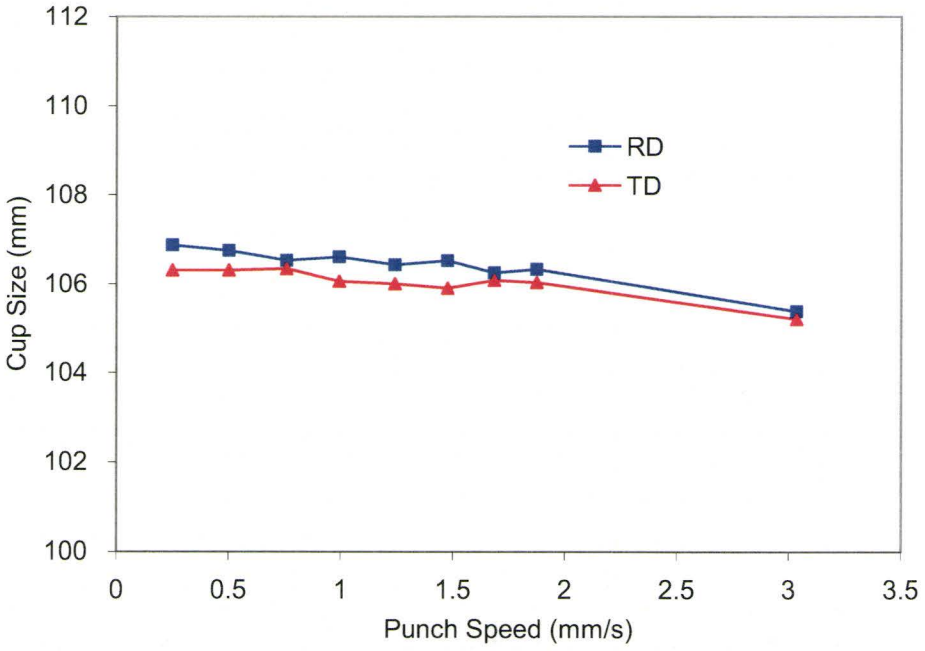

Figure 6.17 Cup sizes from tests for all nine punch speeds.

6.6.2. Circular Cup Drawing Simulations

Circular cup drawing simulations were performed for the test cases in Section 6.6.1 using H3DMAP code with the implemented friction model. Figure 6.18 shows the finite element models for cup drawing tests. To exploit the symmetry in boundary conditions, a quarter of the geometry was modeled. Shell elements were used for the punch and dies, and solid elements were used for the sheet sample to be consistent with the models used for the friction model development in this research. Isotropic elastic-plastic material model was used with the stress-strain data from a RD strip shown in Figure 5.1 as input.

The lower die model was fixed for all degrees of freedom and the punch and upper die models were constrained in lateral directions only allowing the motions in vertical direction. All the nodes in the upper die model were tied to a beam (see Figure 6.18) node in vertical direction and these tied constraints with the applied boundary constraints make the upper die behave as a rigid body. The same constraints were applied to the punch model. The beam elements shown in Figure 6.18 were included in the model to make them work like load cells in the test device. The punch and clamping forces in the simulations are collected from the axial stress data of these beam elements.

Simulations were performed following the test procedures applied in the previous Section 6.6.1 for the nine Cases in Table 6.5. In the tests, the actuator for the upper die is fixed while the punch moves up and draws the sheet sample. During this process, upper die displaces a small amount due to the flexibility of the rig that holds the upper die.

Instead of including the stiffness of the rig in the model, the measured clamping forces (a quarter of the force due to the symmetry model) were directly applied to the upper die for the accurate simulations of the tests. This allows a fair assessment of the friction model while avoiding the need to consider the flexibility of the press in detail.

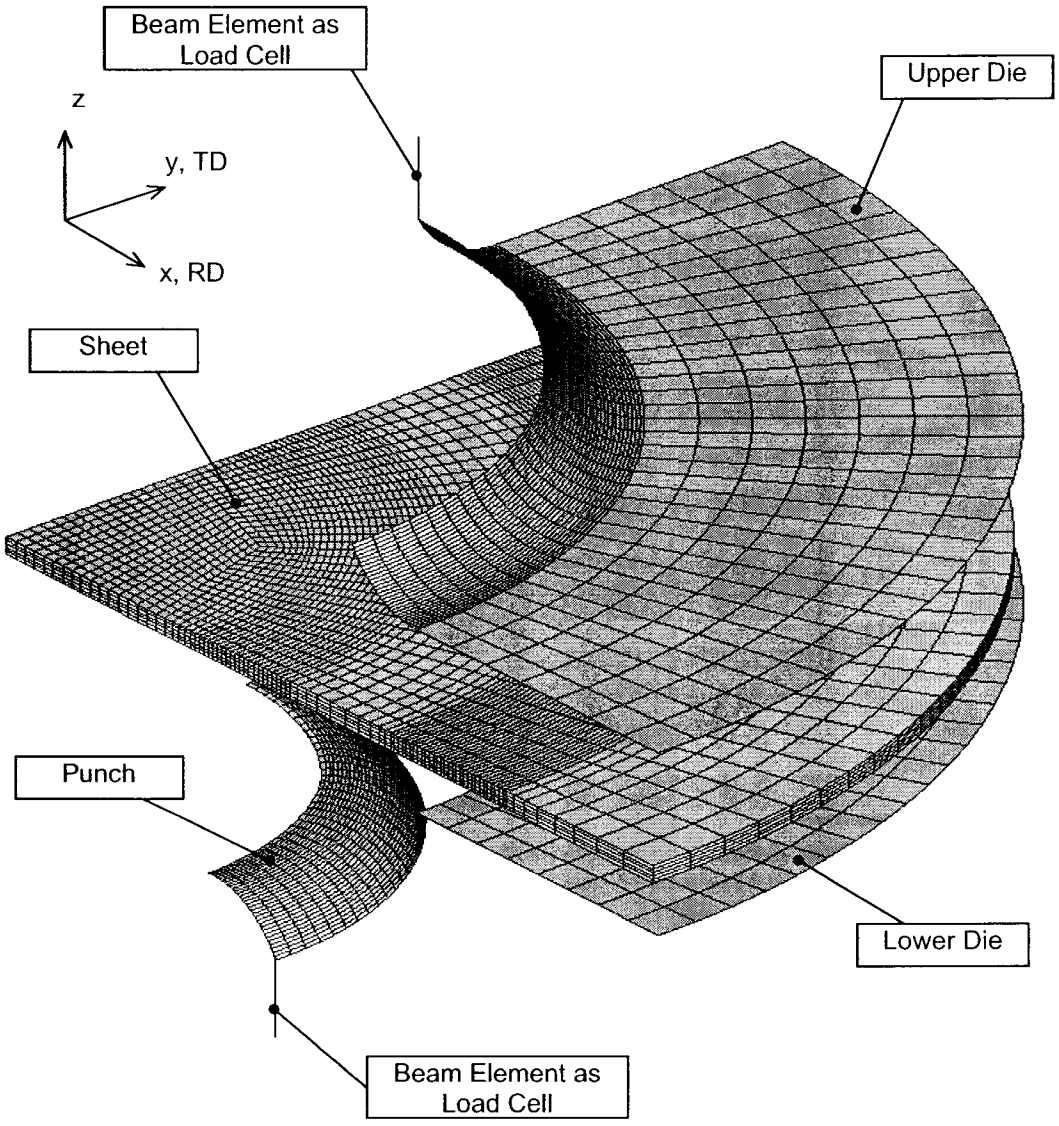

Figure 6.18 Finite element models for circular cup drawing tests.

The deformed shape of the sheet and von Mises stress distribution (in MPa) from the simulation for Case 1 is given in Figure 6.19. The stress level is highest at the punch corner region and the slight difference of stress distribution in RD and TD is noticeable. This is from the frictional anisotropy because isotropic material properties were applied to the simulations.

Figure 6.20 shows punch forces plotted against the punch displacements from the simulations for all nine cases. Following the trend in the tests, the punch force consistently decreased as the punch speed increased. The maximum punch forces at the punch displacement of 15 mm were 27.3 kN and 25.9 kN for Case 1 and Case 9 respectively. As the punch speed is increased from 6.4 mm/s to 77.2 mm/s, the maximum punch force is decreased with magnitude change of -1.4 kN. This is comparable to the experimental results with magnitude change of -1.3 kN (From 26.5 kN to 25.2 kN).

Cup sizes of the sheet model were also obtained from the simulations for the nine test Cases as shown in Figure 6.21. Sizes in the rolling and transverse directions of the sheet were collected to compare with experimental results. They also show the same trend with the test results. As the punch speed increases, the material draw-in is larger, and the draw-in is greater in the transverse direction than in rolling direction.

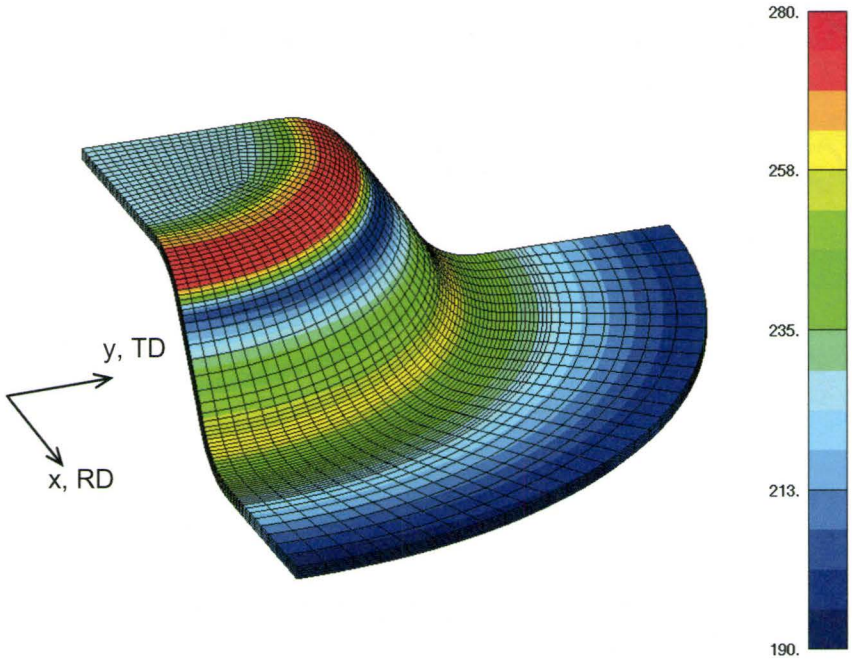

Figure 6.19 Deformed shape and vonMises stress (MPa) distribution of the sheet for case 1.

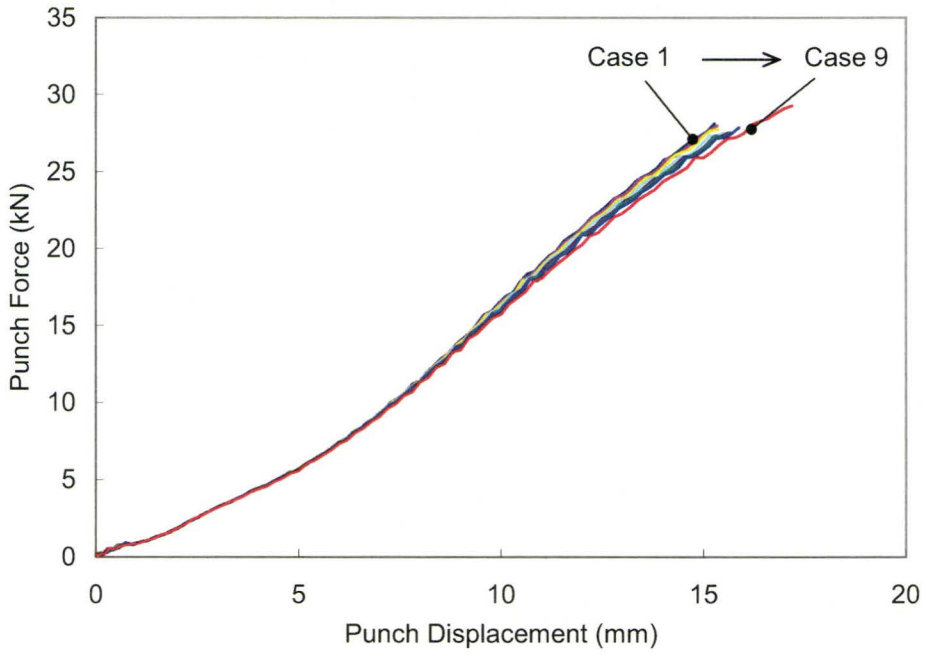

Figure 6.20 Punch force/displacement curves from simulations for all nine cases.

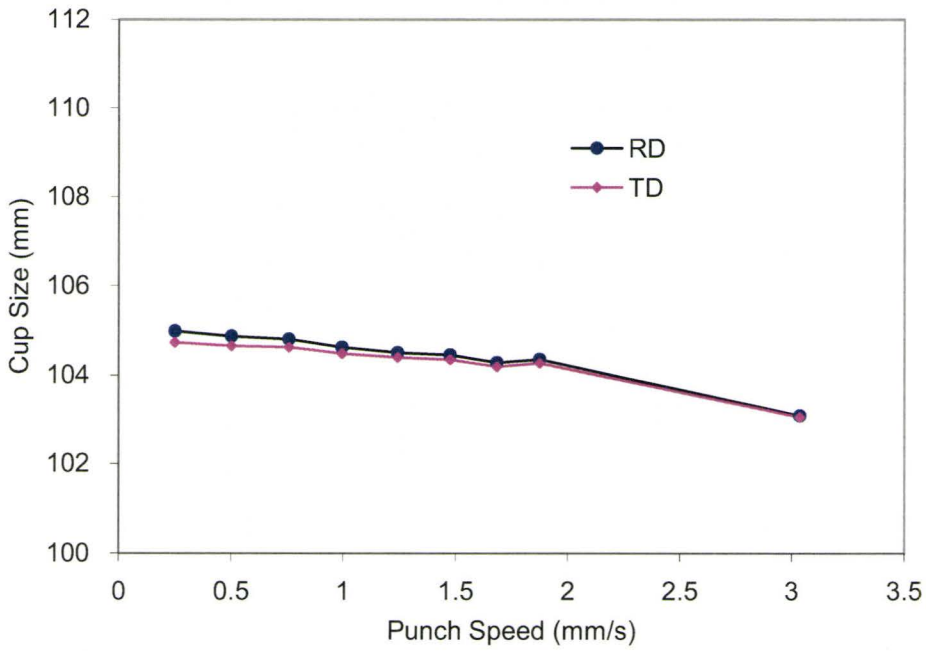

Figure 6.21 Cup sizes from simulations for all nine punch speeds.

6.6.3. Comparison and Discussion of the Results

Punch Forces

Punch forces from simulations agree well with the forces from the tests as can be seen from Figures 6.16 and 6.20. Punch force decreases as the punch speed increases due to the lower frictional force at higher sliding speed, which was observed in the friction tests in Chapter 5. In Figures 6.22 and 6.23, punch forces were compared for the lowest (Case 1) and highest (Case 9) punch speed cases. Maximum punch forces from simulations were 2.9% and 2.4% higher than the measured forces from tests for Case 1 and Case 9 respectively.

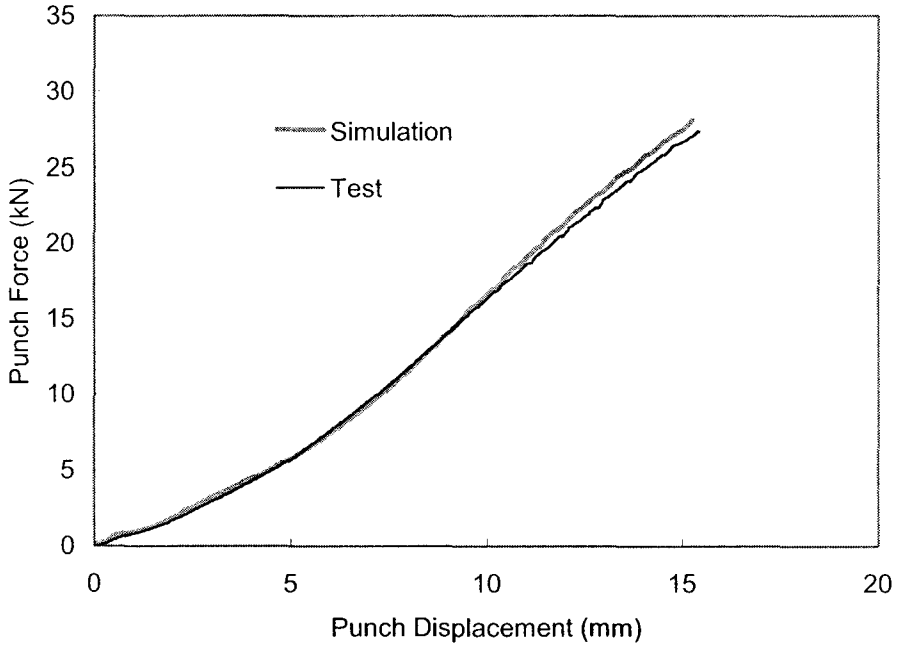

Figure 6.22 Punch force comparison for test case 1 (punch speed: 6.4 mm/s).

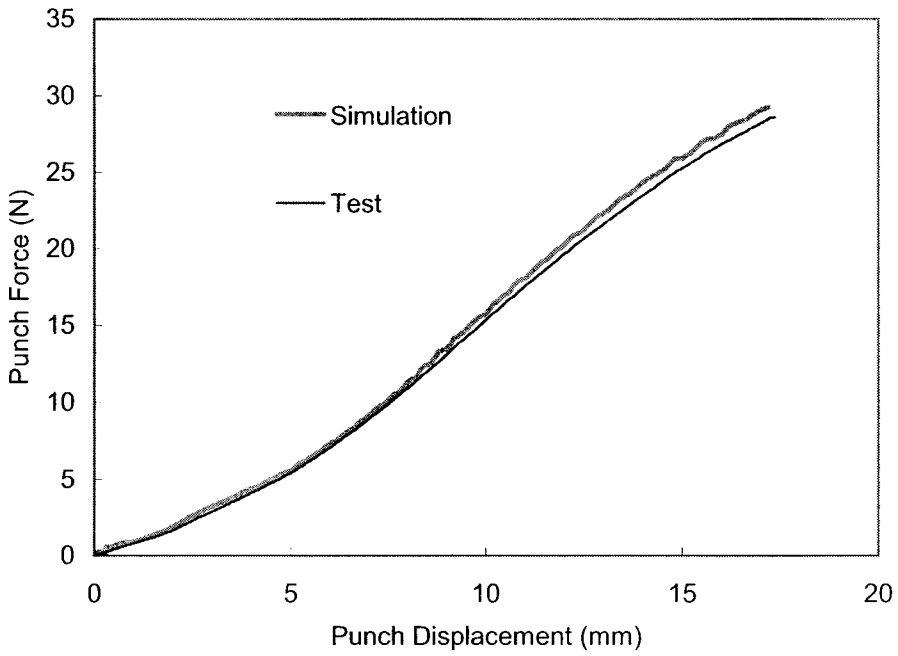

Figure 6.23 Punch force comparison for test case 9 (punch speed: 77.1 mm/s).

Cup Sizes

Figure 6.24 compares cup sizes in RD and TD for all nine punch speed Cases. The simulation results agree well with the test results in the general trend. As the punch speed increases, the cup size decreases because more sheet material is drawn in due to the less frictional force. The draw-in of material in TD is greater than in RD because the frictional force in TD is smaller than in RD. The predicted cup sizes are ~2% smaller than the measured cup sizes. The difference could be attributed to the following factors, which is not considered in the current simulations.

- Material anisotropy as noticed by tensile test data in Figure 5.1
- Spring-back effect of the drawn cups
- Discretization error related to mesh convergence of FE models

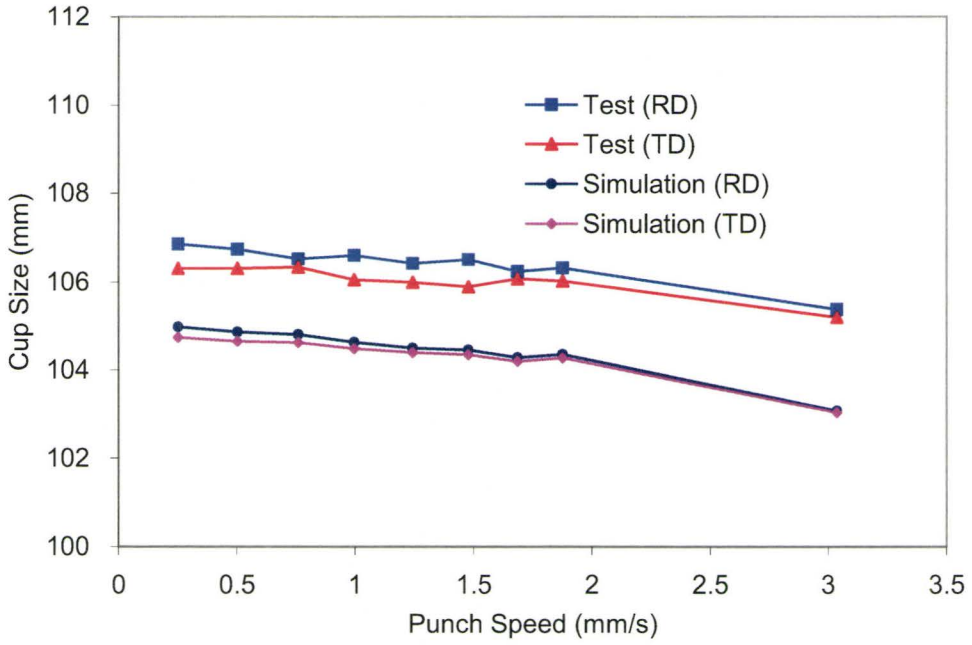

Figure 6.24 Cup size comparison.

Failure Locations

In the first part of the cup drawing experiments, two sheet samples were drawn until the material failed, such that the maximum punch displacement before material failure could be found. Figure 6.25 shows the failed samples, where the rolling direction of the sheets was marked on the sheets by the black arrows. It shows that both sheets failed in the rolling direction. This can be attributed to the material anisotropy of the sheets, but the strong frictional anisotropy of mill-finished aluminum sheets could be a source of this phenomenon.

To compare with these test results, the simulation for test Case 1 were performed with larger punch displacement (21 mm). Figures 6.26 and 6.27 show the von Mises

stress and plastic strain distributions of the deformed sheet, where the highly stress/strain concentrated area is the possible failure region. The comparison shows that the current simulation with the new friction model accurately predicted the location and direction of the failure region. The material anisotropy was not considered in the current simulation. This implies that the frictional anisotropy could be the source of the directional material failure.

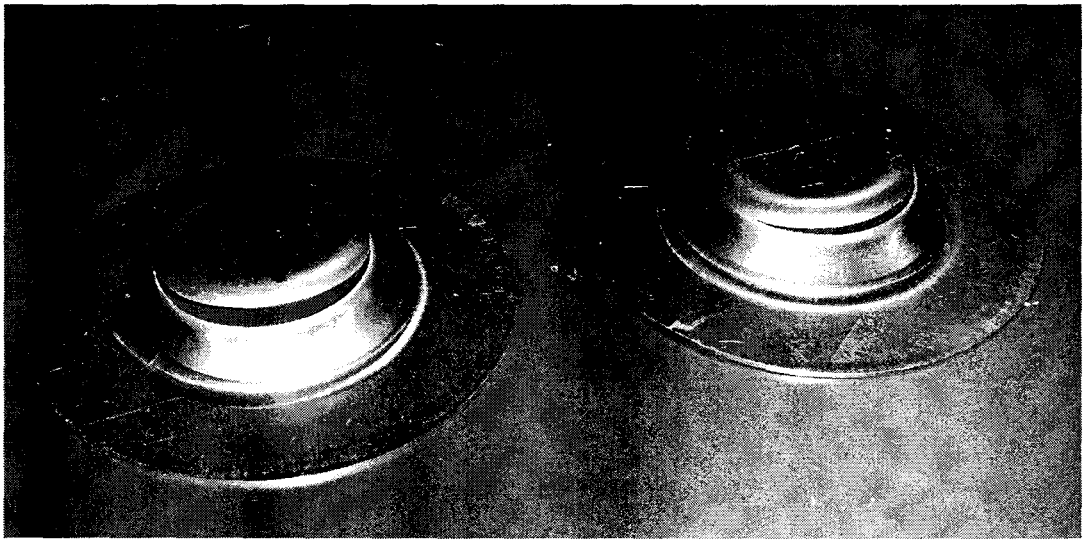

Figure 6.25 Failed samples (RD of the sheets marked by arrow).

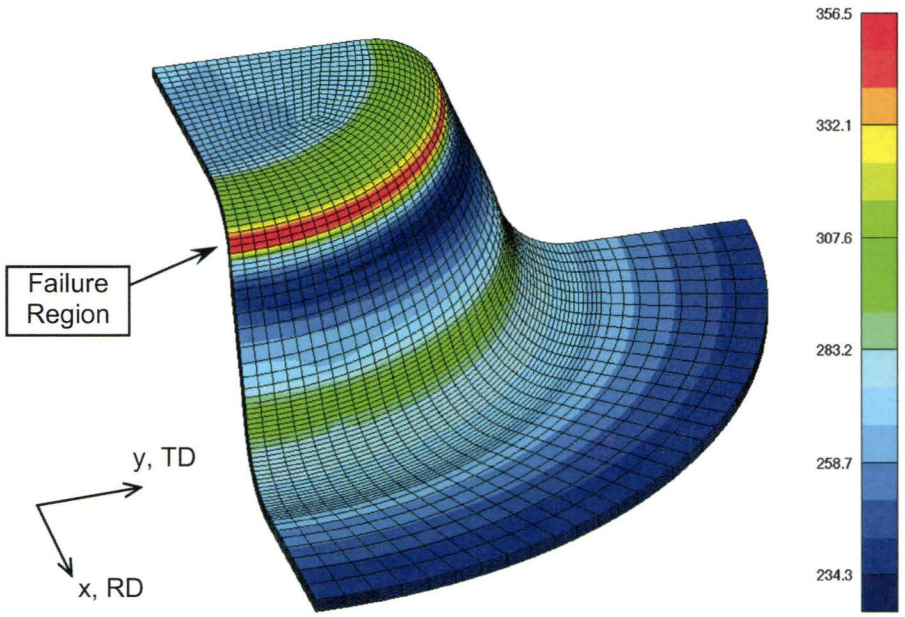

Figure 6.26 vonMises stress (MPa) distribution of the sheet for case 1 with larger punch displacement (21 mm).

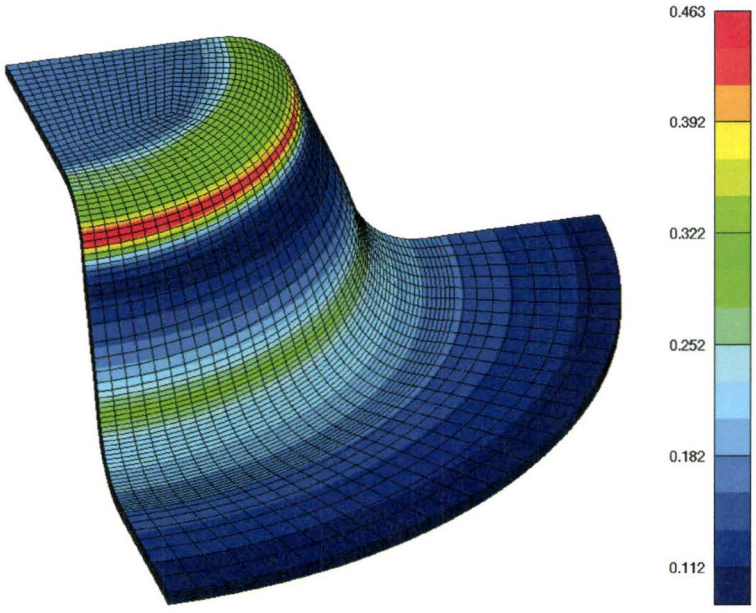

Figure 6.27 Plastic strain (natural strain) distribution of the sheet for case 1 with larger punch displacement (21 mm).

CHAPTER 7

CONCLUSIONS AND RECOMMENDATIONS

7.1. Conclusions

7.1.1. Analysis Method of Draw-Bend Friction Test

On the aspect of the research aimed at getting the most information out of draw-bend friction tests, the following conclusions have been realized.

- The contact pressure distribution in draw-bend test is not uniform with less contact angle than geometric wrap angle. The non-uniformity becomes more severe with decreasing pin diameter.

- The conventional analysis method for draw-bend friction test has shortcomings in addressing pressure dependent friction. The conventional method is valid only for measuring an average friction coefficient over the pressure range that exists in the specific draw-bend system.

- A new method to determine a friction coefficient as pressure dependent polynomial function has been developed. In the new method the pressure non-

uniformity, which persists in draw-bend friction tests, is exploited to measure the pressure dependency of friction coefficient.

7.1.2. Friction Measurements and Modeling for MF Aluminum Sheets

The new pressure dependent method had been applied to the friction measurement and modeling of aluminum sheets and the following have been achieved.

- By applying the new method to friction measurements on MF aluminum sheets, friction coefficients in RD and TD of the sheets were obtained as functions of contact pressure and sliding speed.

- The obtained model was effectively implemented into a finite element code using interpolation functions at minimal computational cost (3.8% increase of computation time for the block sliding simulation in chapter 6). Friction anisotropy was considered in the implementation using stick/slip criterion expressed as an ellipse.

- The developed friction model was validated by circular cup drawing experiments and simulations. The comparisons showed good agreements in the aspects of punch force, cup size and failure location.

7.2. Recommendations and Future Works

7.2.1. Analysis Method of Draw-Bend Friction Test

In the new analysis method, the friction coefficient was obtained as a function of pressure, velocity and sliding direction, assuming that frictional effects from other local conditions such as sliding distance and plastic strain are minor. The extension of the method to consider those local conditions in the analysis is required.

7.2.2. Friction Measurements and Modeling for MF Aluminum Sheets

More investigations on the following items listed below are recommended for future works.

- In the application of the new method to friction measurement on MF aluminum sheets, only two different diameter pins (12.7 mm and 25.4 mm) were used resulting in the friction coefficient as linear functions of pressure. Friction tests with larger number of pins are required to estimate the friction coefficients in more general forms.

- In the current test geometry, the sliding distances were different among pins as illustrated in Figure 7.1. It is recommended to performing draw-bend tests at

the condition of the same sliding distance by applying a different wrap angle for each pin diameter. The comparison with the results from current test geometry will evaluate the effect of sliding distance on friction, since sliding distance may affect how consistent lubrication conditions remain during the tests.

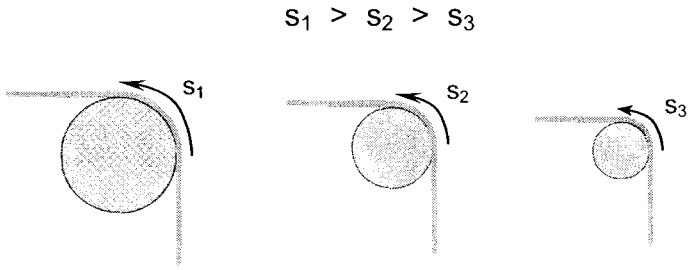

Figure 7.1 Difference in sliding distances among pins involved in the analysis.

- In the circular cup drawing experiments for model validation, cups could be drawn to maximum ~17 mm depth before the material failure, which is quite small compared to the diameter of sheet samples (111 mm). This was due to a relatively large difference between punch (48 mm) and upper die (57.8 mm) diameters. Cup drawing experiments with a larger punch size are recommended for the future work, so that the friction model can be validated for the full range of cup drawing process.

- For anisotropic friction model, the stick/slip criteria represented as an ellipse in this work is an assumption that needs further investigation. For the purpose, more draw-bend friction tests are necessary for the other textural directions of the sheets to more comprehensively verify the suitability of the ellipse model.

REFERENCES

ABAQUS 6.5 (2005) Theory Manuals, Hibbitt, Karlsson & Sorensen, Inc., RI, USA

Alinger, M.J., Sriram, S. and Matlock, D.K. (1999), "An Investigation of Strain Evolution in the Bending-Under-Tension Friction Test", Proceedings of the TMS, PA, pp. 129-140

Belytschko, T., Liu, W.K. and Moran, B. (2000), "Nonliear Finite Elements for Continua and Structures", John Wiley & Sons, New York

Bowden, F.P. and Tabor, D. (1971), "The Friction and Lubrication of Solids", Oxford, Clarendon Press

Buczkowski, R. and Kleiber, M. (1997), "Elasto-Plastic Interface Model for 3D-Frictional Orthotropic Contact Problems", Interanational Journal for Numerical Methods in Engineering, vol. 40, pp. 599-619

Chvedov, D., Jones, R. and Rosenfeld, A. (2003), "Effect of Lubricant Quantity and Surface Topography on the Frictional Behaviour of Can Body Stock", Tribology Transactions, vol. 46, pp. 339-347

Coubrough, G.J., Alinger, M.J. and Van Tyne, C.J. (2002), "Angle of Contact between Sheet and Die during Stretch-Bend Deformation as Determined on the Bending-Under-Tension Friction Test System", Journal of Materials Processing Technology, 130-131, pp. 69-75,

Deng, Z. and Lovell, M.R. (2000), "Effects of Lubrication and Die Radius on the Friction Behavior of Pb-coated Sheet Steels", Wear, vol. 244, pp. 41-45

Dowson, D. (1998), "History of Tribology", 2nd ed., Professional Engineering Publishing, London and Bury St Edmunds, UK

Emmens, W.C. (1988), "The Influence of Surface Roughness on Friction", the 15th Biennial Congress of the IDDRG, Dearborn, USA, pp. 63-70

Fox, R.T., Maniatty, A.M. and Lee, D. (1989), "Determination of Friction Coefficient for Sheet Materials under Stretch-Forming Conditions", Metall. Trans. A, Vol.2, pp. 2179-2182

Fratini, L., Casto, S.Lo and Valvo, E.Lo (2006), "A Technical Note on an Experimental Device to Measure Friction Coefficient in Sheet Metal Forming", Journal of Material Processing Technology, vol. 172, pp. 16-21

Ghosh, A.K. (1977), "A Method for Determining the Coefficient of Friction in Punch Stretching of Sheet Metals", International Journal of Mechanical Science", vol. 19, pp. 457-470

Han, S.S. (1997), "The Influence of Tool Geometry on Friction Behavior in Sheet Metal Forming," Journal of Materials Processing Technology 63, 129-133

Hanaki, K. and Kato, K. (1984), "Pressure Peak in Bending and Unbending Process", Advanced Technology of Plasticity 1, pp 581-586

Hjiaj, M., Feng, Z.-Q., de Saxcé, G. and Mróz, Z. (2004), "On the Modelling of Complex Anisotropic Frictional Contact Laws", International Journal of Engineering Science, vol. 42, pp. 1013-1034

Hsu, T-C. and Liu, C-C. (1998), "Internal Variables Effects in Punch Friction Characterization", Transactions of the ASME, vol. 120, pp. 510-516

Jones, R.E. and Papadopoulos, P. (2006), "Simulating Anisotropic Frictional Response using Smoothly Interpolated Traction Fields", Computer Methods in Applied Mechanics and Engineering", vol. 195, pp. 588-613

Kenny, L.D., Pelow, C. and Nolan, P. (2000), "Measurement of the Coefficient of Friction of Automotive Sheet", Materials Review, Alcan International

Keum, Y.T., Wagoner, R.H. and Lee, J.K. (2004), "Friction Model for FEM Simulation of Sheet Metal Forming Operations," NUMIFORM'04, Columbus, Ohio, USA

Kim, Y.S., Jain, M.K. and Metzger , D.R. (2004), "A Finite Element Study of Capstan Friction Test", Materials Processing and Design: Modeling, Simulation and Applications, NUMIFORM 2004, pp. 2264-2269

Kotchman, D.P., Kim, I., Sa, C.-Y. and Lee, D. (1992), "Determination of Frictional Behavior in Sheet Metals Using Orthogonal Arrays," Journal of Materials Engineering and Performance 1, 555-564

Kwon, Y.W. and Bang, H.C. (2000), "The Finite Element Method Using MATLAB", CRC Press LLC, 2nd Ed.

Lee, B.H., Keum, Y.T. and Wagoner, R.H. (2002), "Modeling of the Friction Caused by Lubrication and Surface Roughness in Sheet Metal Forming", Journal of Materials Processing Technology, vol. 130-131, pp. 60-63

Mamalis, A.G., Manolakos, D.E. and Baldoukas, A.K. (1997), "Simulation of Sheet Metal Forming Using Explicit Finite-Element Techniques: Effect of Material and Forming Characteristics Part 1. Deep-Drawing of Cylindrical Cups", Journal of Materials Processing Technology, vol. 72, pp. 48-60

Matuszak, A. (2000), "Determination of the Frictional Properties of Coated Steel Sheets", Journal of Materials Processing Technology", vol. 106, pp. 107-111

Murtha, S.J., Story, J.M., Jarvis, G.W. and Zonker, H.R. (1995), "Anisotropy Effects in the Forming of Aluminum Sheet", Alcoa

Nakamachi, E. and Huo, T. (1996), "Dynamic-Explicit Elastic Plastic Finite-Element **Simu**lation of Hemispherical Punch-Drawing of Sheet Metal", vol. 13, pp. 327-338

Orowan, E. (1941), "The Calculation of Roll Pressures in Hot and Cold Flat Rolling", **Proc**. I. Mech. E., Vol. 150, pp. 140

Patula, E.J. (1979), "The Tension-Roller-Leveling Process: Elongation and Power Loss, **Journal** of Engineering for Industry, vol. 101, pp. 269-277

Reid, J.V. (2005), "The Twist Compression Test for Evaluating Lubricant/Material **Combinations**", Tribology and Lubrication Technology, Vol. 61, pp. 50-52

Roizard, X., Raharijaona, F., Von Stebut, J. and Belliard, P. (1999), "Influence of Sliding Direction and Sliding Speed on the Micro-Hydrodynamic Lubrication Component of Aluminum Mill-Finished Sheets", Tribology International, vol. 32, pp. 739-747

Saha, P.K. and Wilson, R.D. (1993), "Friction in Forming Electro-galvanized Steel Sheet **with** Tool Steel and Carbide Coated Tools," in Symposium on Contact Problems and Surface Interactions in Manufacturing and Tribological Systems ASME, 209-218

Saha, P.K. and Wilson, R.D. (1994), "Factors Affecting the Accuracy and Control of the **Sheet** Metal Forming Simulator", Transactions of NAMRI/SME, pp. 47-53

Saha, P.K., Wilson, R.D. and Timsit, R.S. (1996), "Influence of Surface Topography on **the** Frictional Characteristics of 3104 Aluminum Alloy Sheet", Wear, vol. 197, pp. 123-129

Sauvé, R.G. (1999), "H3DMAP Version 6 - A General Three-Dimensional Finite **Element** Computer Code for Linear and Nonlinear Analysis of Structures" Ontario Power **Technologies** Report No. A-NSG-96-120, Rev. 1

Sauvé, R.G. and Metzger, D.R. (1995), "Advances in Dynamic Relaxation Techniques for Nonlinear Finite Element Analysis", Journal of Pressure Vessel Technology-Transactions of the ASME, vol. 117, pp. 170-176

Sauvé, R.G., Morandin, G. and Khajehpour, S. (2002), "Contact Simulation in Finite Deformation – Algorithm and Modelling Issues", Computational Mechanics: Developments and Applications, ASME PVP vol. 441, pp. 3-14

Schey, J.A. and Nautiya, P.C. (1991), "Effects of Surface Roughness on Friction and Metal Transfer in Lubricated Sliding of Aluminum Alloys against Steel Surfaces", Wear, Vol. 146, pp. 37-51

Schipper, D.J. (1988), "Transitions in the Lubrication of Concentrated Contacts", Ph.D. Thesis, University of Twente, Enschede, the Netherlands

Shi, Y. and Metzger, D.R. (2001), "A New Penalty Stiffness Treatment for Master-Slave Contact Surfaces", Emerging Technologies: Advanced Topics in Computational Mechanics and Risk Assessment, ASME PVP vol. 417, pp. 43-49

Sniekers, R.J.J.M. (1996), "Friction in Deep Drawing", PhD Thesis, Eindhoven University of Technology, The Netherlands

Swift, H.W. (1948), "Plastic Bending Under Tension", Engineering, Vol. 3, pp. 333-359

Ter Haar, R.T. (1996), "Friction in Sheet Metal Forming, the Influence of Local Contact Conditions and Deformation", Ph.D. Thesis, University of Twente, Enschede, the Netherlands

Vallance, D.W. and Matlock, D.K. (1992), "Application of the Bending-Under-Tension Friction Test to Coated Sheet Steels", Journal of Materials Engineering and Performance, Vol. 1(5), pp. 685-694

Vermeulen, M., Hoebeke, H. and Antonissen, J. (2001), "Mixed Lubricated Plastic Contact Phenomena in EBT Textured Steel Sheet", Proceedings of the 9th International Conference on Sheet Metal, Leuven, Belgium, pp. 415-424

Wagoner, R.H. and Chenot, J.-L. (1996), "Fundamentals of Metal Forming", John Wiley & Sons, pp. 313-338

Wang, J.F., Wagoner, R.H., Matlock, D.K. and Barlat, F (2005), "International Journal of Solids and Structures", vol. 42, pp. 1287-1307

Westeneng, A. (2001), "Modelling of Contact and Friction in Deep Drawing Processes", Ph.D. Thesis, University of Twente, Enschede, the Netherlands

Wihlborg, A. and Crafoord, R. (2001), "Steel Sheet Surface Topography and its Influence on Friction in a Bending under Tension Friction Test", International Journal of Machine Tools & Manufacture, vol. 41, pp. 1953-1959

Wiklund, D., Wihlborg, A. and Rosén, B.-G. (2004), "Evaluation of Surface Topography Parameters for Friction Prediction in Stamping", Wear, vol. 257, pp. 1296-1300

Wilson, W.R.D., Malkani, H.G. and Saha, P.K. (1991), "Boundary Friction Measurements Using a New Sheet Metal Forming Simulator", Transactions of NAMRI/SME , pp. 37-54

Zhang, H.W., He, S.Y. and Wriggers, P. (2004), "A New Algorithm for Numerical Solution of 3D Elastoplastic Contact Problems with Orthotropic Friction Law", Computational Mechanics, vol. 34, pp. 1-14

Zheng, R. and Overby, D. (1988), "Strip Friction Experimental Study on Galvanized Steel Sheet," in Proceedings of the 15th Biennial Congress on Controlling Sheet Metal Forming Processes ASM, 85-90

Zhou, D. and Wagoner, R.H. (1995), "Development and Application of Sheet-Forming Simulation", Journal of Materials Processing Technology, vol. 50, pp. 1-16

APPENDIX A

DESIGN DRAWINGS FOR NEWLY MADE PIN UNITS

A.1. 42 mm Fixed Pin Unit – Pin

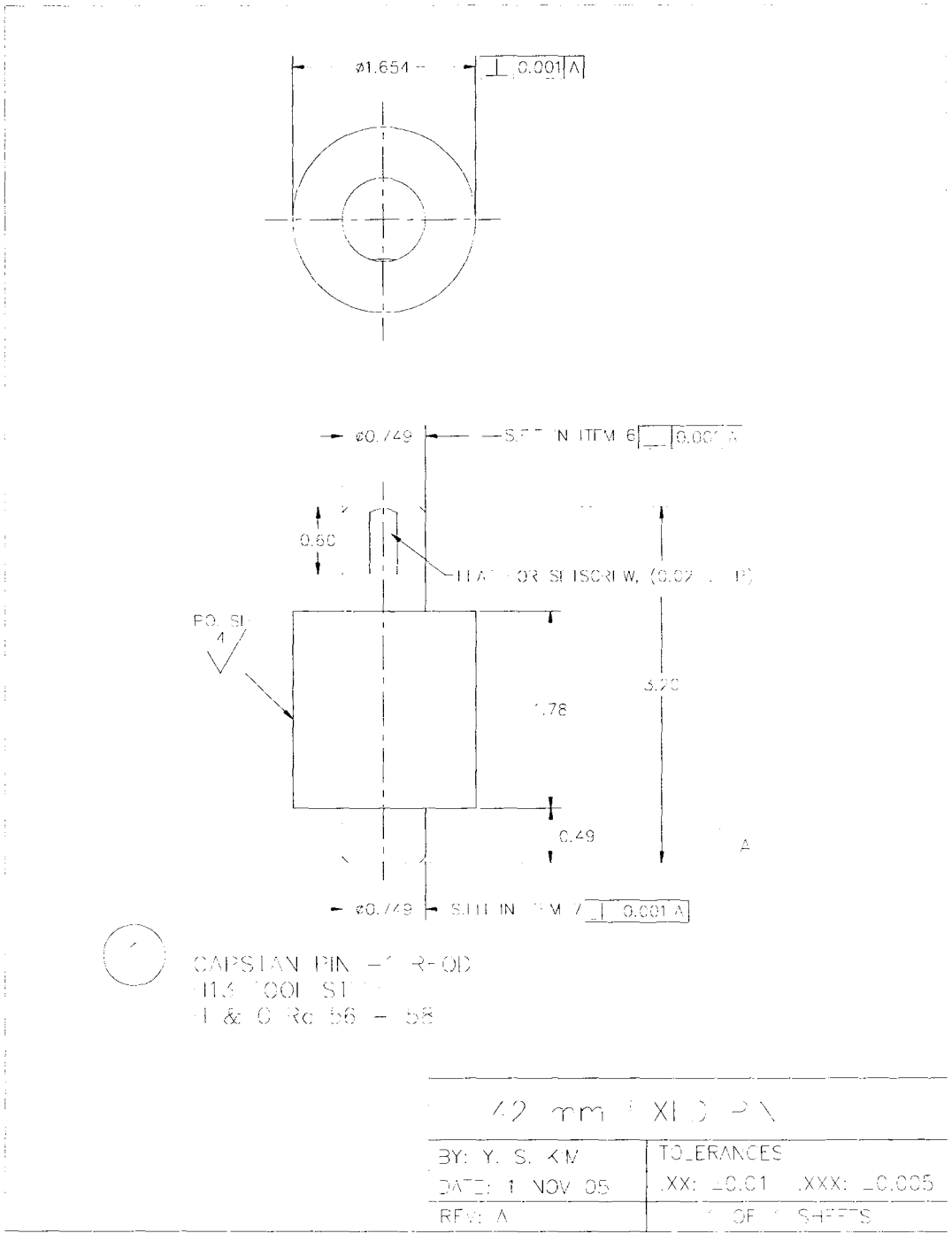

A.2. 42 mm Fixed Pin Unit – Pin Holder (Top)

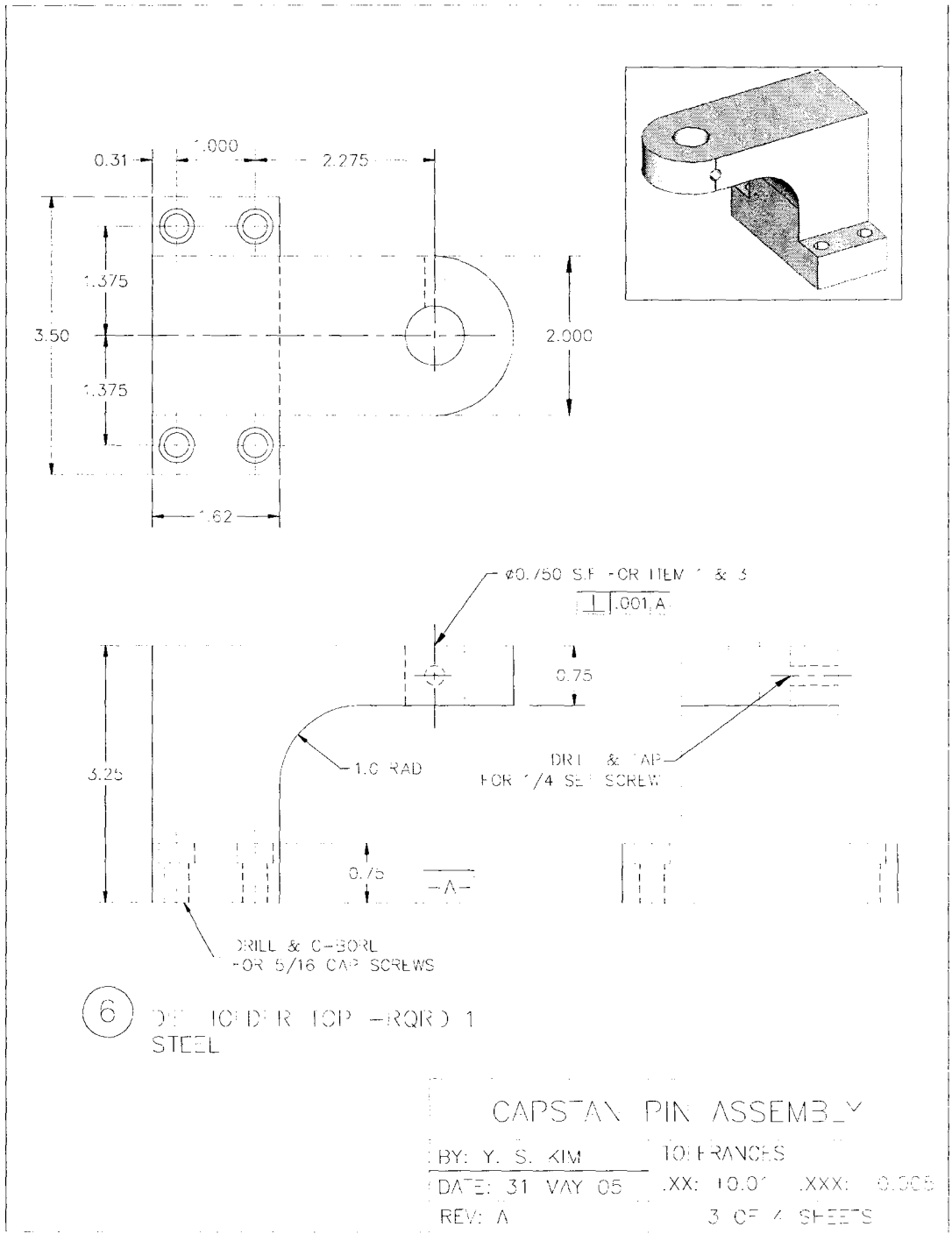

A.3. 42 mm Fixed Pin Unit – Pin Holder (Bottom)

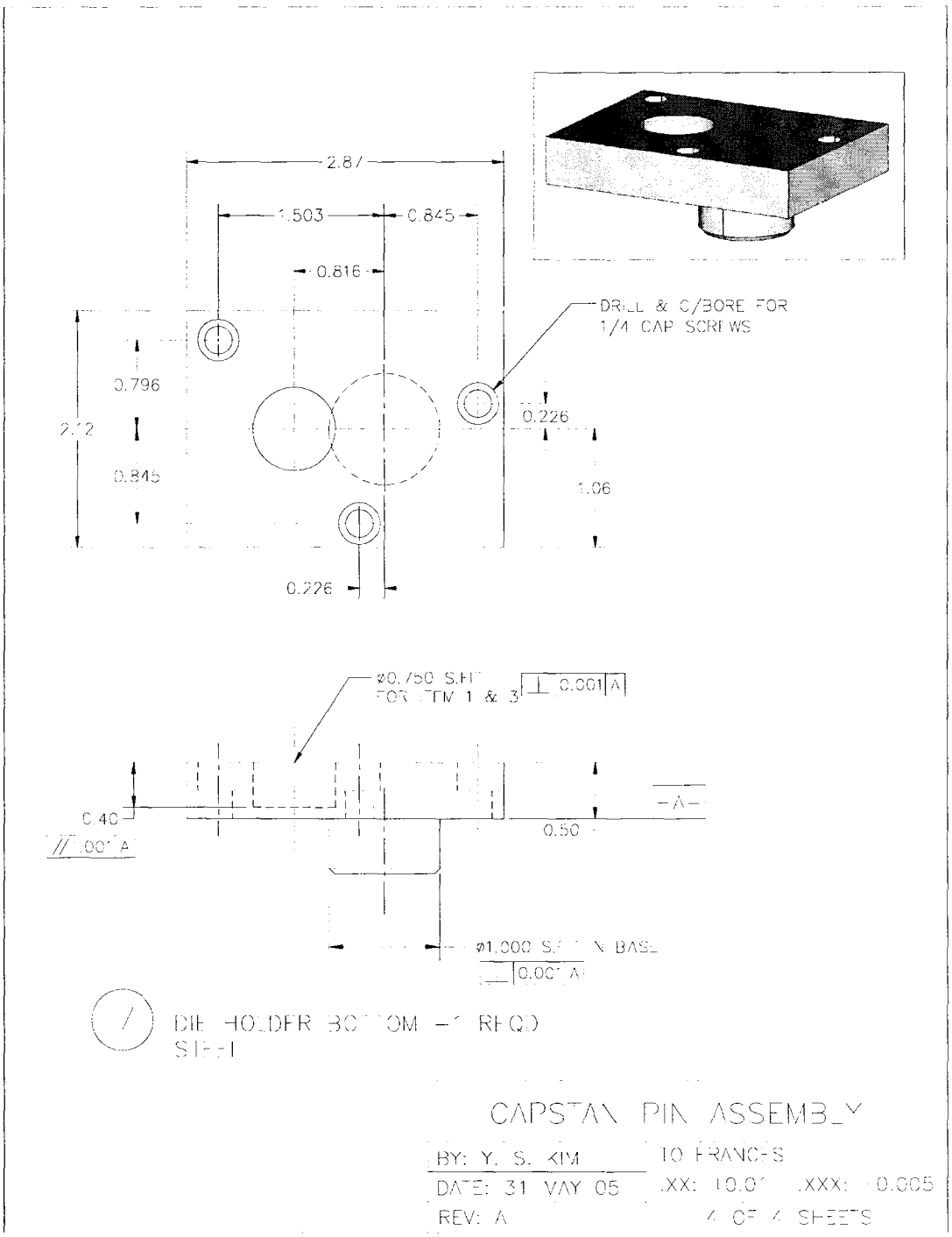

A.4. 12.7 mm Rotating Pin Unit – Pin and Pin Holder (Top)

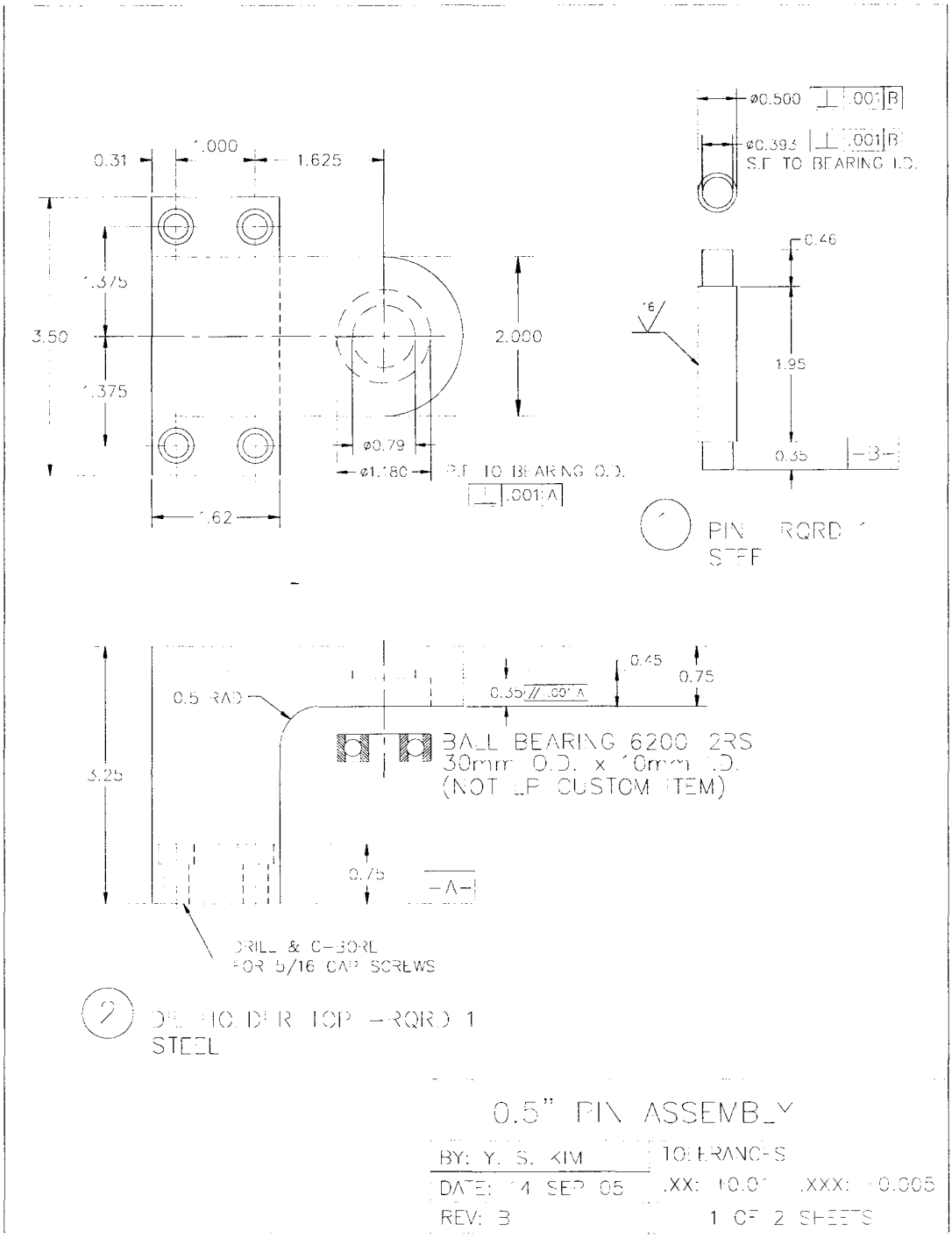

A.5. 12.7 mm Rotating Pin Unit – Pin Holder (Bottom)

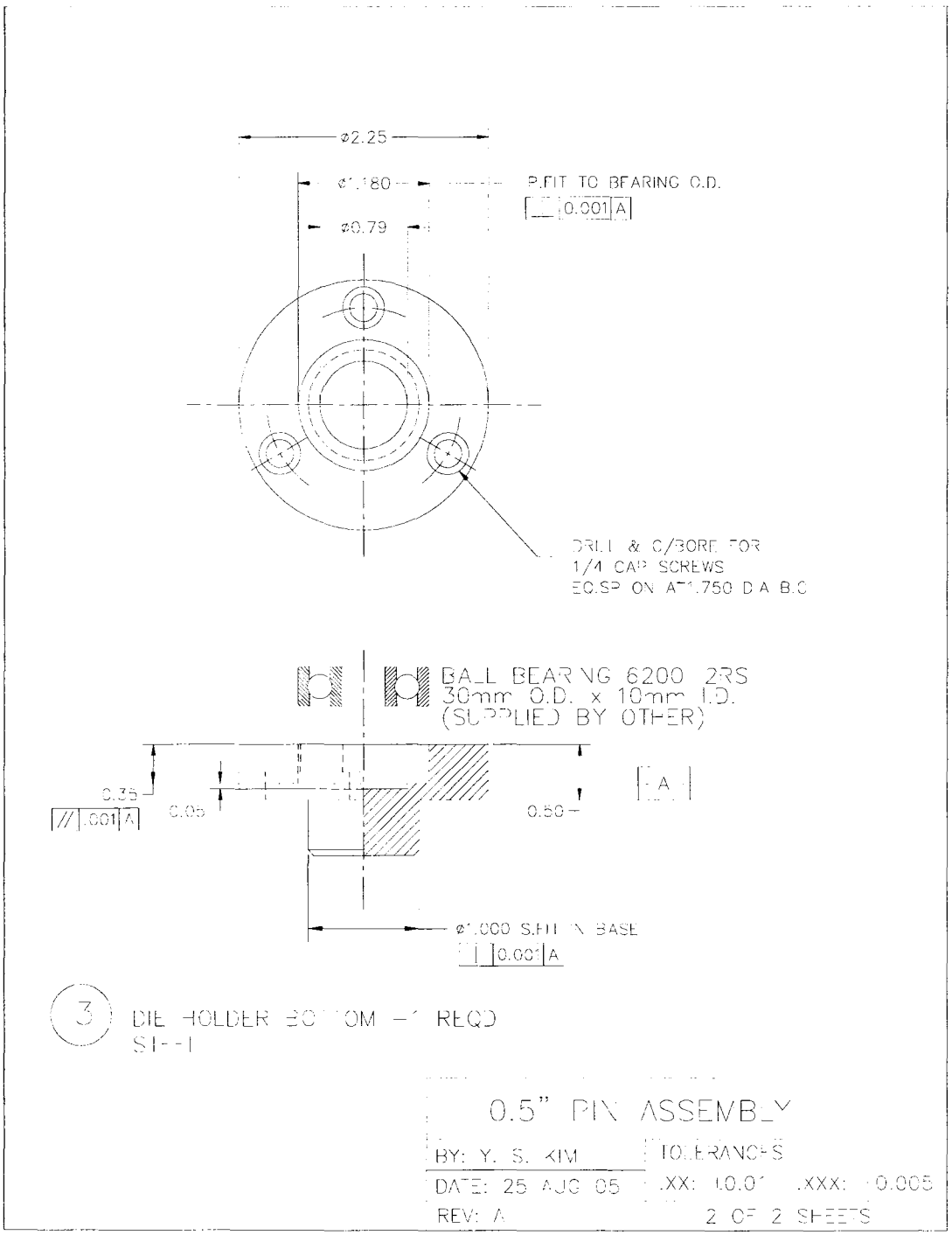

A.6. 25.4 mm Rotating Pin Unit – Pin and Pin Holder (Top)

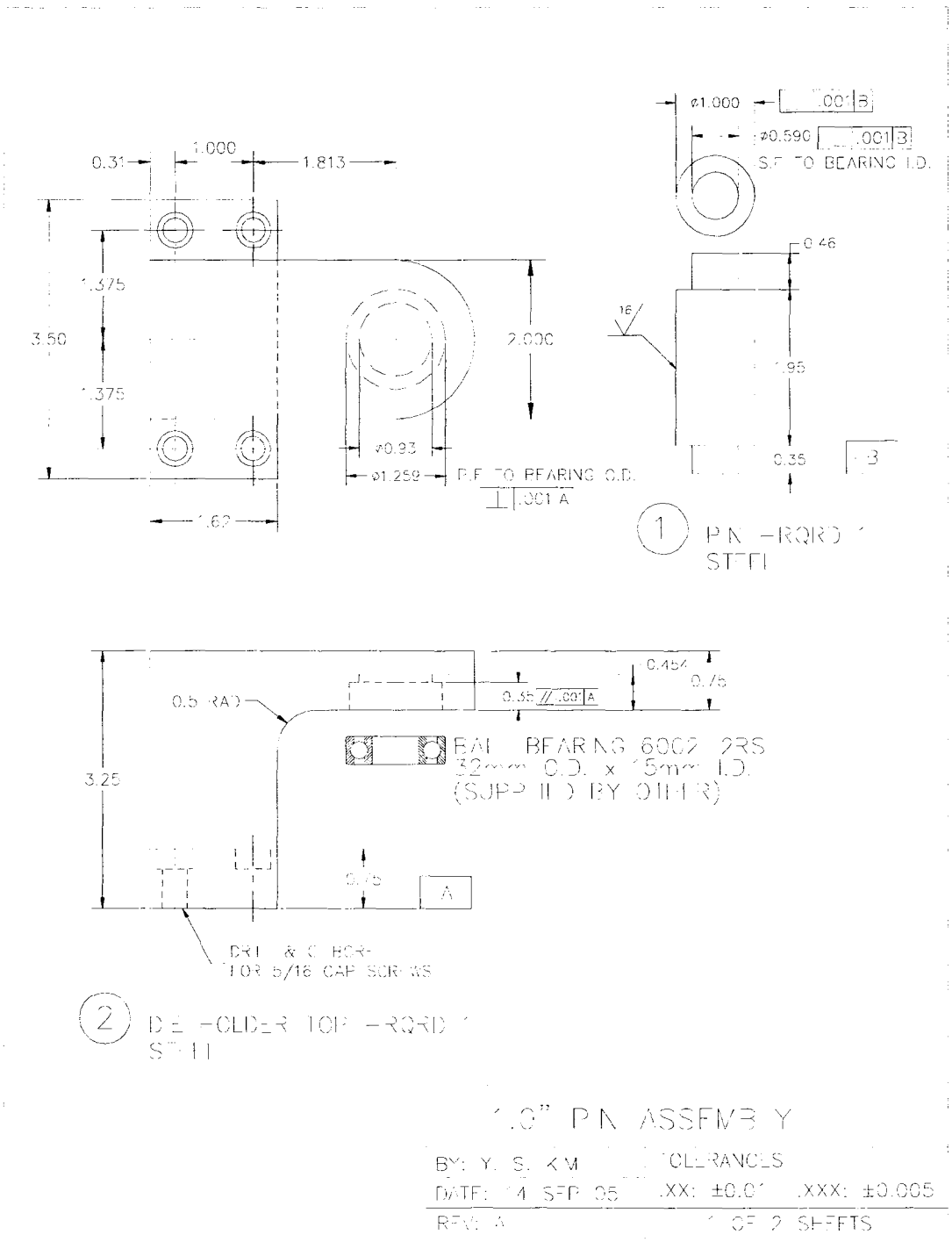

A.7. 25.4 mm Rotating Pin Unit – Pin Holder (Bottom)

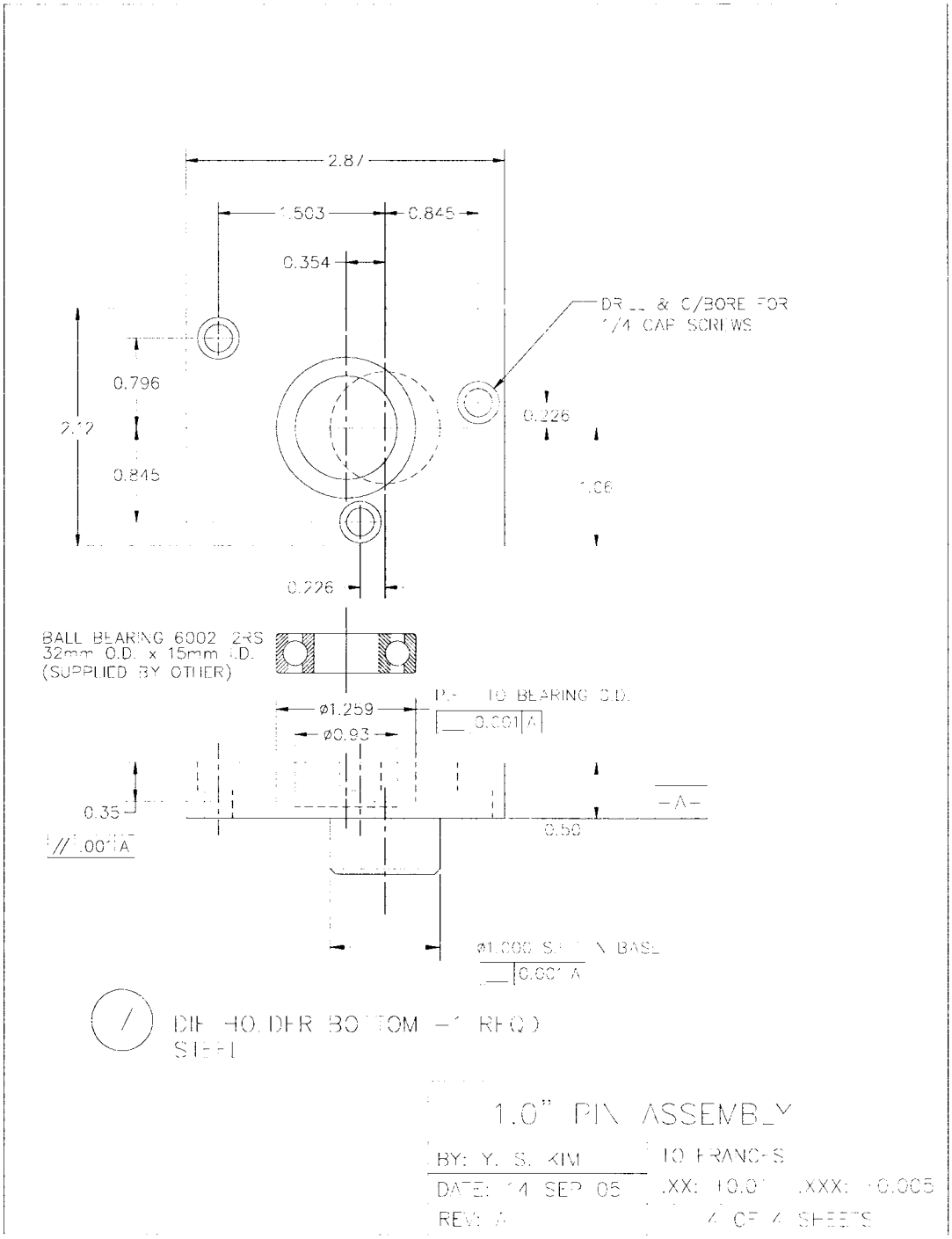

A.8. 42 mm Rotating Pin Unit – Pin